Measurement and Control of Occupational Exposure to Engineered Nanoparticles

A Dissertation
SUBMITTED TO THE FACULTY OF
UNIVERSITY OF MINNESOTA
BY

Drew Jorgen Thompson

IN PARTIAL FULFILLMENT OF THE REQUIREMENTS
FOR THE DEGREE OF
DOCTOR OF PHILOSOPHY

David Y.H. Pui

December 2017

Acknowledgements

I would like to thank my advisor, Dr. David Y.H. Pui, for his guidance, support, and patience. The positive attitude he fosters in the Particle Technology Laboratory has made my years spent here an enjoyable and enriching experience. I would also like to thank former and current PTL colleagues for all the assistance and camaraderie they offered during my time as a student. Finally, I would like to thank my family for their unconditional support.

Chapter 2:

I would like to thank my collaborators at Empa for their contributions and their hospitality during my stay.

This work was supported by the National Institute of Environmental Health Sciences grant # 1RC2ES018741-01 (sub-grant 100029-D) on "Hazard Assessment and Risk Estimation of Inhaled Nanomaterials Exposure" and the National Science Foundation grant (Award ID: 1056479) on "Real Time Measurement of Agglomerated or Aggregated Airborne Nanoparticles Released from a Manufacturing Process and Their Transport Characteristics."

Chapter 3:

Thanks to Prof. Jing Wang and Dr. Lin Li for their assistance in the exposure assessment, Prof. Shawn Chen for his assistance and contribution of the use of the PENS, and Prof. Jacob Swanson for the idea of using a catalytic stripper and allowing me to

borrow one. I would also like to thank the company and employees who participated in the study.

This work was supported by the National Institute of Environmental Health Sciences grant # 1RC2ES018741-01 (sub-grant 100029-D) on "Hazard Assessment and Risk Estimation of Inhaled Nanomaterials Exposure" and the National Science Foundation grant (Award ID: 1056479) on "Real Time Measurement of Agglomerated or Aggregated Airborne Nanoparticles Released from a Manufacturing Process and Their Transport Characteristics." Parts of this work were carried out in the Characterization Facility, University of Minnesota, which receives partial support from NSF through the MRSEC program.

Chapter 4:

Thank you to Dr. Min Tang for obtaining the experimental data used for the verification of the surrogate models and for discharging electret filter media for examination by SEM. Thanks to Mr. Seungkoo Kang for examining the filter media by SEM.

I would like to acknowledge the support of members of the Center for Filtration Research: 3M Co., A.O. Smith, Applied Materials, BASF Corp., Boeing Commercial Airplanes, Cummins Filtration, Donaldson Co., Inc., Entegris Inc., Ford Motor Co., Gore, MSP Corp., Samsung Electronics Co., Ltd., Shengda Filtration Technology Co., Ltd., Shigematsu Works Co., Ltd., TSI Inc., WatYuan Filtration System Co., Ltd., Yancheng Environmental Protection Science and Technology City and affiliate member National Institute for Occupational Safety and Health.

I also acknowledge the Minnesota Supercomputing Institute (MSI) at the University of Minnesota for providing resources that contributed to the research results reported within this chapter. Parts of this work were carried out in the Characterization Facility, University of Minnesota, which receives partial support from NSF through the MRSEC program.

Abstract

This dissertation consists of three studies concerning the measurement and control of inhalation exposure to engineered nanoparticles in the workplace. A key component in evaluating the potential health risks posed by nanomaterials is understanding how a worker may be exposed to airborne engineered nanoparticles. This information is not only needed for establishing safer nanomaterial work practices, toxicology studies also require doses which are relevant to actual workplace exposure. Emission monitoring and exposure assessments were conducted in nanotechnology workplaces in an effort to answer these questions.

In Chapter 2, the synthesis of silicon carbide (SiC) nanoparticles in a prototype inductively coupled thermal plasma reactor and other supporting processes, such as the handling of precursor material, the collection of nanoparticles, and the cleaning of equipment, were monitored for particle emissions and potential worker exposure. The purpose of this study was to evaluate the effectiveness of engineering controls and best practice guidelines developed for the production and handling of nanoparticles, identify processes which result in a nanoparticle release, characterize these releases, and suggest possible administrative or engineering controls which may eliminate or control the exposure source. No particle release was detected during the synthesis and collection of SiC nanoparticles and the cleaning of the reactor. This was attributed to most of these processes occurring in closed systems operated at slight negative pressure. Other tasks occurring in more open spaces, such as the disconnection of a filter assembly from the

reactor system and the use of compressed air for the cleaning of filters which collected synthesized SiC nanoparticles, resulted in releases of submicrometer particles with a mode size of ~ 170 – 180 nm. Observation of filter samples under scanning electron microscope confirmed that the particles were agglomerates of SiC nanoparticles.

In Chapter 3, results are presented from an assessment of potential exposure to multi-walled carbon nanotubes (MWCNTs) conducted at an industrial facility where polymer nanocomposites were manufactured by an extrusion process. Recent animal studies have shown that carbon nanotubes (CNTs) may pose a significant health risk to those exposed in the workplace. To further understand this potential risk, effort must be taken to measure the occupational exposure to CNTs. Exposure to MWCNTs was quantified by the thermal-optical analysis for elemental carbon (EC) of respirable dust collected by personal sampling. All personal respirable samples collected (n = 8) had estimated 8-hour time weighted average (TWA) EC concentrations below the limit of detection for the analysis, and about one half the recommended exposure limit for CNTs of 1 μg EC/m^3 as an 8-hour TWA respirable mass concentration. Potential exposure sources were identified and characterized by direct-reading instruments and area sampling. Area samples analyzed for EC yielded quantifiable mass concentrations inside an enclosure where unbound MWCNTs were handled and near a pelletizer where nanocomposite was cut, while those analyzed by electron microscopy detected the presence of MWCNTs at six locations throughout the facility. Through size selective area sampling, it was found that the airborne MWCNTs present in the workplace were in the form of large agglomerates. This was confirmed by electron microscopy, where most of the MWCNT structures

observed were in the form of micrometer-sized, ropey agglomerates. However, a small fraction of single, free MWCNTs was also observed. It was found that the high number concentrations of nanoparticles, approximately 200,000 particles/cm^3, present in the manufacturing facility were likely attributable to polymer fumes produced in the extrusion process.

Chapter 4 details the development of a theoretical model to predict the filtration efficiency of electret filter media. Electret filters are filters whose fibers are semi-permanently charged. This charge results in electrostatic interactions between particles and fibers which can increase filtration efficiency without increasing the pressure drop across the filter, thus making electret media well-suited for use in local exhaust ventilation and respiratory protection. The numerical results were used to develop surrogate models which considered a random fiber orientation, filter solidity, particle interception, and dielectrophoretic, image, and Coulomb forces. The mean error of predicted single fiber efficiencies for the surrogate models of charged and uncharged particles were 6% and 0.8%, respectively. Aerosol penetration estimated by the surrogate models for a best fit effective surface charge density were compared to experimentally evaluated electret filters. Coefficients of determination for the fitted effective surface charge densities ranged from 0.82 to 0.98 and the effective surface charge densities were comparable to values reported in the literature.

Table of Contents

List of Tables

List of Figures

1 Introduction

Engineered nanoparticles are man-made particles designed to have at least one dimension in the approximate size range of 1 to 100 nm. They are separate from incidental nanoparticle which can be created by both unintentional sources, such as combustion or welding, and natural sources, such as volcanic eruptions (Methner et al., 2010). Engineered nanoparticles are created top-down by destruction of a bulk material or bottom-up starting at nucleation with subsequent growth by condensation and/or coagulation, with bottom-up being the most common route in industrial engineered nanoparticle production (Kuhlbusch et al., 2011). Engineered nanoparticle-enabled nanotechnology is experiencing tremendous growth. According to Lux Research, nanotechnology will be incorporated into $3 trillion worth of products globally by 2020 (Lux Research, 2016). By 2020 an estimated 6 million workers will be employed in the nanotechnology sector (Roco, 2017). Nanotechnology labor and markets are estimated to continue to double every 3 years (Roco, 2017).

While particles in the nanometer size range have been seen to be desirable for the development of new technologies, it has been demonstrated that nanoparticles may pose a significant health risk. Particles smaller than 100 nm are deposited deep into the alveoli of the lung (ICRP, 1994). Once deposited, the larger specific surface areas of nanoparticles can induce greater pulmonary effects than larger submicrometer particles (Oberdörster et al., 1994). Nanoparticles have also been found to translocate from nasal airways to the brain (Oberdorster et al., 2004).

With increased production of nanotechnology enabled products, the potential for worker exposure to nanoparticles will also increase. For controlling exposure to occupational hazards, the traditional hierarchy of controls, listed in order from most to least

effective, is as follows (National Institute for Occupational Safety and Health Division of Applied Research and Technology (DART) 2016): 1) Elimination: physically remove the hazard, 2) Substitution; replace the hazard, 3) Engineering controls: Isolate people from the hazard, 4) Administrative controls: Change the way people work, and 5) Personal Protective Equipment: Protect the worker with Personal Protective Equipment. When working with engineered nanoparticles, elimination and substitution may be difficult because these materials were chosen because of their unique properties (NIOSH, 2013a). This leaves engineering controls, administrative controls, and personal protective equipment as means to protect workers from occupational exposure to engineered nanoparticles.

In Chapters 2 and 3 of this dissertation aerosol emissions and potential worker exposure were monitored at two different nanotechnology workplaces. The objectives of these studies were twofold. First, the physiochemical characterization of airborne engineered nanoparticles may lead to a better understanding of the hazard and the potential means to control the it. Second, the monitoring of emissions and potential exposure can be used to evaluate the effectiveness of the engineering and administrative controls present in the workplace. In the Chapter 2, silicon carbide nanoparticles were produced by inductively coupled plasma synthesis at a research laboratory [published as Thompson D, Leparoux M, Jaeggi C, Buha J, Pui DYH, Wang J. (2013) Aerosol Emission Monitoring in the Production of Silicon Carbide Nanoparticles by Induction Plasma Synthesis. Journal of Nanoparticle Research, 15: 2103]. The study in Chapter 3 was conducted at an industrial facility which manufactured polymer nanocomposites containing multi-walled carbon nanotubes [published as Thompson D, Chen S-C, Wang J, Pui DYH. (2015) Aerosol

Emission Monitoring and Assessment of Potential Exposure to Multi-walled Carbon Nanotubes in the Manufacture of Polymer Nanocomposites. Annals of Occupational Hygiene, 59: 1135-1151].

Chapter 4 concerns the development of a model to predict the submicrometer particle collection efficiency of electret filter media. This type of filter is utilized in engineering controls (the high efficiency particle air (HEPA) filter used in local exhaust ventilation), in administrative controls (in the HEPA-filtered vacuum cleaner recommended for cleaning work areas after each shift), and personal protective equipment (in respiratory protection) (NIOSH, 2013a). The objective of this study was to provide a more accurate prediction of the filtration efficiency of electret filter media which may be used as performance modeling and design tool.

2 Aerosol Emission Monitoring in the Production of Silicon Carbide Nanoparticles by Induction Plasma Synthesis

2.1 Introduction

Engineered nanomaterial-enabled nanotechnology is experiencing unprecedented growth. In 2010, the global consumption of nanomaterials was 1.7 million metric tons and valued at 5.6 billion US$ (Schlag et al., 2011). By 2015 this market is predicted to grow to 7.4 billion US$ (Schlag et al., 2011), with revenues from products incorporating these nanomaterials reaching 2.5 trillion US$ (Hwang and Bradley, 2010) and 2 million workers employed in the nanotechnology sector (Roco, 2011). While flame aerosol processes currently are the most widely used in manufacturing commercial quantities of nanoparticles (Skillas et al., 2011), inductively coupled thermal plasma (ICP) technologies are emerging as a promising alternative.

In an ICP a current is induced in conductive ionized gas. This electrical energy is converted to thermal energy through resistive heating. Temperatures exceeding 10,000 K can be achieved in ICP reactors, allowing for the evaporation of high melting point precursor materials. Nanoparticles are then formed through gas-to-particle conversion. Unlike a flame reactor, oxygen is not required which permits the synthesis of nonoxide materials. The great flexibility offered by ICP allows for the synthesis of a variety of nanoparticles, including metals, oxides, carbides, and nitrides, as well as complex particles, such as core-shell or hollow nanoparticles (Leparoux et al., 2010; Guo et al., 1997).

With the proliferation of nanotechnology has come concern about potential new hazards to human health and the environment (Oberdörster et al., 2005; Maynard and Pui, 2007; Wang et al., 2011). To determine whether nanoparticles and nanomaterials pose a

risk in the workplace the National Institute for Occupational Safety and Health (NIOSH) Nanotechnology Research Center has identified exposure assessments as a critical area of research and communication (NIOSH, 2012). Although industrial ICP systems can produce a wide variety of nanoparticles at scale of gram to kilogram per hour (Vollath, 2008), there have been few studies conducted assessing the potential for nanoparticle exposure during induction plasma synthesis. One such study was completed at an industrial site housing a large-scale pilot ICP reactor where 20 – 30 nm silver nanoparticles were produced at a rate of 5 kg/day (Lee et al., 2011). Even though no additional engineering controls beyond natural ventilation were employed, they were unable detect a nanoparticle release by scanning mobility particle sizer and optical particle sizer (OPS). This was attributed to all production processes being performed under negative pressure. Personal breathing zone (PBZ) and area samples analyzed by ICP optical emission spectrometry contained 0.02 – 1.02 μg Ag/m^3. Silver nanoparticle agglomerates were also found by TEM. A NIOSH field study was also conducted at a research lab where a pilot scale ICP reactor was used to synthesize 50 – 80 nm aluminum nanoparticles at a scale of kilograms per day (Methner et al., 2010). The cleaning and brushing down of a plasma torch, filter chamber, and cyclone in a ventilated walk-in enclosure was monitored. Background subtracted condensation particle counter (CPC) measured concentrations were 7000 – 16,000 particles/cm^3 during cleaning, while OPS measurements exceeded the upper dynamic range of the instrument. Mass concentrations from area and PBZ samples were 40 – 280 μg/m^3 and 160 μg/m^3, respectively. Evidence of aluminum nanoparticles was found on all area and PBZ samples. Clearly more workplace measurements are needed to accurately characterize the risk posed to workers from exposure to engineered nanoparticles during induction plasma synthesis.

In this study aerosol emissions were monitored during the synthesis of nanoparticles by an ICP reactor prototype and associated production tasks. While highly dependent on the material being synthesized, the reactor prototype is typically capable of producing nanoparticles at a rate of hundreds of grams per hour. This reactor has successfully synthesized tungsten carbide, silicon, copper, and titanium carbonitride nanoparticles (Leparoux et al., 2010; Leparoux et al., 2005). In this assessment silicon carbide (SiC) nanoparticles were produced from the in-flight carburization of metallic silicon, where the silicon precursor reacts with the carbon generated from the decomposition of methane in the plasma. While the Occupational Safety and Health Administration (OSHA) regulates SiC under its generic permissible exposure limit (PEL) of 15 mg/m^3 total particulate and 5 mg/m^3 respirable particulate for particulates not otherwise regulated, inductive plasmas are capable of synthesizing materials regulated under more stringent exposure limits, such as silver which has a PEL of 0.01 mg/ m^3 (OSHA, 2013). Thus, even with its high PEL, it is worthwhile to monitor potential nanoparticle emissions during the synthesis of SiC, as the results may be translated to the synthesis of more hazardous materials. The research objectives of this study were to evaluate the effectiveness of engineering controls and best practice guidelines developed for the production of nanoparticles, identify processes which result in particle emission, characterize these emissions, and suggest possible administrative or engineering controls which may eliminate or control the emission source.

2.2 Methods

2.2.1 *Facility and Process Descriptions*

The ICP reactor prototype was housed in an approximately 170 m^2 laboratory building at the Laboratory for Advanced Materials Processing, Empa – Swiss Federal Laboratories for Materials Science and Technology located in Thun, Switzerland. This lab is dedicated solely to the reactor and contains no office space. The building is kept under slight negative pressure. All ventilation exhaust and aspiration lines pass through two air cleaners (EBS P.4.160, LWK Innofil GmbH, Germany) operating in parallel, with each having a filtration surface of 160 m^2 and handling an airflow of 6,000 m^3/h. The makeup air entering the lab is not filtered. The outside ambient temperature and dew point ranged from -2 – 6 °C and -5 – 3 °C, respectively, during the assessment. The temperature and humidity in the laboratory was uncontrolled, with the indoor temperature being ~ 20 – 22 °C during the study. A schematic of the laboratory is given in Fig. 2.1.

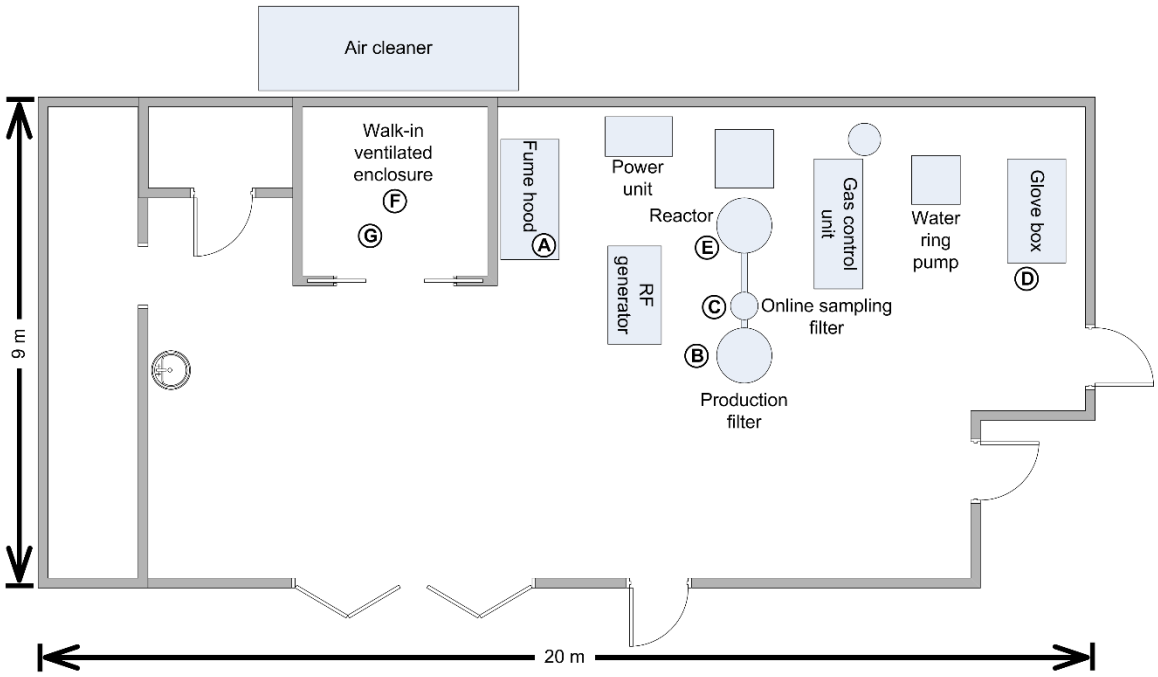

Fig. 2.1 A schematic of the facility housing the ICP reactor prototype where sampling locations corresponding to those listed in Table 2.1 are given by letters

The tasks monitored included the handling of powder precursor, the synthesis of nanoparticles, the disconnection of the sampling filter used to capture these nanoparticles, the collection and packaging of the nanoparticles captured on the filter, and the cleaning of the reactor and filters. The details of these tasks will be presented in the following sections. For safety, all tasks are performed by at least two trained persons. Nanoparticles are passivated for at least 24 hours under static vacuum before any cleaning. After this passivation step, the nanoparticles are normally no longer reactive. If it is known that there is no risk of the nanoparticles reacting with air, as is the case for SiC, alumina or other stable oxides, the cleaning can be done after a few minutes or hours. For all but two tasks, plasma synthesis and cleaning of the production filter, the personal protective equipment (PPE) worn at this facility included a filtering facepiece respirator which provides at least

99% filtration efficiency (FFP3), lab coat, nitrile gloves, and safety glasses. During plasma synthesis, the safety glasses worn were protective against ultraviolet (UV) and infrared (IR) radiation. This was because the plasma was visible through view ports on the reactor, which were also equipped with green UV glass filters. During the cleaning of the production filter the PPE worn included a supplied air, hood type respirator, a Tyvek jumpsuit, nitrile gloves, Tyvek sleeves worn over the seam between jumpsuit and gloves, and shoe covers. A summary of the tasks monitored, the duration and frequency of these tasks, and the engineered controls and PPE employed for each task is given in Table 2.1.

Table 2.1 Summary of tasks monitored in the production SiC nanoparticle by ICP synthesis

Task	Sampling location (Fig. 2.1)	Duration / frequency	Engineering controls	Personal protective equipment	Observations
Handling of powder precursor	A	1 min / daily	Enclosing hood	FFP3, lab coat, nitrile gloves, safety glasses	Release of both fine (~ 250 nm) and coarse (~ 2.1 µm) particles (measured inside enclosing hood w/o ventilation to simulate worst case scenario)
ICP synthesis of nanoparticles	B	4 h / daily	Reactor under 30 to 75 kPa depression	FFP3; lab coat; nitrile gloves; IR and UV safety glasses	No particle emissions
Disconnection of online sampling filter	C	10 min / daily	Two valve system, flanged opening capturing hood	FFP3; lab coat; nitrile gloves; safety glasses	Release of ~ 180 nm particles from dead volume in two valve system
Collection of nanoparticles on online sampling filter	D	30 min / daily	Glove box, gloves worn on interior of glove box	FFP3; lab coat; nitrile gloves; safety glasses	No particle emissions
Cleaning of reactor	E	2 h / weekly	—	FFP3; lab coat; nitrile gloves; safety glasses	—
Windows of view port opened and wiped, interior walls cleaned w/ compressed air	—	60 min	Reactor under 0.4 kPa depression, connected to aspiration	—	No particle emissions
Reactor opened and separated into two sections	—	2 min	Connected to aspiration	—	No particle emissions
Two reactor sections cleaned w/ compressed air	—	30 min	Connected to aspiration, lid w/ slit opening	—	No particle emissions
Interior walls of top reactor section wiped w/ damp cloth	—	30 min	Connected to aspiration	—	No particle emissions
Cleaning of online sampling filter w/ compressed air	F	10 min / weekly	Walk-in ventilated enclosure	FFP3; lab coat; nitrile gloves; safety glasses	Particle release
Cleaning of production filter w/ compressed air	G	3 h / yearly	Walk-in ventilated enclosure	Supplied air, hood type respirator; Tyvek coveralls; Tyvek sleeves; nitrile gloves; shoe covers	Particle release, number concentrations exceeded 226,000 particles/cm^3, particles had mode size of ~ 170 nm, SiC agglomerates found on filter sample by SEM

2.2.1.1 Handling of Silicon Metal Powder Precursor

Before the synthesis of SiC nanoparticles the powder precursor, silicon metal (SIMET 993, Keyvest Belgium SA, Belgium), was handled in an enclosing hood. The manufacturer's specifications of the precursor list a mass median diameter (MMD) of 11 µm. This powder was poured back and forth from its original container into the vessel which empties into the powder feeder. To simulate a worst-case scenario the ventilation of the hood was not turned on. Normally, the ventilation is always on. This simulated work practice was done to determine whether nanoparticles would become airborne in the handling of materials which, from mass based measurements, were assumed to consist of micrometer sized particles. Since there was no ventilation engaged in the hood this was in no way considered a measure of hood effectiveness. To properly evaluate the effectiveness of the enclosing hood the approach of Tsai et al. (2012), where the capture velocity at the particle release site is measured and/or calculated, should be used.

2.2.1.2 Synthesis of Silicon Carbide Nanoparticles

The nanoparticle synthesis prototype consisted of an induction plasma torch coupled to a radio frequency (RF) power supply, a powder feeder, a synthesis chamber, a flow control system, a filtration unit, and a vacuum system (Leconte et al., 2008; Leparoux et al., 2005). A schematic of the ICP reactor is given in Fig. 2.2(a). Precursors, carrier gas, and reactive gas were introduced axially into the induction plasma torch (PL-35, Tekna Plasma Systems Inc., Canada), while the plasma gas (Ar) is introduced with a swirl. Silicon metal powder was used as a precursor and was fed into the torch by a dense phase convey powder feeder (PowderCube, DACS, Switzerland) which could transport non- or poor-

flowable powders (Dvorak and Dietrich, 2001). The induction coil was connected to a RF power supply (Elgotec AG, Switzerland). The torch was mounted atop a stainless steel, water cooled synthesis chamber. Quenching gas was introduced through a quenching ring positioned below the torch. Quenching permitted tailoring of the temperature profile in the reaction chamber which resulted in the control of the particle size distribution. In this case, a quenching rate exceeding 10^8 K/m resulted in SiC particles with a mean diameter of ~ 30 nm. The synthesis chamber was equipped with view ports which allowed for in situ process visualization and characterization.

The synthesis chamber was connected to a specially designed filtration unit. This consisted of an online sampling filter and a production filter. The larger production filter was composed of regenerable metallic high-efficiency particulate air (HEPA) filters and had a filtration surface of 2 m^2. Nanoparticles can be accumulated in the powder collector at the base of the production filter after regeneration. The online sampling filter can be used to bypass the production filter and collect small quantities of nanoparticles on a membrane filter without halting production. A two-valve system was employed at the filter inlets and outlets, allowing both the online sampling filter and the production filter to be disconnected while the filters and the reactor remained sealed (Leparoux and Siegmann, 2003). Nanoparticles were drawn from the synthesis chamber to the filtration unit by a water ring pump with a pressure regulation system which typically maintained a constant process pressure of 15 to 60 kPa. The pump exhaust is also connected to the external air cleaners. For this assessment nanoparticles were collected primarily on the online sampling filter with flow directed to the production filter at the beginning and end of the synthesis.

2.2.1.3 Disconnection of Online Sampling Filter

After nanoparticle production was halted, and appropriate time had elapsed for passivation of nanoparticles, the online sampling filter was disconnected from the reactor prototype, as shown in Fig. 2.2(b). While the two-valve system employed did prevent air movement from or into the filter and reactor, a dead volume existed in the transport line between the valves. Because of this dead volume local exhaust ventilation (LEV) with a flanged opening capturing hood approximately 5 cm in diameter was used in this process. LEV captures contaminants near their source, which is more effective and results in lower equipment and operation costs in comparison with dilution ventilation.

2.2.1.4 Collection of Nanoparticles in Online Sampling Filter

Once disconnected, the online sampling filter was transported to a glove box. The SiC nanoparticles were collected by hand, transferred to well labeled bottles, and then sealed in tight plastic bags under an argon atmosphere. A new pair of nitrile gloves was worn on the interior of the glove box to prevent cross contamination. After the nanoparticles were collected from the surface of the membrane filter, the online sampling filter was reassembled and the outer surface wiped clean.

2.2.1.5 Cleaning of Reactor

It was necessary to clean the interior of the reactor to avoid contamination when one wants to synthesize different products. In cleaning the reactor, first, two aspiration lines were attached to the reactor. When connected to these aspiration lines the reactor was under 0.6 kPa depression. Then view ports were opened, one at a time. With one open view

port, the reactor was under 0.4 kPa depression. The window was then wiped clean directly in front of the opened view port. Thus, any particles released in this cleaning would be captured by the suction of the opened view port. Next, a compressed air gun was inserted through the open view port and used to blow off particles which deposited on the interior walls of the reactor, as shown in Fig. 2.2(c). This process was performed at each view port, proceeding from the top of the reactor to the bottom. Because particles tend to redeposit during cleaning this process may need to be repeated.

The reactor was then opened. Once opened, both aspiration lines were in operation with each section of the reactor having its own aspiration line. The two sections of the opened reactor were separated and a lid with a slit plastic membrane at its center was attached to the bottom section. The compressed air gun was then used to clean the bottom section of the plasma reactor. The compressed air was applied into the particle transport line at the base of the reactor and through the slit in the lid attached to the reactor section, where in the latter instance the particle transport line was closed, as seen in Fig. 2.2(d). This lid was then attached to the top section of the reactor. Again, the compressed air gun was inserted through the lid and the walls were cleaned, as shown in Fig. 2.2(e). Finally, the lid was removed from the top section of the reactor and the interior walls were wiped with a damp cloth, which is demonstrated in Fig. 2.2(f).

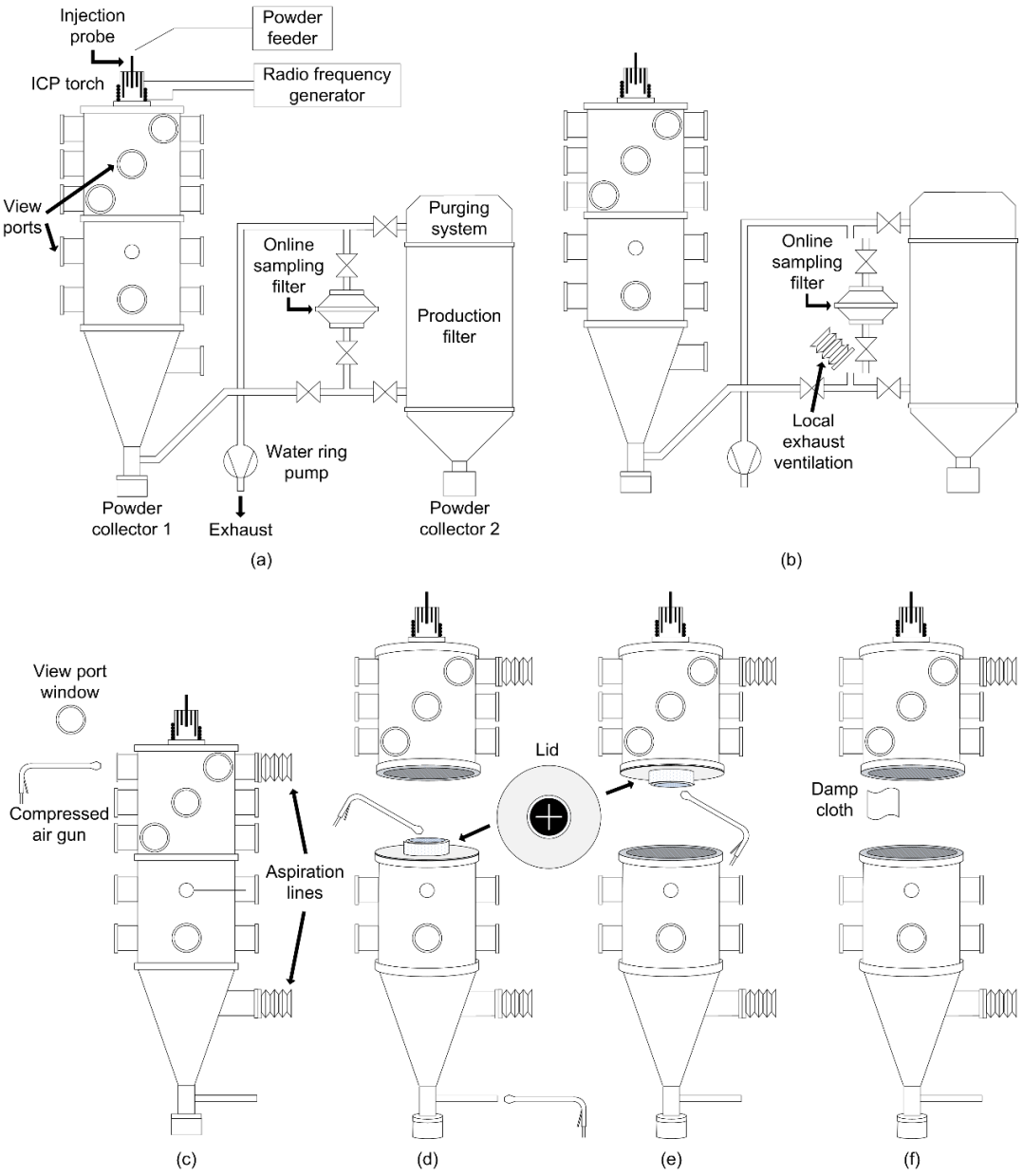

Fig. 2.2 A schematic of (a) the ICP reactor prototype adapted from Leconte et al. (2008), (b) the disconnection of the online sampling filter, and (c – f) the steps taken in cleaning the ICP reactor. (c) An individual view port window was removed and wiped clean. The compressed air gun was used to clean the inside walls of the reactor through the open view port. This was repeated at all viewports. (d) The reactor was split open and a lid with a slit plastic membrane at its center was attached to the bottom section. Compressed air was used to clean the interior of the reactor, first though the particle transport line at the base of the reactor and then through the slit in the lid. (e) The lid was attached to the top section of the reactor and compressed air was applied though the slit in the lid. (f) The lid was removed and a damp cloth was used to clean the interior of the top section of the reactor.

2.2.1.6 Cleaning of Online Sampling and Production Filters

It was also necessary to clean the online sampling and production filters to avoid contaminating future synthesized nanoparticles with the current product. The online sampling filter was cleaned with a compressed air gun in a walk-in ventilated enclosure with flow aligned with the side wall. The worker was upstream of the filter during the cleaning. For this assessment, the production filter was also cleaned in the enclosure using a compressed air gun. While only a small quantity of SiC nanoparticles was collected in the production filter during this assessment, its filtration surface had not been cleaned after prior production runs.

2.2.2 Monitoring Strategy

Task based area measurements were conducted using a suite of direct-reading particle instruments. A handheld CPC (Model 8525, TSI Inc., USA) and Nanoparticle Surface Area Monitor (NSAM) (Model 3550, TSI Inc., USA) were used to measure the particle number concentration and lung deposited surface area concentration, respectively, in the 10 nm to 1 µm size range every second. A Fast Mobility Particle Sizer Spectrometer (FMPS) (Model 3091, TSI Inc., USA) and Aerodynamic Particle Sizer Spectrometer (APS) (Model 3321, TSI Inc., USA) were employed to measure particle size distributions. The FMPS measured electrical mobility diameters in the range of 5.6 to 560 nm every second. The APS measured aerodynamic diameters from 0.5 to 20 µm with a possible time resolution of one second. However, an averaging time interval of 5 or 20 s for the APS was used in this assessment. WPS Commander (WPS Commander 3.0, MSP Corp., USA) was used for analyzing and applying fits to the particle size data. A time series approach was

used to distinguish released engineered nanoparticles from the background. It was assumed that concentrations and size distributions measured during no work activity were the background. Increases in concentration and changes in size distribution during work activity were attributed to a task (Kuhlbusch et al., 2011). The time series approach was combined with a morphological analysis conducted by scanning electron microscope (SEM) (Nova NanoSEM 230, FEI Co., USA). Samples were collected on 47 mm diameter track-etched polycarbonate membrane filters with 0.4 µm pore size (Cat. No. 111107, Whatman plc, UK) housed in an open-faced 47 mm stainless steel filter holder with filter support screen (Cat. No. XX5004710, EMD Millipore, USA).

Instruments and sampling equipment were typically placed on carts and positioned as close to the task being monitored as possible without disrupting the work and were generally within 1 m of the task. The sampling locations corresponding to the tasks listed in Table 2.1 are given in Fig. 2.1. In the monitoring of some tasks approximately 1 m of conductive silicon tubing with a 7.9 mm inner diameter was connected to the inlets of the FMPS and NSAM. This conductive tubing acted as a sampling probe. Being conductive, the electrostatic losses in the tubing were negligible. Diffusion was the major loss mechanism in particle transport through the tube. The nanoparticle diffusional losses calculated by the Gormley and Kennedy (1948) formula were less than 6% for the size ranges of particles measured by the FMPS and NSAM. Thus, no corrections were made for these minimal diffusional losses in the results.

2.3 Results and Discussion

2.3.1 Tasks

2.3.1.1 Handling of Silicon Metal Powder Precursor

When the silicon metal precursor, with a MMD of 11 μm, was handled, a bimodal lognormal size distribution was measured by the FMPS and APS inside an enclosing hood, with one mode, or geometric mean, μ_g, at an electrical mobility diameter, d_B, of 252 nm (geometric standard deviation, σ_g, of 1.45 and coefficient of determination, R^2, of 0.991) and the other at an aerodynamic diameter, d_a, of 2.10 μm (σ_g = 1.70, R^2 = 0.996), as shown in Fig. 2.3. The size distributions measured by the FMPS and APS are presented as a function of electrical mobility diameter and aerodynamic diameter, respectively. No effort was made to relate electrical mobility diameter and aerodynamic diameter using an effective density (Kelly and McMurry, 1992) since this property is material and size dependent (Rao et al., 1995) and its implementation would introduce extra uncertainties.

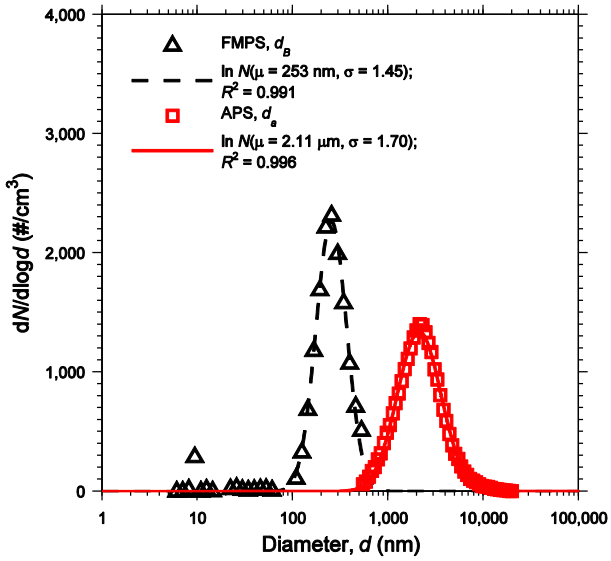

Fig. 2.3 Background subtracted particle size distributions measured by FMPS (in terms of mobility diameter, d_B) and APS (in terms of aerodynamic diameter, d_a) inside an enclosing hood during the handling of metal silicon powder precursor. A 20 s averaging interval was used for the instruments.

While this powder was considered to consist of coarse particles, during handling, both fine and coarse airborne particles were detected. The modes of this size distribution were comparable to those observed in dustiness tests, $d_B \approx 100 – 200$ nm and $d_a \approx 0.8 – 2.5$ µm, for various nanopowders (zinc oxide, Bentonite, nanoclay, titanium dioxide, talc, fumed silica, Goethite, and Y-zirconia) using a rotating drum (Jensen et al., 2008; Schneider and Jensen, 2008; Tsai et al., 2009). The peak measured by the FMPS at around 10 nm was believed to be an artifact of the instrument. Particles of this size would suggest a particle generation event, which one would not associate with the handling of powders. This peak measured by the FMPS has been observed by other researchers in ambient and indoor measurements (Jeong and Evans, 2009) and when challenged with sodium chloride particles (Asbach et al., 2009). They, too, concluded that this may be an artifact of the instrument.

2.3.1.2 Synthesis of Silicon Carbide Nanoparticles

No particle emissions were detected by direct-reading particle instruments during the synthesis of SiC nanoparticles. This was a result of the entire ICP reactor prototype, from powder feeder to filtration unit, being under negative pressure. These results were similar to those in the exposure assessment performed by Lee et al. (2011) at an industrial site where an ICP reactor synthesized silver nanoparticles.

2.3.1.3 Disconnection of Online Sampling Filter

A particle release was detected when the online sampling filter was disconnected from the ICP reactor prototype, as shown in Fig. 2.4(a). These emitted particles were believed to have originated from the dead volume present in the two-valve system which sealed off both the reactor and online sampling filter. The capturing hood which was held near this dead volume as the online sampling filter was disconnected was inadequate for containing the particle release. The FMPS and NSAM, whose probes were held near the online sampling filter as it was disconnected, and the APS, which was adjacent to the reactor, all detected this event. The FMPS measured a bimodal distribution (R^2 = 0.973) with modes present at 6.44 nm (σ_g = 1.63) and 183 nm (σ_g = 1.55), as shown in Fig. 2.5. Again, this sub-10 nm peak was believed to be an artifact of the FMPS. From Fig. 2.4(a) it can be seen the APS measured an increase in particle concentration, as well. These particles were attributed to the tail end of the peak at 183 nm measured by the FMPS.

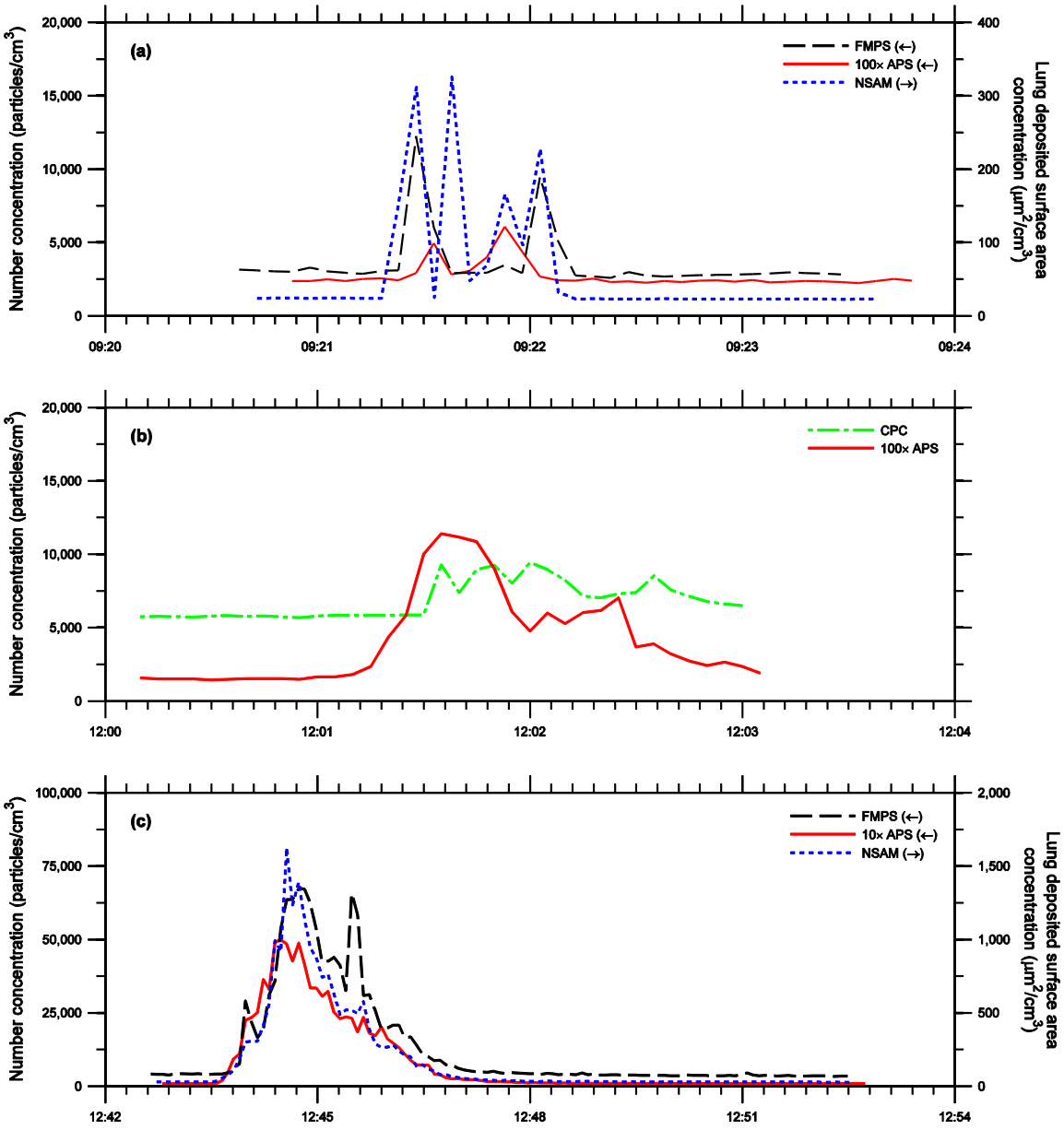

Fig. 2.4 Real-time particle measurements, where the instrument averaging interval was 5 s. (a) Particle number concentrations measured by the FMPS and APS and lung deposited surface area concentrations measured by the NSAM during the disconnection of the online sampling filter. (b) Particle number concentrations measured by the CPC and APS during the cleaning of the online sampling filter. (c) Particle number concentrations measured by the FMPS and APS and lung deposited surface area concentrations measured by the NSAM during the cleaning of the production filter.

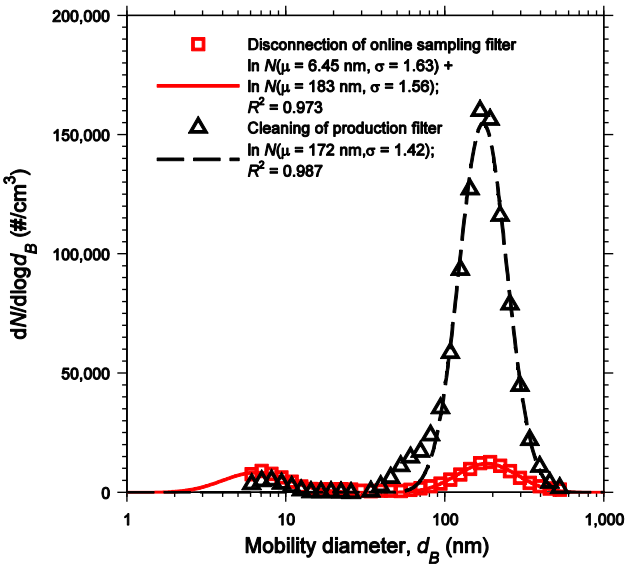

Fig. 2.5 Background subtracted particle size distributions measured by the FMPS (in terms of mobility diameter, d_B) at the peak particle number concentrations during the disconnection of the online sampling filter and the cleaning of the production filter. A 5 s averaging interval was used for the FMPS.

2.3.1.4 Collection of Nanoparticles in Online Sampling Filter

After the online sampling filter was disconnected, it was placed in a glove box where the SiC nanoparticles were collected and packaged in an inert atmosphere. Then the online sampling filter was wiped clean. No particle release was detected as the online sampling filter was removed from the antechamber of the glove box.

2.3.1.5 Cleaning of Reactor

Direct-reading instruments did not provide evidence of particle emissions during the cleaning of the reactor. Adequate aspiration and enclosure was provided by the engineering controls in place to prevent the release of SiC particles. Although no particle release was detected, in the future, as a precautionary measure, LEV will be used near the

slit opening on the lid when compressed air is applied through the particle transport line connected to the bottom section of the reactor, as shown in Fig. 2.2(d).

2.3.1.6 Cleaning of Online Sampling and Production Filters

The cleaning of the membrane filter used in the online sampling filter unit with compressed air in the walk-in ventilated enclosure was found to resuspend the collected SiC particles. This was to be expected, as the entire purpose of this cleaning was to liberate the SiC particles from the filter surface and have the ventilation in the enclosure capture the aerosol. Unfortunately, during this measurement the FMPS was positioned upstream of the cleaning and directly behind the worker. Because of this the FMPS did not measure a particle release. The CPC, which was held near this activity, did measure an increase in particle concentration during cleaning. The APS, too, was able to measure this release, as it was not directly behind the worker. These concentration measurements can be seen in Fig. 2.4(b), where results from the NSAM are not shown due to instrument malfunction.

The cleaning of the production filter was found to be a very dusty process. Particle number and lung deposited surface area concentrations measured by the FMPS and NSAM, respectively, which were transverse to the direction of the ventilation exceeded 67,000 particles/cm^3 and 1,600 μm^2/cm^3, as seen in Fig. 2.4(c), while concentrations measured by the CPC placed downstream of the cleaning exceeded 226,000 particles/cm^3. The liberated particles had a mode size of 172 nm (σ_g = 1.42, R^2 = 0.987). It can be seen in Fig. 2.5 that the particle size distribution was similar to that measured when the online sampling filter was disconnected. Again, what was believed to be an artifact of the FMPS was observed below 10 nm. The particles measured by APS were found to belong to the tail of the

distribution measured by the FMPS. A filter sample collected during the cleaning of the production filter was inspected by SEM revealing the presence of SiC agglomerates, as shown in Fig. 2.6. A summary of the observations resulting from monitoring of the production tasks is given in Table 2.1.

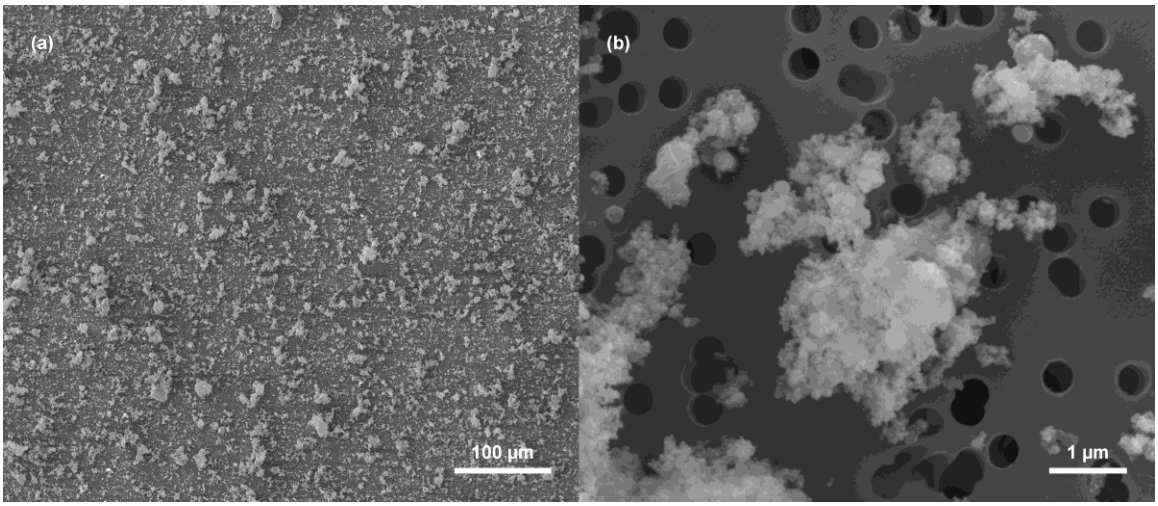

Fig. 2.6 SEM images of SiC agglomerates sampled on a membrane filter with 0.4 µm pores during the cleaning of the production filter at (a) lower and (b) higher magnifications.

2.3.2 Use of Compressed Air in the Cleaning of Nanomaterials

In recommended work practices published by NIOSH, HEPA vacuum or wet wiping methods are recommended when cleaning nanomaterials (NIOSH, 2009). In our study, when compressed air was used for cleaning the inside walls of the reactor, the interior of a semi-closed ventilated system, no particle emissions were detected. When compressed air was used for cleaning in more open spaces, such as the cleaning of the online sampling and production filters in the ventilated walk-in enclosure, emissions of submicrometer particles were identified inside the enclosure. However, the cleaning of the online sampling and production filters only occurs approximately 10 minutes every week

and 3 hours every year, respectively. With few opportunities for exposure and adequate engineering controls and PPE used when completing these tasks, it was determined that it is unfeasible to replace the current standard operating procedure with a new procedure employing HEPA vacuuming.

Few other studies have been conducted where particle emissions were measured when compressed air was used for cleaning nanomaterials. Ogura et al. (2010) measured the release of particles from the filter of a cyclone vacuum cleaner used to collect carbon nanotubes from a substrate when this filter was cleaned in a fume hood, first with a spatula and then a compressed air gun. The CPC measured a concentration increase of approximately 3,000 particles/cm^3, while the optical particle counter exceeded the coincidence loss level of 140 particles/cm^3. Zimmermann et al. (2012) measured the emission of nanoparticles in the cleanout of plasma-enhanced chemical vapor deposition (PECVD) equipment used in the production of silicon nanowires. When an air jet was used to clean the equipment, CPCs measured particle number concentrations 10,000 particles/cm^3 above background with an FMPS measured peak size of 10 nm. In another study, which was conducted at a fullerene factory, compressed air was used to intentionally disperse an open bag of fullerenes resulting in a release of coarse fullerene agglomerates (Fujitani et al., 2008). Similarly, Evans et al. (2013) evaluated a novel Venturi device used to aerosolize fine and nanoscale powders. The air flows were expected to resemble energetic dust dispersion activities, such as the use of compressed air for cleaning. The aerodynamic diameters of the dispersed powders ranged from ~ 300 nm to several micrometers, with no modes below 100 nm. The results of our study reinforce the observations made in workplace simulations. Like these workplace simulation studies, the

reaerosolized particles were in the form of agglomerates larger than 100 nm. This differs from the results of Zimmerman et al. (2012) where a peak size of 10 nm was reported in the case of cleaning PECVD equipment with compressed air.

2.4 Conclusion

The use of direct-reading particle instruments was shown to be an effective means by which to assess efficacy of the engineering controls and best practice guidelines and identify the potential for inhalation exposure in the production of nanoparticles by ICP synthesis. By addressing potential nanoparticle emissions in the design of the engineering controls installed, the work practices performed, and the PPE worn, the processes conducted in this laboratory were safe along all processing steps from the manipulation of the precursor material to the packaging of the final product. No particle release was detected during the synthesis of SiC nanoparticles. This was attributed to the reactor prototype being a closed system operated under slight negative pressure. Similar observations were made during nanoparticle production at industrial sites (Lee et al., 2011), in pilot scale plants (Wang et al., 2012, Wang et al., 2013), and in laboratories (Walser et al., 2012). Tasks related to the synthesis of nanoparticles were also evaluated. A release of submicrometer particles was detected when the online sampling filter was disconnected from the reactor system. Additional LEV has since been installed for this process as a result of this study. The use of compressed air when cleaning nanoparticle contaminated equipment was monitored. When compressed air was used for cleaning the interior of semi-closed ventilated systems, like the inside walls of the reactor, no particle emissions were detected. When compressed air was used for cleaning in open spaces, such as the cleaning

of the online sampling and production filters in the ventilated walk-in enclosure, emissions of submicrometer particles were identified. The cleaning of the production filter resulted in particle number concentrations exceeding 226,000 particles/cm^3. Particle emissions in this facility were found to be mainly submicrometer with a mode size of ~ 170 – 180 nm. Observation of filter samples under SEM confirmed that the particles released in the cleaning of the production filter were agglomerates of SiC nanoparticles.

3 Aerosol Emission Monitoring and Assessment of Potential Exposure to Multi-walled Carbon Nanotubes in the Manufacture of Polymer Nanocomposites

3.1 Introduction

Since engineered carbon nanotubes (CNTs) were first brought to the attention of the scientific community in 1991 (Iijima, 1991), there has been extensive research on the unique properties of this material and their possible applications. The high strength and electrical properties of CNTs have led to their use in numerous applications, including energy storage, semiconductor devices, and conductive composite materials (Baughman et al., 2002). In fact, the worldwide production capacity of CNTs was estimated to be approximately 5 kilotons per year in 2011, a tenfold increase from 2004 (De Volder et al., 2013).

With the proliferation of CNTs has come concern about potential hazards to human health. Recent toxicological studies have suggested that exposure to CNTs may pose a health risk. Length dependent asbestos-like pathogenicity was observed when multi-walled (MWCNTs) were injected into the abdominal cavity of mice (Poland et al., 2008). Murphy et al. (2013) examined three CNT samples of differing lengths and found only the long CNT sample caused acute neutrophilic inflammation in bronchoalveolar lavage at 1 week. However, MWCNTs with a shorter length have also caused adverse health effects in animal studies (Porter et al., 2013; Mercer et al., 2010; Mercer et al., 2011). Sargent et al. (2014) demonstrated that inhalation exposure to MWCNTs can promote the growth of lung adenocarcinoma. Several factors may influence the toxicity of CNTs, including the degree of agglomeration (Wick et al., 2007), surface functionalization (Osmond-Mclead et al., 2011), metal content (Shvedova et al., 2008), and surface wall defects (Muller et al., 2008).

While it has been demonstrated that CNTs may elicit negative health effects, currently there are no enforceable occupational exposure limits for CNTs. In a recent current intelligence bulletin the National Institute for Occupational Safety and Health (NIOSH) (2013b) has proposed a recommended exposure limit (REL) for CNTs and carbon nanofibers of 1 μg/m^3 elemental carbon (EC) as an 8-hour time weighted average respirable mass concentration with the recommended analytical method being NIOSH Method 5040 (NIOSH, 2003a). For comparison, the permissible exposure limit for carbon black is 3,500 times higher (CFR, 2007). The British Standards Institute has suggested a benchmark exposure limit of 0.01 fibers/cm^3, one tenth of the asbestos exposure limit (BSI, 2007).

There are limited data on exposure to CNTs in the workplace. Many of the studies which have been conducted were at research facilities where CNTs were produced (Bello et al., 2008a; Maynard et al., 2004; Methner et al., 2010; Ogura et al., 2010; Tsai et al., 2009) and handled (Johnson et al., 2010; Methner et al., 2010; R'mili et al., 2010) and where advanced composites containing CNTs were produced (Cena and Peters, 2011; Fleury et al., 2011) or machined (Bello et al., 2008b). Additional studies have been conducted at industrial sites where CNTs or products utilizing CNTs were manufactured (Dahm et al., 2012; Dahm et al., 2015; Fonseca et al., 2014; Han et al., 2008; Hedmer et al., 2014; Heitbrink et al., 2015; Ji et al., 2015; Lee et al., 2010; Lee et al., 2014; Lee et al., 2015; Methner et al., 2012a; Takaya et al., 2012; Wang et al., 2011). Only two studies have employed the recommended sampling and analytical method for quantifying the CNT REL. Hedmer et al. (2014) measured respirable EC mass concentrations ranging from <0.08 to 7.4 μg EC/m^3 from personal breathing zone (PBZ) sampling during the

production, sieving, and purification of MWCNTs. Dahm et al. (2015) measured respirable EC PBZ concentrations ranging from <0.02 to 2.94 μg EC/m^3 and an 8-h TWA concentration of 0.16 EC/m^3 at 5 primary and secondary CNT manufacturers. With this lack of personal exposure measurements in primary and secondary manufacturers of CNTs, it is obvious that there is a critical need for further workplace measurements. In this study, potential exposure to MWCNTs was monitored during the manufacturing of polymer nanocomposites where MWCNTs were used as nanofiller. This paper will investigate the volatile nature of the nanoparticles present, address the temporal and spatial variation of particle concentrations in the facility, quantify MWCNT emissions and potential personal exposure, and characterize the morphology of airborne MWCNT structures.

3.2 Methods

3.2.1 Facility and Process Descriptions

Potential exposure was monitored at a secondary MWCNT manufacturer which produced polymer nanocomposites by an extrusion process. The assessment was conducted 04/2010 – 09/2010 and 04/2011 – 08/2011. At this facility, commercially available MWCNTs were used as nanofiller. These MWCNTs produced by chemical vapor deposition processes were more than 95 % pure carbon and contained no detectable amorphous carbon. They had 3 – 15 walls, a mean outer diameter of 13 nm, lengths greater than 1 μm, and were in the form of agglomerates which could be as large as 1 mm. A cobalt impurity was known by the nanocomposite manufacturer to be present in the MWCNTs at a mass fraction of 0.0022 (Personal communication, March 31, 2011). In the extrusion

process, thermoplastic polymer and MWCNT feedstock were fed into a twin-screw extruder, where the polymer was melted and MWCNTs were dispersed throughout the polymer matrix. This mixture was extruded through a die, creating polymer nanocomposite strands, which were cooled in a water bath, passed through a dryer, and cut into pellets. The pellets entered a shaker for size selection and then a cyclone to remove any dust. Finally, the polymer nanocomposite pellets were packaged.

This production facility had the capability to operate continuously, 24 hours a day. Typically, this facility would handle about 5 kg of MWCNTs daily. Two employees actively worked in the manufacturing area. Each would work 12 hour days with alternating 3 and 4 day workweeks. Tasks performed by the employees included the handling of unbound MWCNTs, the cleaning and maintenance of machinery, cleaning of the facility, sampling and testing of nanocomposite for quality control, and the transporting of feedstock and finished product. A large portion of the employees' time was spent at a computer console where processes were monitored and data were entered for record keeping.

The MWCNT feedstock supplied to the extruder was replenished about once every other day. The apparatus which housed the MWCNT feedstock consisted of a drum funnel with a butterfly valve at its end which was attached to the top of an opened MWCNT shipping drum with an O-ring and ring clamp. When the drum was spent, the butterfly valve was closed and the apparatus was removed from atop the MWCNT feedstock feeder. The funnel was unclamped and the funnel and O-ring were taken off. The O-ring, funnel, and interior of the spent drum were cleaned by a vacuum with a high-efficiency particulate air (HEPA) filter. Then a new shipping drum was opened, the O-ring and funnel were

reattached, and the funnel was clamped down. The lid from the newly opened drum was attached to the spent drum. The apparatus was then affixed to the MWCNT feedstock hopper and the butterfly valve was opened. A HEPA vacuum was used to clean the floor in the surrounding area. The entire duration of the transferring procedure was approximately 5 minutes.

This facility had many control measures in place to prevent worker exposure. The nanocomposite production area had a ventilation system which was separate from the rest of the building. The production area was under negative pressure and underwent 15 – 30 air changes per hour. The area was under controlled access, with workers needing clearance to gain entry. Closed-circuit television allowed for remote monitoring of the facility. Handling of unbound MWCNTs and the cleaning and maintenance of MWCNT contaminated equipment was performed inside of strip curtain enclosures where local exhaust ventilation (LEV) was employed. All cleaning of MWCNT contaminated surfaces was done by HEPA vacuum or wet wiping methods. All waste was triple bagged and incinerated. Strip curtains also surrounded electric forklift access doors used to collect packaged nanocomposite product on the first floor and to bring in feedstock on the second floor. Alarms would sound if forklift access doors remained open for extended periods of time. There were sticky mats placed at the exit of the facility. There was a separate gowning room, degowning room, and anteroom, each with interlocked pneumatic sliding doors. The personal protective equipment required inside the manufacturing facility included Tyvek coveralls with hood, shoe covers, nitrile gloves, and full facepiece power air-purifying respirators (PAPR) with organic vapor cartridges and P100 filters. Employees were required to wash their hands after degowning. A layout of the production facility is shown

in Fig. 3.1.

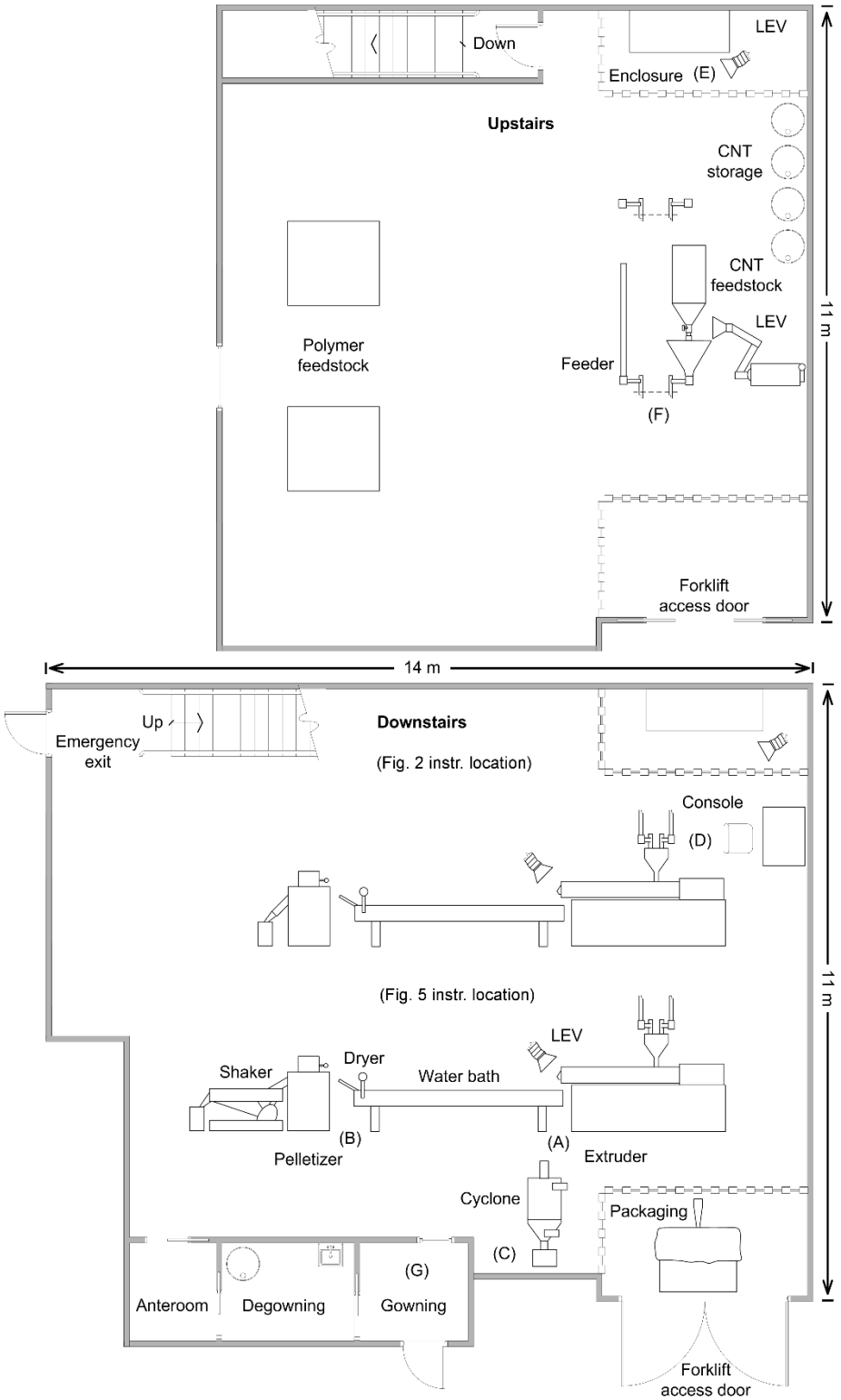

Fig. 3.1 Schematic of polymer nanocomposite production facility with the locations of area measurements given in parentheses.

3.2.2 Monitoring Strategy

The monitoring strategy employed involved task and process based area sampling and measurement by direct-reading instruments, as well as personal breathing zone (PBZ) sampling. Direct-reading instruments and area sampling equipment were typically positioned as close to the task being monitored as possible without disrupting the work and were generally within 1 m of the presumed emission source. The locations where area measurements were performed are labeled in parentheses in Fig. 3.1. Background sampling and measurements were taken for the downstairs and upstairs of the manufacturing facility at the console and in the enclosure (locations D and E, respectively, in Fig. 3.1) on days where no work tasks were done. The durations of the measurements by direct-reading instruments and sampling times for determining these background concentrations were 1 and 1.5 hours, respectively.

3.2.2.1 Direct-reading Instruments

An Engine Exhaust Particle Sizer Spectrometer (Model 3090, TSI Inc., USA) and Nanoparticle Surface Area Monitor (Model 3550, TSI Inc., USA) were used to monitor the temporal evolution of particle size distributions from 5.6 – 560 nm every 0.1 seconds with a 1 second averaging interval and lung deposited surface area concentrations in the alveoli region of the lung every second, respectively, from inactivity in the manufacturing area to steady production from two extruders. A handheld condensation particle counter (CPC) (Model 8525, TSI Inc., USA), Aerosol Particle Sizer (APS) Spectrometer (Model 3321, TSI Inc., USA), DustTrak with a Dorr-Oliver cyclone attached at its inlet (Model 8530,

TSI Inc, USA), and AeroTrak 9000 (Model 9000, TSI Inc., USA) measured task and location based particle number concentrations for particles 20 – 1000 nm in size every second, particle number concentrations for particles 0.5 – 20 μm in aerodynamic diameter every 20 seconds, respirable particle mass concentrations every 20 seconds, and lung deposited surface area concentrations in the alveoli region of the lung every second, respectively. The sampling time at each location typically ranged from 1.5 to 3.5 hours, except for the respirable particle mass concentration measurements at the pelletizer and enclosure which were only for 2 and 30 minutes, respectively, due to instrument error. To investigate the volatility of the particles present during nanocomposite extrusion, a catalytic stripper (CS) was used to condition the aerosol before it entered a Scanning Mobility Particle Sizer (SMPS) Spectrometer consisting of an Electrostatic Classifier (Model 8030, TSI Inc., USA) with a Nano-Differential Mobility Analyzer (Model 3085, TSI Inc., USA) operating at a sheath to aerosol flow ratio of 5 connected to an ultrafine CPC (Model 3025A, TSI Inc., USA) operating in high flow mode for size distribution measurements. The CS removed the semi-volatile, typically organic carbon, fraction by passing the aerosol over an oxidation catalyst heated to 300 °C (Swanson et al., 2013). Four size distribution measurements, each with scanning times of 2 minutes, were made with and without the CS. WPS Commander (WPS Commander 3.0, MSP Corp., USA) was used for analyzing and applying fits to the particle size data.

3.2.2.2 Area and Personal Breathing Zone Sampling

Area samples were positioned at the breathing zone height (1.5 m) using tripod stands (No. 228-502, SKC Inc., USA). Closed face three-piece cassettes were used to

sample total suspended particulate (TSP). For the sampling of respirable particles, aerosol collected by a sampler with 4 μm median cut point (PM_4), the inlet of the three-piece cassette was replaced with an aluminum cyclone (No. 225-01-01, SKC Inc., USA) operated at a flow rate of 2.5 L/min which is specified in NIOSH Method 0600 for the sampling of respirable particles (NIOSH, 2003b). A recently developed personal nanoparticle sampler (PENS) was also employed. Through the use of a respirable cyclone and micro-orifice impactor with cutoff aerodynamic diameter of 100 nm, the PENS was able to simultaneously sample respirable particles at a flow rate of 2 L/min in two separate size selective samples, with $PM_{0.1\text{-}4}$ collected on an impaction surface and $PM_{0.1}$ collected in an after filter housed in a two-piece polycarbonate cassette (Tsai et al., 2012). Sampling in worker's PBZ was conducted as well. Workers wore a respirable particle sampler as described above housed in a filter cassette holder (No. 225-1, SKC Inc., USA) positioned on their chest by clipping it on to the zipper of their Tyvek coveralls. The personal sampling pump (AirChek XR5000, SKC Inc., USA) was attached to their belt-mounted PAPR. The sampling times for area sampling ranged from 0.28 to 24 h with an average of 6.6 h and for PBZ sampling ranged from 1.9 to 4.9 h with an average of 3.7 h. A summary of the sampling times for the area and PBZ sampling is provided in Appendix Table A1.1.

3.2.2.3 OC-EC Analysis

TSP, PM_4, $PM_{0.1\text{-}4}$ and $PM_{0.1}$ area samples (n = 23) and PM_4 PBZ samples (n = 8) were collected for organic carbon (OC) and EC analysis. Samplers were loaded with heat-treated quartz fiber filters (Tissuquartz 2500 QAT-UP, Pall Corp., USA). Three-piece 25 mm conductive cassettes (No. 225-329, SKC Inc., USA) were used for TSP and PM_4

sampling. Closed face sampling at a flow rate of 4 L/min was conducted for the TSP sampling. Such sampling conditions may have resulted in an uneven deposit on the filter (Miller et al, 2013), invalidating the assumption made that the ~1.5 cm^2 punch analyzed was representative of the entire filter. As a result, reported TSP concentrations for OC-EC may be overestimated. Samples were analyzed by Sunset Laboratory Inc. (Tigard, OR) using NIOSH Method 5040 (NIOSH, 2003a). Thermal-optical speciation for the quantification of carbonaceous particles has been applied in several recent exposure assessments (Birch et al., 2011; Dahm et al., 2012; Dahm et al., 2015; Hedmer et al., 2014; Kuhlbusch and Fissan, 2006; Kuhlbusch et al., 2004; Lee et al., 2014; Methner et al., 2007; Ono-Ogasawara et al., 2009; Takaya et al., 2012). The limit of detection (LOD) was assumed to be 0.09 µg EC per cm^2 of filter, the value reported by NIOSH (2013b) for a given as-received 25 mm quartz filter media lot. This LOD can be expressed as an air concentration when multiplied by the filter deposit area and divided by the sampled air volume and for this assessment ranged from about 0.1 to 1 µg EC/m^3. Task-based PM_4 PBZ samples with sampling times ranging from 1.9 – 4.9 h during a 12 h shift were compared to the 8-h TWA REL using two assumptions. One, the 8-h TWA was based on the worst 8 h of exposure during the entire extended work shift as suggested by the Occupational Safety and Health Administration (OSHA) for the evaluation of permissible exposure limits over an extended work shift (OSHA, 1997). Two, the concentrations determined by task-based sampling were representative of the worst 8 hours of exposure.

3.2.2.4 ICP-MS Analysis for Metals

TSP area sampling for trace metal analysis by inductively coupled mass

spectrometry (ICP-MS) was carried out with 37 mm hydrophilic mixed cellulose ester (MCE) filters (GN-4 Metricel, Pall Corp., USA) in closed faced three-piece polycarbonate cassettes (No. M000037A0, EMD Millipore, USA) at a sampling flow rate of 5 L/min. The filter samples (n = 5) were leached in 10 mL of 5 % nitric acid for four hours. ICP-MS was used to estimate the mass concentration of MWCNTs by measuring the mass concentration of cobalt, an impurity present at a known mass fraction. This technique was previously utilized in a study where iron catalyst was used as a descriptor for CNTs (Maynard et al., 2004). The LOD of the ICP-MS sampling method was calculated as three times the standard deviation of cobalt mass in 7 media blanks. Two blanks which had cobalt masses below the instrument detection limit were incorporated by using the Kaplan-Meier method (Helsel, 2010) via the statistical software ProUCL (ProUCL 5.0.00, US Environmental Protection Agency, USA), where the blank cobalt mass was assumed to be normally distributed. The method was found to have an LOD of 2.04 µg of MWCNTs per filter which can be expressed as an air concentration when divided by the sampled air volume.

3.2.2.5 Gravimetric Mass Analysis

Gravimetric measurements were also conducted to determine mass concentrations of area samples (n = 4). Polytetrafluoroethylene filters with a polymethylpentene support ring and diameter of 37 mm (Teflo, Pall Corp., USA) were utilized in three-piece polycarbonate cassettes with the inlet of the cassette replaced with an aluminum cyclone and in the after filter of the PENs for PM_4 and $PM_{0.1}$ sampling, respectively. Silicone impaction surface spray (No. 0100-96-0559A-X, MSP Corp., USA) coated aluminum foil was used as the impaction surface for $PM_{0.1\text{-}4}$. After 24 hours of conditioning in a

temperature and humidity controlled environment, samples were weighed on a microbalance accurate to 1 µg (C-31 Microbalance, Cahn Instruments, Inc., USA).

3.2.2.6 SEM Analysis

Sampling of TSP size fraction was conducted at roughly 2.5 L/min for subsequent analysis by scanning electron microscope (SEM) for the identification and morphological characterization of MWCNT structures. Closed faced, conductive, three-piece cassettes with extended cowls (No. 4376, Pall Corp., USA) suitable for asbestos monitoring were used. Track-etched polycarbonate filters with 0.1 µm pore size and 25 mm diameter (Isopore, EMD Millipore, USA) backed with 5 µm pore size MCE filters (No. SMWP02500, EMD Millipore, USA) and MCE support pads (No. 66238, Pall Corp., USA) were housed inside the cassettes. Roughly 3 mm by 3 mm sections were removed from the center of the filter samples (n = 11) by scalpel, adhered to SEM sample stubs with carbon conductive tape, and then coated with 5 nm of carbon applied by ion-beam sputtering. Samples were observed with a field emission gun SEM (JSM-6500F, JEOL, Japan) where the samples were manually scanned in a serpentine fashion at a magnification of about 10 – 20 nm/pixel to search for MWCNT structures. Identified MWCNT structures were then imaged at higher magnifications (2 – 20 nm/pixel) and the micrographs with resolution of 1280 × 964 pixels were analyzed by the image processing software ImageJ (ImageJ 1.43u, US National Institutes of Health, USA) to calculate equivalent projected area diameters, d_{PA}, and Feret diameters of the structures.

3.3 Results and Discussion

3.3.1 Direct-reading Instruments

The temporal evolution of particle number concentration, lung deposited surface area concentration, and particle size distribution from the 3.5 hours of monitoring of particle emissions during nanocomposite production on 04/08/2010 are shown in Fig. 3.2. During inactivity (period i in Fig. 3.2), when the facility was unoccupied, the particle number and lung deposited surface area concentrations were approximately 10,000 particles/cm^3 and 15 $\mu m^2/cm^3$, respectively. When the manufacturing equipment was being warmed-up (period ii in Fig. 3.2) 10 – 20 nm nanoparticles were generated at number and lung deposited surface area concentrations of around 50,000 particles/cm^3 and 50 $\mu m^2/cm^3$, respectively. When one extruder was operating (period iii in Fig. 3.2) the particle number and lung deposited surface area concentrations were about 50,000 particles/cm^3 and 150 $\mu m^2/cm^3$, respectively, and the mode size observed was about 50 nm. When two extruders were in operation (period iv in Fig. 3.2) nanoparticles with a mode size of about 60 nm and number and lung deposited surface area concentrations of approximately 100,000 particles/cm^3 and 400 $\mu m^2/cm^3$, respectively, were measured. The nanoparticles measured were thought to have been generated by the condensation of polymer fumes produced in this manufacturing process (Wang et al., 2011). Similar concentrations and size distributions were observed in the production of CNT-polymer nanocomposites by melt-molding (Fleury et al., 2011) and in the compounding of nanocomposites using nanoalumina as fillers (Tsai et al., 2008), where in both studies it was suggested that polymer fume particles were the major nanoparticle source. Zhang et al. (2012) and Kuo

et al. (2014) characterized the chemical composition of nanoparticles from thermal cutting of polystyrene foams and showed that the particles were formed by condensing chemical vapors from the high-temperature process.

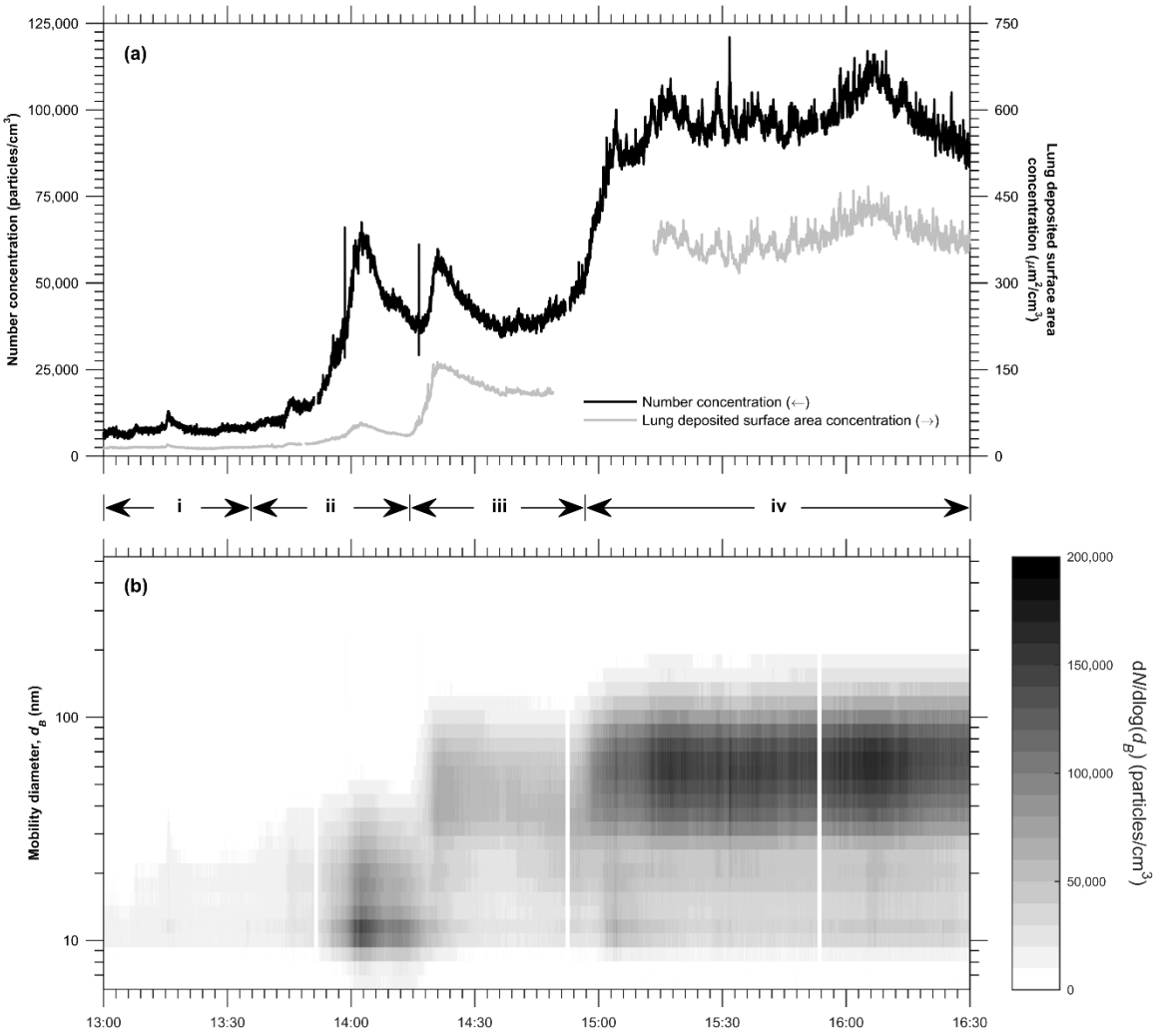

Fig. 3.2 Real-time particle measurements during the production of polymer nanocomposites on 04/08/2010 where time periods i – iv represent i) inactivity, ii) equipment warm-up, iii) operation of one extruder, and iv) operation of two extruders. (a) Time series of particle number and lung deposited surface area concentrations. (b) Time series of particle size distributions.

Direct-reading instruments were unable to detect a MWCNT release in the replenishment of the MWCNT feedstock when unbounded MWCNTs were handled and a

HEPA vacuum was used to clean MWCNT contaminated surfaces. In addition, direct-reading instruments did not distinguish a MWCNT release in the servicing and cleaning of MWCNT contaminated manufacturing equipment. The average particle number concentrations for particles 20 – 1000 nm in size, particle number concentrations for particles 0.5 – 20 μm in aerodynamic diameter, respirable particle mass concentrations, and lung deposited surface area concentration during steady, continuous nanocomposite production, where the respective background concentrations measured during inactivity has been subtracted, at several locations in the production facility are given in Fig. 3.3. It can be seen that the number concentrations measured by CPC and lung deposited surface area concentrations were higher downstairs than upstairs with concentrations downstairs highest near the extruder. This suggests that the extruder was the major source of nanoparticle emissions. During production, the number concentrations measured by APS and mass concentrations at all locations were mostly similar, except for near the cyclone. It is possible that some of the coarse dust which was removed from the surface of nanocomposite pellets by the cyclone were emitted.

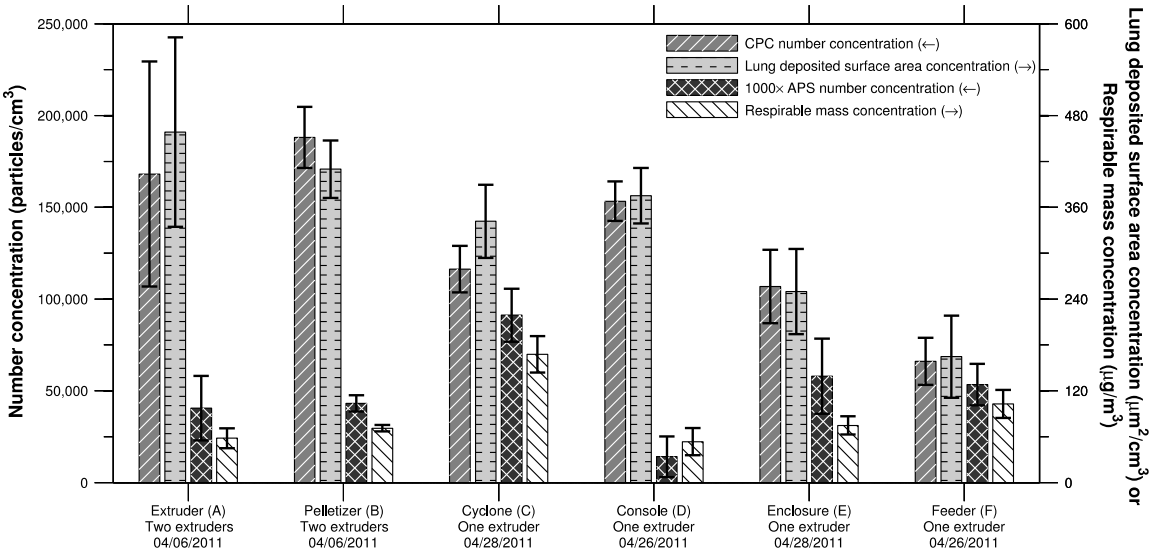

Fig. 3.3 Average particle number concentrations measured by CPC, lung deposited surface area concentrations, particle number concentrations measured by APS, and respirable mass concentrations during steady, continuous nanocomposite production at selected locations in the facility. Error bars represent the standard deviation of concentrations.

The number concentration measured by CPC and lung deposited surface area concentration showed a linear correlation, while the APS measured number concentration linearly correlated with the respirable mass concentration, as shown in Fig. 3.4. This was because both the CPC and AeroTrak 9000 and the APS and DustTrak operate in similar size ranges. While the AeroTrak 9000 and DustTrak measure concentrations weighted by particle size, lung deposited surface area and respirable mass concentrations, respectively, spatial and temporal variations in particle size distributions likely were not great enough to affect this correlation. The Pearson correlation coefficient for the number concentration measured by CPC and lung deposited surface area was r = 0.91 and for the number concentration measured by APS and respirable mass concentration it was r = 0.97. In contrast, the Pearson correlation coefficients for all other instrument combinations were in

the range of r = -0.27 – -0.08 (see Fig. A1.1 in Appendix 1). These results are similar to those reported by Heitbrink et al. (2008) who found that active surface area concentrations correlated strongly with fine particle number concentrations and weakly with respirable mass in the presence of high concentrations of ultrafine particles at an engine machining and assembly facility. Similarly, Park et al. (2010) found that the exposure metrics of surface area concentration and fine particle number concentration, rather than mass concentrations or coarse particle number concentration, agreed with incidental nanoparticle sources and distribution throughout a restaurant and die casting factory.

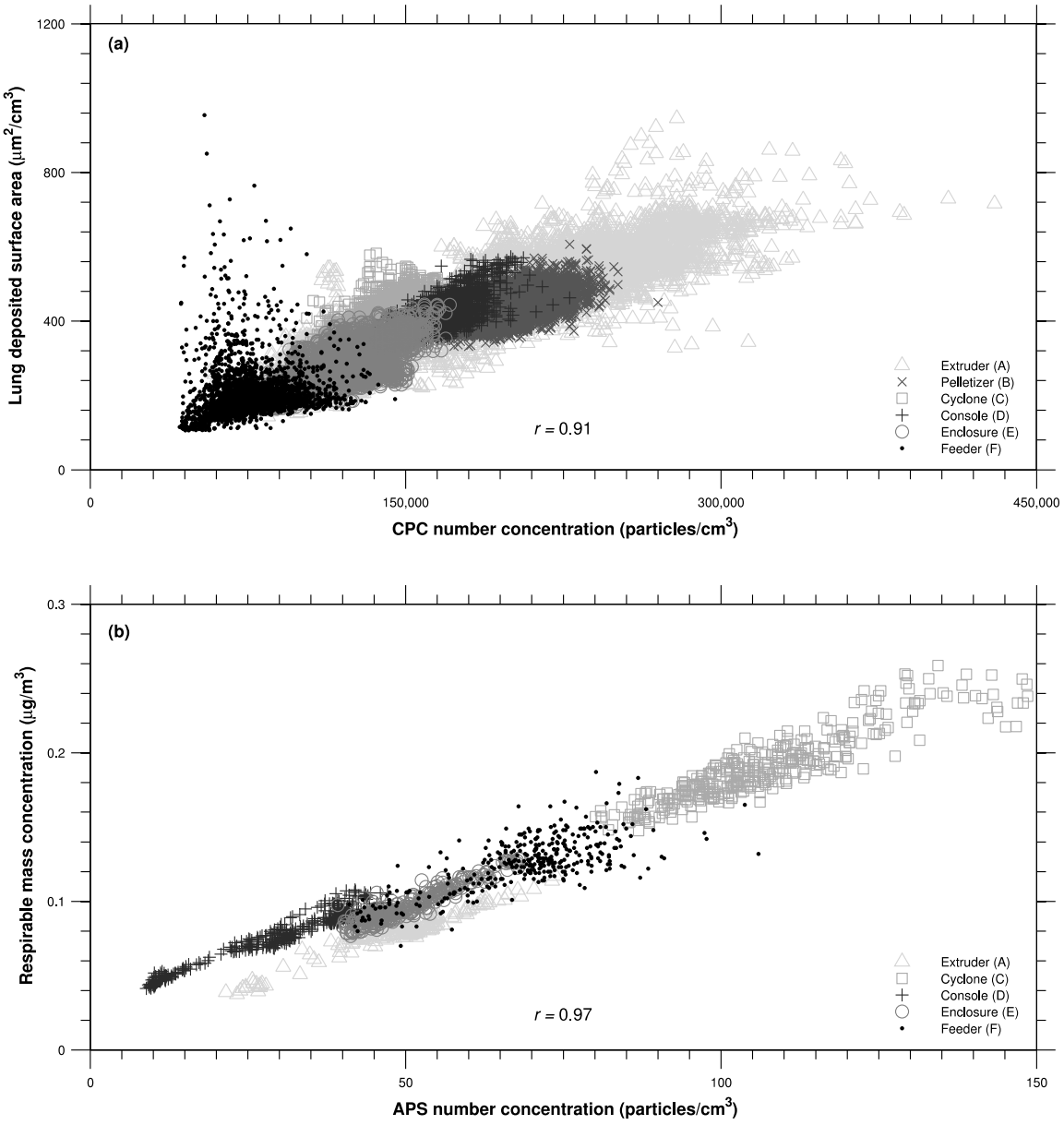

Fig. 3.4 Correlation of (a) particle number concentrations measured by CPC and lung deposited surface area concentrations and (b) particle number concentrations measured by APS and respirable mass concentrations during steady, continuous nanocomposite production at selected locations in the facility.

In Fig. 3.5 the size distributions measured on 05/27/2010 by an SMPS during polymer nanocomposite extrusion with and without a CS at its inlet are shown. Without the CS the size distribution was found to be lognormal with a geometric mean, μ_g, of 47

nm, a geometric standard deviation, σ_g, of 1.7 and a coefficient of determination, R^2, of 0.99. When this aerosol was conditioned by the CS, this mode was no longer present. While the measurement results were not corrected to account for the losses in the CS due to diffusion and thermophoresis, losses alone do not explain the difference in size distributions, as solid particle penetration was found to be 50 % for 10 nm and about 80 % for particles larger than 50 nm for a CS of similar design (Swanson et al., 2013). These results further support the supposition that the major source of nanoparticle emissions in this facility were polymer fume particles, which would be volatized in the CS.

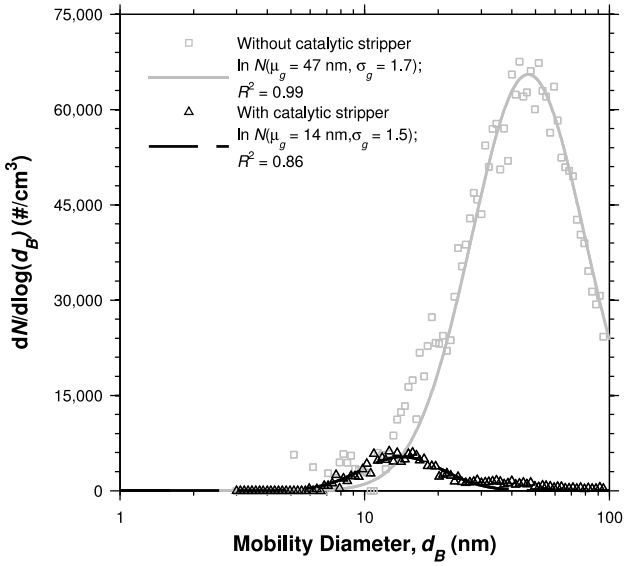

Fig. 3.5 Size distributions measured by SMPS on 05/27/2010 with and without a CS connected to its inlet.

3.3.2 Area and Personal Breathing Zone Sampling

In Table 3.1 an overview of the results from area and PBZ sampling by location and size fraction sampled is given. In this table, the EC and OC mass concentrations determined by NIOSH Method 5040, the estimated MWCNT mass concentration calculated from measured cobalt mass concentration determined by ICP-MS, total

suspended particulate mass concentration determined by gravimetric analysis, and whether or not MWCNTs were found by SEM are given for area samplers for the TSP, PM_4, $PM_{0.1-4}$, and $PM_{0.1}$ size fractions and for PBZ samplers for the PM_4 size fraction. A summary of all monitoring events and their corresponding area and PBZ samples is provided in Table A1.2 in Appendix 1. A more detailed discussion of these results is presented in the subsequent sections.

Table 3.1 Overview of results from area and PBZ sampling by location and size fraction sampled.

			EC (µg EC/m^3)				OC (µg OC/m^3)				MWCNT by ICP-MS (µg/m^3)				Total dust by gravimetric analysis (µg/m^3)				MWCNTs found by SEM	
Location	Activities	Size fraction	n	Min	Max	Mean	n	Min	Max	Mean	n	Min	Max	Mean	n	Min	Max	Mean	n	Yes/ No
Extruder (A)	Production	TSP	1	0.27[a]	0.27[a]	0.27[a]	1	61	61	61	–	–	–	–	–	–	–	–	1	Yes
Pelletizer (B)	Production	TSP	1	2.6	2.6	2.6	1	37	37	37	–	–	–	–	–	–	–	–	3	3× Yes
		PM_4	5	0.09[a]	0.52[b]	0.31[a,b]	5	36	46	39	–	–	–	–	1	60	60	60	–	–
		$PM_{0.1\text{-}4}$	3	0.10[a]	0.58	0.26[a]	3	20	34	26	–	–	–	–	3	29	39	34	–	–
		$PM_{0.1}$	3	0.27[a]	0.96[a]	0.70[a]	3	9.1	14	11	–	–	–	–	3	16	41	25	–	–
Cyclone (C)	Production	TSP	1	0.57[a]	0.57[a]	0.57[a]	1	45	45	45	1	2.7	2.7	2.7	–	–	–	–	1	Yes
Console (D)	Background	TSP	1	0.57[a]	0.57[a]	0.57[a]	1	9.8	9.8	9.8	1	2.8	2.8	2.8	–	–	–	–	1	No
	Production	TSP	1	0.56[a]	0.56[a]	0.56[a]	1	37	37	37	–	–	–	–	–	–	–	–	1	Yes
Enclosure (E)	Background	TSP	–	–	–	–	–	–	–	–	1	2.7	2.7	2.7	–	–	–	–	1	Yes
	Production	TSP	2	0.54[a]	12	6.3[a]	2	38	42	40	1	2.6	2.6	2.6	–	–	–	–	1	Yes (See Fig. 3.6)
		PM_4	1	0.10[a]	0.10[a]	0.10[a]	1	21	21	21	–	–	–	–	–	–	–	–	–	–
		$PM_{0.1\text{-}4}$	1	0.08[b]	0.08[b]	0.08[b]	1	19	19	19	–	–	–	–	–	–	–	–	–	–
		$PM_{0.1}$	1	0.27[a]	0.27[a]	0.27[a]	1	5.7	5.7	5.7	–	–	–	–	–	–	–	–	–	–
Feeder (F)	Production	TSP	1	0.57[a]	0.57[a]	0.57[a]	1	48	48	48	1	2.8	2.8	2.8	–	–	–	–	2	2× Yes
Gowning (G)	Production	TSP	1	0.58[a]	0.58[a]	0.58[a]	1	25	25	25	–	–	–	–	–	–	–	–	–	–
PBZ	Production	PM_4	8	0.47[a]	1.2[a]	0.67[a]	8	19	55	38	–	–	–	–	–	–	–	–	–	–

[a]One or more samples are below the LOD (See Table A1.2)
[a]One or more samples are between the LOD and LOQ (See Table A1.2)

3.3.2.1 OC-EC Analysis

Before reviewing OC results, it should be noted that no corrections were made for artifacts caused by adsorbed organic vapor (Birch, 2004). Although tandem quartz filters were used, the bottom filter was not analyzed for the correction of adsorbed OC vapors due to cost. The highest OC mass concentration collected by TSP area samplers was measured near the extruder, 61 µg OC/m^3. It can be seen that concentrations collected by the TSP samples were similar to those collected by PM_4 area samples. This would indicate the OC particles and adsorbed organic vapor present in the workplace were respirable.

The EC results may have been adversely affected by OC loading which was relatively higher than the EC loading potentially causing a bias in the EC results (NIOSH, 2013b). While adsorbed OC vapor should be accounted for by the analysis of tandem filters (Birch, 2004), which was not done in this study, particulate OC should be accounted for by thermal analysis of the specific particulate OC in question to determine onset of oxidation and confirm complete oxidation (NIOSH, 2013b). It was believed that there were two major types of particulate OC at the workplace: coarse particles mechanically generated by the cutting of nanocomposite at the pelletizer and fine particles formed from the evaporation and subsequent condensation of polymer during the extrusion of nanocomposite. Due to the nondisclosure agreement signed with the nanocomposite manufacturer it was not possible to account for the effect of the mechanically generated particulate OC on the EC results by thermal analysis of the bulk materials which constitute the nanocomposite or the nanocomposite as whole, as Zhao (2013) found that in certain polymer nanocomposites the presence of CNTs can result in a decomposition temperature

lower than that of the bulk polymer. The chemical composition of the fine particles which were generated by condensing polymer vapors likely differed from that of the bulk polymer, as was demonstrated in recent work on the thermal cutting of polystyrene foams (Zhang et al., 2012; Kou et al., 2014).

The impact of adsorbed OC vapor and fine particulate OC from condensed OC vapor on EC results appeared to be minimal since no correlation was observed between measured OC and EC concentrations for the 31 area and PBZ samples (see Fig. A1.2 in Appendix 1). The extent of influence that the mechanically generated nanocomposite particles had on EC results was unclear through examination of the sample set, but the effect should be localized to sampling done near the pelletizer. Due to OC overload and/or polymer pyrolysis, it may not be possible to quantify CNT concentrations by thermal-optical analysis if they are incorporated in a polymer matrix (NIOSH, 2013b). Polymer which does not fully evolve or pyrolyze in the inert atmosphere during thermal-optical analysis would result in a positive bias on EC (Conny et al., 2003). The co-evolution of EC and pyrolyzed carbon formed from the charring of polymer would result in a positive or negative bias on EC depending on the light absorption coefficients of the EC and char (Yang and Yu, 2002).

All but two of the TSP area samples had EC concentrations below the LOD, which was generally about 0.6 µg EC/m^3. The samples taken during production near the pelletizer and inside the curtained enclosure upstairs on 06/30/2011 had EC mass concentrations of 2.6 and 12 µg EC/m^3, respectively. The EC measured near the pelletizer may have originated from the cutting of polymer nanocomposite strands which occurred at this piece of equipment. A number of studies have reported protruding CNTs from polymer particles

after the cutting, sanding, or abrading of nanocomposites (Cena and Peters, 2011; Hellmann et al., 2012; Huang et al., 2012; Ogura et al., 2013; Schlagenhauf et al., 2012). In addition, a couple of studies have observed the release of free individual CNTs and agglomerated CNTs (Huang et al., 2012; Schlagenhauf et al., 2012; Dahm et al., 2015). However, NIOSH Method 5040 would not distinguish between free MWCNTs and MWCNTs in a polymer matrix. The other possible explanation is that this EC was entirely a result of polymer charring during analysis.

Additional area samples were collected at the pelletizer and curtained enclosure where MWCNTs were handled using size selective samplers and larger sampling volumes. No detectable EC concentrations were found on the $PM_{0.1}$ samples, where the LOD was less than 1 µg EC/m^3. Quantifiable $PM_{0.1\text{-}4}$ EC concentrations of 0.58 and 0.11 µg EC/m^3 were measured near the pelletizer on 07/11/2011 and 08/15/2011, respectively. The collocated PM_4 sample on 07/11/2011 was 0.52 µg EC/m^3, above the LOD but below the LOQ, and only differed from the quantifiable $PM_{0.1\text{-}4}$ EC concentration by 10 %, suggesting that the PM_4 EC mass that was sampled consisted of respirable particles larger than 100 nm. All other PM_4 EC concentrations were below the LOD, which was typically less than 1 µg EC/m^3. That all quantifiable $PM_{0.1\text{-}4}$ EC concentrations sampled were less than one quarter of the quantifiable TSP EC concentrations sampled indicated that the TSP samples likely consisted of non-respirable MWCNT agglomerates or non-respirable polymer particles charred during analysis.

Personal respirable samples were analyzed by NIOSH Method 5040. The personal sampling was performed during nanocomposite production, the transferring of unbound MWCNTs, the changing of HEPA and shop vacuum cleaner bags, and the cleaning of

machinery. All task-based PBZ PM_4 samples yielded EC concentrations below the LOD, which was typically less than 1 µg EC/m^3. Using the assumptions that (1) for extended work shifts the REL for CNTs should be based on the worst 8 hours of exposure and (2) that the task-based samples were representative of the worst 8 hours of exposure, it follows that the estimated 8-h TWA was also typically less than 1 µg EC/m^3, the REL for CNTs. PBZ PM_4 OC concentrations were comparable to those measured in area sampling.

Micrometer-sized agglomerates of MWCNTs with outer diameters less than 20 nm, similar to those used in the present study, oxidize at 700 °C (Ono-Ogasawara and Myojo, 2013; Takaya et al., 2012). Examination of the carbon masses detected at each oxidation temperature for NIOSH Method 5040 for the four samples with quantifiable EC concentrations revealed that the two TSP samples had highest EC masses at EC3 and the two $PM_{0.1\text{-}4}$ had highest EC masses at EC5 (see Fig. A1.3 in Appendix 1). EC3 and EC5 are associated with temperatures of 700 °C and 890 °C, respectively (Khan et al., 2011). Even though ambient particulate matter contains EC3 (Ono-Ogasawara and Myojo, 2013), it was believed that this EC3 in the quantifiable TSP area samples was indeed a signature of the MWCNTs used in this workplace due to the fact that both the area TSP sample located near the extruder and the PBZ PM_4 sample collected simultaneously yielded EC concentrations of < 0.27 and < 0.55 µg EC/m^3, respectively. The ratio of EC to total carbon for the TSP samples taken near the pelletizer and in the enclosure, were 0.22 and 0.058, respectively, while the ratios for the two $PM_{0.1\text{-}4}$ collected near the pelletizer on 07/11/2011 and 08/15/2011 were 0.025 and 0.0044, respectively. Because of the low EC to total carbon ratios, the predominance of EC5 in the $PM_{0.1\text{-}4}$ samples may not be due to actual airborne

EC, but instead the high relative OC content, likely mechanically generated polymer particles, may have caused a positive bias in the EC results (NIOSH, 2013b).

The PENS was found to be an effective device for sampling MWCNTs in the workplace with improved sensitivity. Because the PENS collected $PM_{0.1-4}$ using a micro-orifice impactor with a nozzle array with a diameter 6.8 mm, the deposition area is greatly reduced compared to that of 25 or 37 mm filter cassettes (Tsai et al., 2012). The LOD of NIOSH Method 5040 is given in µg EC per cm^2 of filter. By concentrating the mass sampled onto the area of one filter punch, sensitivity is increased. Likewise, although a 37 mm filter was used in the current study, a 25 mm filter could be employed as the after filter of the PENS to reduce the LOD for the $PM_{0.1}$ sample. If one were to use a filter punch which was the same size as the impactor deposition area and a 25 mm after filter, the PENS would be capable of simultaneously detecting concentrations of 0.034 µg EC/m^3 in the $PM_{0.1-4}$ size range and 0.36 µg EC/m^3 in the $PM_{0.1}$ size in a worker's PBZ over an 8-hour workday. It must be noted that although the sum of the $PM_{0.1-4}$ and $PM_{0.1}$ fractions is the health based fraction PM_4, the individual fractions $PM_{0.1-4}$ and $PM_{0.1}$ are strictly technical definitions and not health based fractions.

3.3.2.2 ICP-MS Analysis for Metals

The ICP-MS analysis of area TSP samples did not yield detectable quantities of cobalt. This method for detecting CNTs was found to be difficult to implement for higher purity MWCNTs, even with the increased sensitivities offered by ICP-MS analysis. All analyzed samples had estimated MWCNTs concentrations below the LOD, which was

approximately 3 µg/m^3. This was roughly five times higher than the EC LOD for collocated samples analyzed by NIOSH Method 5040.

3.3.2.3 Gravimetric Analysis

When the OC mass concentrations were compared to the respirable gravimetric mass concentrations, it was seen that the mass sampled consisted largely of OC particulate matter and adsorbed vapor. This further suggested that incidental organic nanoparticles were the major nanoparticle source in this facility.

3.3.2.4 SEM Analysis

Area TSP filter samples were inspected by SEM for the identification of MWCNT structures and the characterization of MWCNT structure morphology. MWCNTs were found on 10 of the 11 samples collected at 6 different locations. Locations and tasks where MWCNTs were detected by SEM include the extruder, console, feeder, cyclone, and pelletizer during nanocomposite production, as well as on samples taken in the curtained enclosure both during production activities and inactivity. This is in contrast to the OC-EC results where EC was only detected in 6 of the 23 area samples collected, those sampled near the pelletizer and in the enclosure, with the caveat that some of those EC results may have been positively biased by the charring of OC particles in analysis. Of the 6 area samples analyzed by OC-EC which were collocated with 5 TSP area samples with MWCNTs detected by SEM, all 4 TSP samples were below the EC LOD of 0.54 - 0.57 µg EC/m^3 while the collocated PM_4 and $PM_{0.1-4}$ samples had detectable EC concentrations of 0.52 and 0.58 µg EC/m^3, respectively. These qualitative results which suggest that electron

microscopy would offer more sensitivity and selectivity in the measurement of CNT exposure than EC analysis are substantiated by the studies of Dahm et al. (2012, 2015) and Hedmer et al. (2014) who quantified CNT number concentrations via electron microscopy on samples collected in parallel with samples whose EC concentrations were below the LOD.

One filter sample collected in the curtained enclosure on 04/28/2011, when unbound MWCNTs were handled and vacuum bags used in the cleaning of MWCNT contaminated surfaces were changed, was found to have more MWCNT structures than the other samples. Consequently, a more detailed morphological analysis of the MWCNT structures found on this sample was conducted. Micrographs of representative MWCNT structures found on this sample are shown in Figs. 3.6(a) – (d). Approximately 60 % of the MWCNT structures observed were loose, ropey agglomerates. About 10 % of the structures appeared to be denser, more compact agglomerates. Another 20 % were either free individual MWCNTs or loose agglomerates where individual MWCNTs were discernible. The remaining 10 % were some combination either amongst the types of MWCNT structures previously described or with other particulate matter. Free individual MWCNTs had a geometric mean Feret diameter of 1.8 μm with a geometric standard deviation of 1.8. Release of free individual CNTs and agglomerated CNTs was also observed in the abrasion of nanocomposite in other studies (Huang et al., 2012; Schlagenhauf et al., 2012). A histogram obtained from a total of 81 MWCNT structures found on this one filter sample is given in Fig. 3.6(e). The particle size distribution was found to be lognormal in nature with a geometric mean projected area diameter of 1.8 μm (σ_g = 2.5 and R^2 = 0.99). Chen et al. (2012) characterized MWCNTs aerosolized using an

acoustic dispersion system for use in animal exposure studies and categorized the MWCNT structures into two fractions, fibrous particles and isometric particles which were MWCNT agglomerates having an aspect ratio of less than 3. While in their case the fibrous particles were more numerous than agglomerates (60 – 80 vs. 20 – 40%), their reported size distributions, with fibrous particles having a geometric mean length of 3.0 µm with geometric standard deviation of 2.2 and isometric particles having a geometric mean diameter of 0.9 µm with geometric standard deviation of 2.0, were fairly representative of the MWCNTs observed in this exposure assessment.

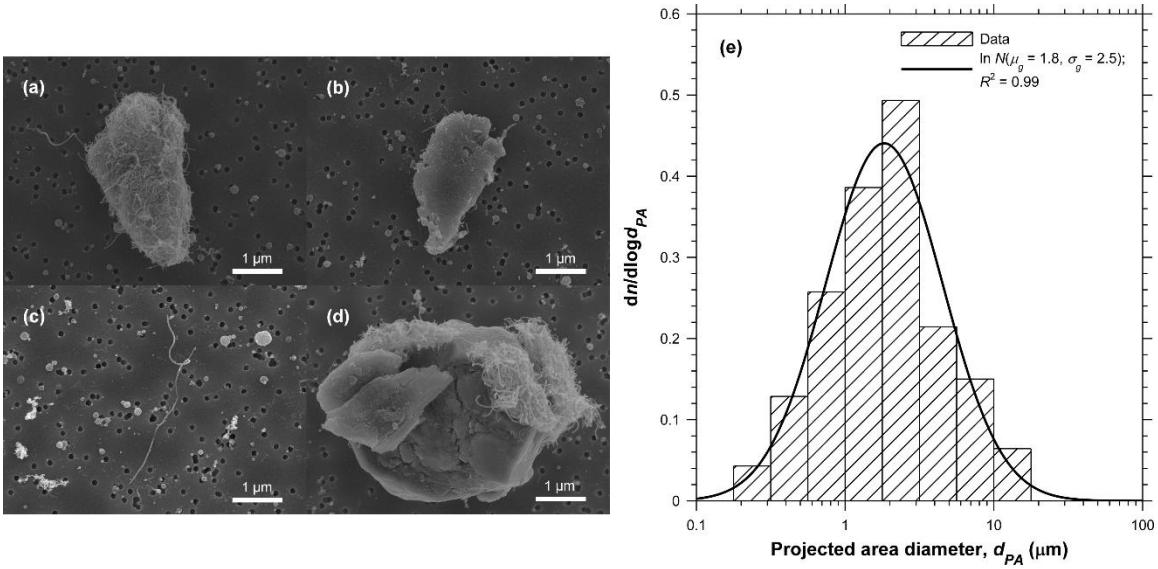

Fig. 3.6 (a – d) Scanning electron micrographs of representative MWCNT structures collected on one filter sample in the enclosure during the transferring of unbound MWCNTs, the changing of bags from vacuums used for cleaning, and the operation of one extruder on 04/28/2011. (a) Approximately 60 % were ropey agglomerates. (b) About 10 % appeared to be denser, more compact agglomerates. (c) 20 % were either free individual MWCNTs or loose agglomerates where individual MWCNTs were discernible. (d) 10 % were some combination either amongst the types of MWCNT structures previously described or other particulate matter. (e) Histogram and calculated lognormal distribution obtained from the projected area diameters, d_{PA}, of MWCNT structures on this sample.

3.4 Conclusions

All eight of the PM_4 PBZ samples had estimated 8-h TWA EC concentrations below the LOD, which was typically less than the REL for CNTs. Analysis of area TSP samples by SEM found MWCNTs on 10 of the 11 samples collected at the extruder, console, feeder, cyclone, pelletizer, and in the curtained enclosure. While some free individual MWCNTs were found, most of the MWCNT structures observed were in the form of ropey, micrometer-sized agglomerates. Nonetheless, it should be noted that the extent to which CNT agglomerates are dispersed once deposited in the lung is presently unknown and that diluted alveolar lining fluid was shown to effectively disperse single-walled CNTs in a biological medium (Wang et al., 2010). Area TSP sampling measured quantifiable EC concentrations indicative of MWCNTs inside the enclosure where unbound MWCNTs were handled and near the pelletizer. However, the TSP EC concentration measured near the pelletizer may potentially be attributable to polymer charring. Area $PM_{0.1\text{-}4}$ samples collected near the pelletizer yielded quantifiable EC concentrations, but this too may be due to polymer charring or the high relative OC content which may have caused a positive bias in the EC result.

It was found that nanoparticle number concentrations were elevated, exceeding 200,000 particles/cm^3, on the manufacturing floor during nanocomposite production. From the results of the OC and gravimetric analyses, as well as the use of a CS at the inlet of an SMPS, it is believed that these nanoparticles consisted largely of organic material and were produced by the heating of the polymer in the extruder. Because of the high OC concentrations measured in this facility, the monitoring of organic vapor concentrations

with sorbent tubes may be pertinent for fully characterizing worker exposure, as potential health effects may be additive or synergistic with co-exposures (Birch, 2011).

4 Collection Efficiency of Submicrometer Aerosol Particles in Electret Filters

4.1 Introduction

4.1.1 Electret Filter Media

An electret is a dielectric material exhibiting a quasi-permanent electrical charge which can produce an external field, making an electret the electrostatic analogue of a permanent magnet (Sessler, 1998). When used in filter media, electrostatic interactions between an electret and aerosol particles can increase the filtration efficiency without an increase in pressure drop. Thus, electret filter media are well-suited for applications which require high particle collection efficiencies and low flow resistances, such as HVAC and respirator filters (Thakur et al., 2013). For details on the charging of nonwoven or fibrous electret filter media, consult Chapter 5 of Brown (1993) and Myers and Arnold (2003).

There are three major electrostatic forces to consider when a particle or fiber carries some charge: dielectrophoretic force, image force, and Coulomb force. The dielectrophoretic force (also known as the induced or polarization force) is present anytime inhomogeneities exist in the electric field. The electric field polarizes the particle, and because the poles are in a non-uniform electric field, a force imbalance acting on the poles results in a net attractive force. The image force is present anytime a particle is charged. Mechanistically, this attractive force is the same as the dielectrophoretic force, except this time the particle polarizes the fiber. It is usually referred to as the image force because the method of image charges is typically used to solve the problem. The Coulomb force is present when both the fiber and particle are charged and is simply the product of the particle charge and the electric field produced by the electret fiber.

4.1.2 Review of Predictive Theoretical Equations for Electret Filter Particle Collection Efficiency

There have been a considerable number of studies which have modeled the filtration efficiency of electret filter media where the three electrostatic forces described above were accounted for to varying degrees. Here, only studies which presented analytical or regression equations for the prediction of particle collection efficiency of a filter composed of bipolarly charged fibers using depth filtration theory will be reviewed. A bipolarly charged fiber is described as having both positive and negative charges with a net charge of zero. In the theories below, bipolarly charged fibers are either assumed as having a circular or rectangular cross-section. The surface charge on cylindrical fibers was assumed to have a line dipole surface charge distribution given by $\sigma \cos(\theta - \theta_0)$ (Brown, 1981), where σ is the surface charge density and θ_0 is an angle between the dipole poles and the gas flow. The electric field around a rectangular cross-section fiber was simulated by summing the contribution of imaginary line charges on each side of the filter (Emi et al., 1987). The flow field around fibers with circular and rectangular cross-sections were described using the solution of Stokes' equation by Kuwabara (1959) and the solution of Oseen's equation for flow past an elliptic cylinder by Tomotika and Aoi (1953), respectively.

Depth filtration theory seeks to link filter collection efficiency on the macroscale to the performance of an idealized, homogeneous collector in the microscale that is representative of the media in aggregate. When the collector is a fiber perpendicular to the flow, the metric used to evaluate the particle collection of the fiber is the single fiber collection efficiency, defined as the ratio of the rate of particle deposition on a fiber per

unit length to the rate per unit length that particles pass through the volume swept by the fiber area (Brown, 1993). The rate of particle deposition on a fiber per unit length is typically determined using one of three methods: limiting trajectories, Brownian dynamics, and the convection-diffusion equation.

The method of limiting trajectories is a deterministic Lagrangian description of particle behavior. Limiting trajectories are the outermost particle trajectories which are still collected by the fiber. Single fiber efficiency can be calculated from the particle flux between limiting trajectories. Additionally, when the forces acting on an inertialess particle are solenoidal, i.e., field divergence is zero everywhere, then particle concentrations along a trajectory remain constant (Robinson, 1956) and the single fiber efficiency can be found analytically from the stream function of the limiting trajectory. Coulomb force is a solenoidal force, meaning that for an inertialess particle suspended in incompressible flow and subject to Coulomb force, the single fiber can be found analytically. This simplification may not always be appropriate because the Coulomb force can never act alone when both particle and fiber are charged. Dielectrophoretic and image forces are also present. When dielectrophoretic and image forces are present particle trajectories must be calculated numerically, barring some simplified limiting cases. If one or more limiting trajectories terminate at a point on the fiber surface where the radial particle velocity is zero, then the filter efficiency is dependent on the finite size of the particle and it is said that particle interception occurs. If not, then the limiting trajectories terminate more than one particle radius away from the fiber surface at a point where particle velocity is zero and there is no effect of particle finite size.

Brownian dynamics is a stochastic Lagrangian description of particle behavior where the particle equation of motion includes particle inertia, the drag and resistance force, external forces, and a randomly fluctuating Brownian force. Typically, single fiber efficiency is related to the numerically evaluated integral of the deposition probability, defined as the ratio of the number of particles deposited from some initial point to the total number of particles generated at this same point, over the boundary of the domain (Podgórski, 2002). When particle inertia is neglected, the single fiber efficiency from the combined effects of fluid flow, electrostatic forces, and diffusion can be determined from an Eulerian frame of reference by solving the convection-diffusion equation with properly selected boundary conditions and calculating the particle flux to the fiber.

Using the method of limiting trajectories, Brown (1981) obtained equations for the single fiber efficiency of inertialess particles captured by a cylindrical electret fiber. For charged particles, only the Coulomb force was considered in the determination of a single fiber efficiency regression equation which was fitted to analytical results for an orientationally averaged fiber. The single fiber efficiency regression equation for uncharged particles captured by dielectrophoretic force was found from numerical results. For both cases, relations were given to estimate when the effect of finite particle size can be neglected, as the equations for single fiber efficiency did not consider particle interception. Since the equations were found by fitting the single fiber efficiency of a filter with a solidity (or solid fraction of the filter) of 0.05, expressions to generalize the results using a method of correlation to recalculate the single fiber efficiency for another solidity were provided. However, Podgórski and Bałazy (2008) reported what could be a computational mistake in the calculation of the correlation's numerical constants.

Pich et al. (1987) provided an analytical solution for the collection of charged particles by a cylindrical electret fiber. The analytical solution, dependent on the orientation of the dipole, was found using the method of limiting trajectories and accounted for both Coulomb force and direct interception acting simultaneously. Using generalized variables, the results are expressed as a universal function which was independent of the type of flow. However, as discussed by Otani et al. (1993), this theory does not account for the existence of a critical interception parameter below which finite particle size has no effect.

Otani et al. (1993) developed regression equations with the intent of bridging the works of Brown (1981), which did not estimate single fiber efficiency above the critical interception parameter, and Pich et al. (1987), which did include the range of interception parameters for which their equation was applicable. For a cylindrical fiber with its dipole perpendicular to the flow, a relation approximating the critical interception parameter was given, above which the equation developed by Pich et al. (1987) for single fiber efficiency could be used. Below the critical value, new approximations of Brown's equation for Coulomb force single fiber efficiency of an orientationally averaged fiber were found for a wider parameter range. Similarly, new approximations of Brown's equation for dielectrophoretic force single fiber efficiency for a wider parameter range were presented.

Lathrache and Fissan (1987) developed theoretical descriptions for the collection of inertialess particles with negligible size (i.e., no interception (Lathrache et al., 1986)) by cylindrical fibers. Kuwabara flow with a slip condition on the fiber was considered (Pich, 1965). From the solution of particle equations of motion, approximate solutions of single fiber efficiency were derived. Coulomb force was considered for charged particles and the

dielectrophoretic was considered for uncharged particles. Unfortunately, it is difficult to find the full derivation of this theory in English. It appears later work was made to incorporate the contribution of interception (Lathrache and Fissan, 1989). This theory, when applied correctly, has been found to agree reasonably well with experimental data (Chang et al., 2015; Chang et al., 2016; Chen et al., 2014).

For electret filter media with a rectangular cross-section, Emi et al. (1987) experimentally and theoretically investigated the combined effects of dielectrophoretic and Coulomb forces on the collection of submicrometer particles. Single fiber efficiency was calculated by method of limiting trajectories and the results were approximated by a regression equation. In addition, a regression equation was developed from experimental results where the number of charges on the particle, particle diameter, and face velocity were controlled to cover a wide range of parameters. The regression equations from theory and experiment had parameters raised to the same power, but differences in coefficients, which were attributed to the uncertainty in the assumed surface charge density and the random orientation of fibers. Kanaoka et al. (1987) performed a similar regression from experimental data which considered Brownian diffusion and dielectrophoretic and Coulomb forces simultaneously. The result was identical to the experimental results of Emi et al. (1987), except for the addition of a term describing the effect of diffusion. Both studies gave regression equations with numerical constants dependent upon the surface charge density of the electret filter, a quantity which is difficult to measure.

Using the results from Brownian dynamics simulations, Podgórski and Bałazy (2008) developed regression equations for the single fiber efficiency of uncharged submicron aerosol particles collected by a cylindrical electret fiber. First collection

efficiencies of an electret filter were determined using Brownian dynamics while considering convection by gas flow, Brownian motion, particle inertia, and dielectrophoresis. Then, the collection efficiencies of a structurally identical, uncharged filter were found. The difference between efficiencies of the electret and mechanical filter was interpreted as the increase in single fiber efficiency attributable to dielectrophoresis. A correlation was developed for this enhancement and a simple approximate rule for recalculating the correlation for another filter solidity was presented. Their results were approximately valid over a wider parameter range than previously developed equations for dielectrophoretic single fiber efficiency. In addition, coupling between dielectrophoresis and Brownian motion was noted for the smallest particles and weakly charged fibers.

As mentioned previously, whenever a particle and fiber are charged, Coulomb and dielectrophoretic forces act simultaneously. Of the studies reviewed above, only Emi et al. (1987) calculated the theoretical single fiber efficiency of a charged particle experiencing both Coulomb and electrophoretic forces. For all other theories, one would have to assume the additivity rule, where the efficiencies calculated for each force independently are superimposed. Emi et al. (1987) and Kanaoka et al. (1987) found a negative interaction between dielectrophoretic and Coulomb forces which would disallow additivity between these collection mechanisms. However, the interaction they found was not so significant because the evaluated filter had a low surface charge density ($3\ \mu C/m^2$ gave the best fit between numerical and experimental results) (Lee et al., 2002). Later, Lee et al. (2002) experimentally found that for an electret filter with an assumed surface charge density of $120\ \mu C/m^2$, a value on par with that measured in highly charged electret media (Li et al.,

2012), additivity between Coulombic capture efficiency and diffusion-dielectrophoretic capture efficiency does not hold.

The one equation in the literature which does account for the interaction between dielectrophoretic and Coulomb forces, that derived by Emi et al. (1987), doesn't include terms dependent on fiber solidity or account for the finite size of the particle. In addition, the disagreement between the coefficients of their regression equations developed from theoretical and experimental results could not be reconciled by the uncertainty of the surface charge density on the fiber alone. They speculate that this may be attributable to the random orientation of rectangular cross-section fibers in the real filter media versus the orientation normal to the flow assumed in the theory.

4.1.3 Objective of Study

It is evident from the reviewed literature that there is a need for a predictive model for the single fiber collection efficiency of charged particles collected by electret filters. The objective of this study was to develop an improved model for the single fiber collection efficiency of a cylindrical fiber with line dipole charge distribution using the method of limiting trajectories. When particles were uncharged the dielectrophoretic force was considered, whereas when they were charged dielectrophoretic, image, and Coulomb forces were considered. Advances in computational power since the development of the limiting trajectory models described above were leveraged to explore a wide parameter space and include the influences of filter solidity, random dipole orientation, particle finite size, dielectrophoresis, image force and Coulomb force. Surrogate models were developed from the numerical results of the limiting trajectories model and validated by comparison

to experimental data where collection mechanisms were isolated through the control of the particle charge state and/or discharging of the electret media.

4.2 Methods

4.2.1 Theory

4.2.1.1 Depth Filtration Theory

From the particle number continuity equation in Eq. (1), the sum of the rate of change of the local particle number concentration N inside control volume dV (or $\delta x \delta y \delta z$) and the net rate that the aerosol flows out of the control surface $d\vec{S}$ must equal zero.

$$\frac{\partial}{\partial t} \oiiint N dV + \oiint N\vec{u} \cdot d\vec{S} = 0 \tag{1}$$

The rate of particle number accumulation is the product of the rate of particle deposition on a fiber per unit length Φ, the fiber length per unit volume L, and the differential volume. Particle inflow and outflow is assumed to only occur in the direction of the gas flow, along δx. Due to the conservation of mass of gas, assuming incompressible flow, the volumetric flow rate through the media is constant and equal to the face velocity U_0 times the cross-sectional differential area $\delta y \delta z$. Eq. (1) can then be rewritten as Eq. (2).

$$\Phi L \delta x \delta y \delta z + \left[-U_0 N \delta y \delta z + U_0 \left(N + \frac{\partial N}{\partial x} \delta x \right) \delta y \delta z \right] = 0 \tag{2}$$

Assuming that fibers are perpendicular to the flow, single fiber collection efficiency is defined as the ratio of the rate of particle deposition on a fiber per unit length to the rate per unit length that particles pass through the volume swept by the fiber area, as seen in Eq. (3), where d_f is the fiber diameter and U is the interstitial gas velocity (Brown, 1993).

$$\eta = \frac{\Phi}{N d_f U} \tag{3}$$

In porous or fibrous media, the interstitial velocity is related to the face velocity U_0 by $U = U_0/(1-\alpha)$ where α is the solidity or solid fraction of the filter. In addition, the fiber length per unit volume this can be written as $L = 4\alpha/\pi d_f^2$. Using the definitions above, the particle continuity equation can be written as a first-order linear partial differential equation, as shown in Eq. (4), as originally suggested empirically by Iwasaki et al. (1937).

$$\frac{\partial N}{\partial x} = -\frac{4\alpha}{\pi(1-\alpha)d_f}\eta N \tag{4}$$

For clean filter media and assuming homogenous solidity and monodisperse fiber diameter, the general solution for $N(x,t)$ can easily be obtained. Particle penetration through the filter media is defined as the ratio of the downstream and upstream particle number concentrations, $P = N(h,t)/N(0,t)$ where h is the thickness of the filter media. By applying the solution for $N(x,t)$ to the definition of penetration Eq. (5a), the equation of aerosol penetration, can be found. As will be discussed in more detail later, the single fiber efficiency will be dependent on the number of charges on the particle, n. In cases where particles hold a probability distribution of charge, $f(n)$, Eq. (5b) can be used to calculate the aerosol penetration for n in the set of integers $\mathbb{Z}$.

$$P = \exp\left(-\frac{4\alpha h}{\pi(1-\alpha)d_f}\eta\right) \tag{5a}$$

$$P = \sum_{n\in\mathbb{Z}} f(n)\exp\left(-\frac{4\alpha h}{\pi(1-\alpha)d_f}\eta(n)\right) \tag{5b}$$

For the calculation of single fiber efficiency in this model, additivity will be assumed between the stochastic (i.e., diffusion) and deterministic (e.g., drag and

electrostatic forces) collection mechanisms, as given by $\eta = \eta_D + \eta_{det}$. This assumption was thought to be acceptable because for charged particles the collection due to Coulomb force should dominate in the size range where diffusion is typically the most prominent mechanical collection mechanism. For uncharged particles, collection due to dielectrophoresis will increase with increasing particle size, while the opposite is true for diffusion.

4.2.1.2 Capture of Particles by Diffusional Deposition

The empirical power law model of Wang et al. (2007) was used to determine the diffusional single fiber efficiency η_D. As seen in Eq. (6), η_D scales with the Peclet number to the power of -0.43, where $Pe = Ud_f/D$ and the diffusion coefficient of the particle is defined as $D = k_B BT$ with k_B being the Boltzmann constant, B particle mobility, and T absolute temperature. Particle mobility is defined as $B = C_c/3\pi\mu_g d_p$ where C_c is the slip correction factor, μ_g is the gas viscosity, and d_p is the particle diameter. The slip correction factor was calculated using the relation obtained by Kim et al. (2005), $C_c = 1 + Kn_p\left[1.165 + 0.483\exp\left(-0.997/Kn_p\right)\right]$ where the particle Knudsen number is defined as the ratio of the gas mean free path λ_g and particle radius, $Kn_p = 2\lambda_g/d_p$. Eq. (6) differs slightly from that given in Wang et al. (2007), since the fiber diameter used in that publication to calculate the penetration, as shown in Eq. (5a), was the pressure drop equivalent fiber diameter $d_{f,R}$ as given by Rubow (1981) in Eq. (7). Rubow calculates the pressure drop Δp across a fibrous filter with an inhomogeneity factor of $\epsilon = 1.65$ using Pich's (1966) expression for a Kuwabara flow field in the slip flow regime where Kuwabara the hydrodynamic factor is $Ku = -1/2\ln\alpha - 3/4 + \alpha - \alpha^2/4$, the coefficient

of slip is given by $\xi = 0.998Kn_f$, and the fiber Knudsen number is defined as the ratio of gas mean free path and the fiber radius, $Kn_f = \lambda_g / R_f$. In addition, Pe was defined in Wang et al. (2007) using the face velocity U_0 and $d_{f,R}$. The formulation of η_D in Eq. (6) allows the use of the traditional definition of Pe and the use of a different fiber diameter when calculating P.

$$\eta_D = 0.84\left(\frac{d_f}{d_{f,R}}\right)^{1.43}[(1-\alpha)Pe]^{-0.43} \tag{6}$$

$$\Delta p = \frac{\mu_g U_0 h}{d_{f,R}^2}\left\{\frac{16\alpha}{\epsilon(1-\alpha)}\frac{(1+2\xi)}{\left[Ku + \xi\left(-\ln\alpha - \frac{1}{2} + \frac{1}{2}\alpha^2\right)\right]}\right\} \tag{7}$$

The power of -0.43 on Pe in Eq. (6) differs from the power of -2/3 typically seen from theories which calculate η_D from particle transport through the fiber boundary layer (Lee and Liu, 1982; Stechkina and Fuchs, 1966). This scaling to the -0.43 power has been hypothesized to arise due to inhomogeneities in fibrous filters from a distribution of fiber diameters (Podgórski, 2009), pinhole leaks (Mouret et al., 2009), or nonuniformity in fiber packing density (Yamada et al., 2011).

4.2.1.3 Capture of Particles by Deterministic Particle Deposition

4.2.1.3.1 Equation of Particle Motion

The equation of motion for an inertialess particle under the influence of drag force and dielectrophoretic, $\vec{F}_{Di}$, image, $\vec{F}_{Im}$, and Coulomb, $\vec{F}_C$, electrostatic forces is given in Eq. (8a). The force balance and the definitions of the electrostatic forces are identical to those used in the model by Baumgartner and Loffler (1987), except in the current model gravitational and inertia forces were excluded.

The fluid flow field was proscribed by the Kuwabara (1959) cell model, Eq. (8b), where Stokes' approximation is used and the boundary conditions applied are no slip on the fiber wall and zero vorticity on the cell boundary, $b = R_f/\sqrt{\alpha}$. Stokes' approximation has been found to be applicable for the prediction of pressure drop across the filter for fiber Reynolds numbers $Re_f = \rho_g U d_f/\mu_g < 0.5$, where ρ_g is the gas density (Kirsch and Stechkina, 1977). The boundary condition of no slip on the fiber wall is applicable to flow in the continuum regime, i.e., $Kn_f < 10^{-3}$ (Pich, 1971).

The dielectrophoretic force, Eq. (8c), was calculated using the equation of Pohl (1958) where ε_0 is the electric constant or permittivity of free space, ε_g, and ε_p are the relative permittivities of the gas and particle, respectively, and $\vec{E}$ is the electric field acting on the particle. The image force is given by Eq. (8d) (Weber, 1965) where ε_f is fiber relative permittivity. Note that in the typical operation of electret filters $\varepsilon_f = 2\sim3.5$ and $\varepsilon_p = 2.5\sim6$, and in this range of fiber and particle relative permittivities it has been found that the image force calculated using Eq. (8d) may be underestimated by 7 to 31%. Eq. (8d)

may be amended by multiplying the right-hand side by a correction factor dependent on ε_f, ε_g, and ε_p which must by calculated numerically (Goel and Spencer, 1975; Jones, 1995). The Coulomb force is simply the product of particle charge q, itself the product of the number of charges on the particle n and the elementary charge e, and $\vec{E}$ as shown in Eq. (8e). The electric field outside of a cylindrical line dipole fiber with a surface charge distribution given by $\sigma\cos(\theta-\theta_0)$ is given by Eq. (8f) (Brown, 1981), where σ is the surface charge density and θ_0 is the angle between the most positively charged part of the dipole and the rear stagnation point, as illustrated in Fig. 4.1.

$$\vec{v} = \vec{u} + B\left(\vec{F}_{Di} + \vec{F}_{Im} + \vec{F}_C\right) \tag{8a}$$

$$\vec{u} = \frac{U}{Ku}\left\{\left[\frac{\alpha-1}{2} + \frac{1}{2}\left(1-\frac{\alpha}{2}\right)\left(\frac{r}{R_f}\right)^{-2} + \ln\left(\frac{r}{R_f}\right) - \frac{\alpha}{4}\left(\frac{r}{R_f}\right)^2\right]\cos\theta\,\hat{\boldsymbol{r}}\right. \\ \left. - \left[\frac{\alpha+1}{2} - \frac{1}{2}\left(1-\frac{\alpha}{2}\right)\left(\frac{r}{R_f}\right)^{-2} + \ln\left(\frac{r}{R_f}\right) - \frac{3\alpha}{4}\left(\frac{r}{R_f}\right)^2\right]\sin\theta\,\hat{\boldsymbol{\theta}}\right\} \tag{8b}$$

$$\vec{F}_{Di} = \left(\frac{\varepsilon_p - \varepsilon_g}{\varepsilon_p + 2\varepsilon_g}\right)\frac{\pi d_p^3 \varepsilon_0 \varepsilon_g}{4}\nabla\left(\vec{E}^2\right) \tag{8c}$$

$$\vec{F}_{Im} = -\left(\frac{\varepsilon_f - \varepsilon_g}{\varepsilon_f + \varepsilon_g}\right)\frac{q^2}{16\pi\varepsilon_0\varepsilon_g\left(r-R_f\right)^2}\hat{\boldsymbol{r}} \tag{8d}$$

$$\vec{F}_C = q\vec{E} \tag{8e}$$

$$\vec{E} = \frac{\sigma}{\varepsilon_0\left(\varepsilon_f+\varepsilon_g\right)}\left[\left(\frac{r}{R_f}\right)^{-2}\cos(\theta-\theta_0)\,\hat{\boldsymbol{r}} + \left(\frac{r}{R_f}\right)^{-2}\sin(\theta-\theta_0)\,\hat{\boldsymbol{\theta}}\right] \tag{8f}$$

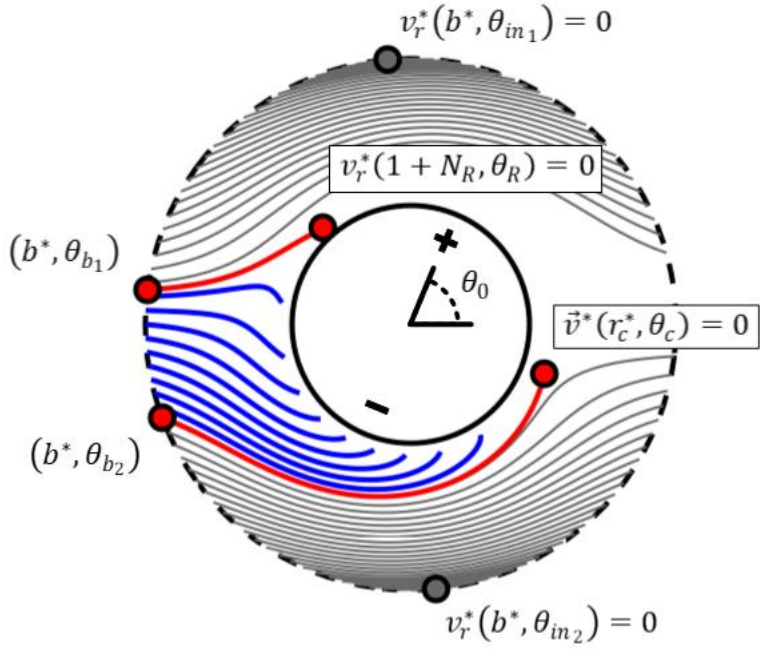

Fig. 4.1 Schematic diagram illustrating the simulation cell for method of limiting trajectories. Points highlighting the bounds of particle inflow on the cell boundary are given. The upper and lower limiting trajectory are examples of grazing and nodal limiting trajectories, respectively.

By applying the nondimensionalization $r^* = r/R_f$ and $t^* = Ut/R_f$ to Eq. (8), the nondimensional radial particle velocity $v_r^*(r^*, \theta) = dr^*/dt^*$and nondimensional angular particle velocity $v_\theta^*(r^*, \theta) = d\theta/dt^*$ are obtained, as shown in Eqs. (9a) and (9b). Particle motion is shown to only be dependent on 5 parameters: θ_0, α, and the dimensionless parameters describing particle capture by dielectrophoretic, image, and Coulomb forces given in Eqs. (9c) – (9e). The inner boundary where particle collision occurs with the fiber is $1 + N_R$ where N_R is the interception dimensionless parameter as defined by Eq. (9f).

$$\frac{dr^*}{dt^*} = \left\{ \frac{1}{Ku} \left[\frac{\alpha - 1}{2} + \frac{1}{2}\left(1 - \frac{\alpha}{2}\right) \frac{1}{r^{*2}} + \ln r^* - \frac{\alpha}{4} r^{*2} \right] \cos\theta \right. \tag{9a}$$

$$\left. - N_{Di} \frac{1}{r^{*5}} - N_{Im} \frac{1}{(r^* - 1)^2} + N_C \frac{\cos(\theta - \theta_0)}{r^{*2}} \right\}$$

$$\frac{d\theta}{dt^*} = \frac{1}{r^*}\left\{\frac{1}{Ku}\left[-\frac{\alpha+1}{2} + \frac{1}{2}\left(1-\frac{\alpha}{2}\right)\frac{1}{r^{*2}} - \ln r^* + \frac{3\alpha}{4}r^{*2}\right]\sin\theta + N_C\frac{\sin(\theta-\theta_0)}{r^{*2}}\right\} \tag{9b}$$

$$N_{Di} = \frac{2}{3}\left(\frac{1-\frac{\varepsilon_g}{\varepsilon_p}}{1+2\frac{\varepsilon_g}{\varepsilon_p}}\right)\frac{\varepsilon_g\sigma^2 d_p^2 C_c}{\varepsilon_0\left(\varepsilon_f+\varepsilon_g\right)^2\mu_g U d_f} \tag{9c}$$

$$N_{Im} = \left(\frac{\varepsilon_f-\varepsilon_g}{\varepsilon_f+\varepsilon_g}\right)\frac{q^2 C_c}{12\pi^2\varepsilon_0\varepsilon_g\mu_g U d_p d_f^2} \tag{9d}$$

$$N_C = \frac{\sigma q C_c}{3\pi\varepsilon_0\left(\varepsilon_f+\varepsilon_g\right)\mu_g U d_p} \tag{9e}$$

$$N_R = \frac{d_p}{d_f} \tag{9f}$$

Particle trajectories were solved numerically using the ode23s algorithm in MATLAB for the solution of stiff problems (Shampine and Reichelt, 1997). The equations for the Jacobian matrix were supplied to the solver to improve calculation reliability and efficiency. For the parameter space investigated in this study, it was found that a relative error tolerance of 10^{-7} and an absolute error tolerance of 10^{-7} for each solution component, r^* and θ, and an interval of integration for t^* with duration less than or equal to 10^7 provided satisfactory results.

4.2.1.3.2 Calculation of Deterministic Single Fiber Efficiency

The rate of particle deposition on a fiber per unit length Φ is defined in Eq. (10a) as the flux of particles into the closed contour $\vec{s}$ surrounding a fiber. Recall that N is the particle concentration along the depth of the filter. $\mathbb{P}_f$ is defined as the probability that

particles entering $\vec{s}$ are deposited on the fiber. $\widetilde{N}$ is defined as the local particle concentration along $\vec{s}$ normalized by N. This formulation is similar to that given by Banks and Kurowski (1983). The average local concentration of particles entering the flow cell along the contour $\vec{s}$ is assumed to be equal to N as stated in Eq. (10b) where $\mathbb{P}_{in}$ is the probability that particles along $\vec{s}$ enter the flow cell and s is the total length of the contour.

$$\Phi = -N \oint \mathbb{P}_f \widetilde{N} \vec{v} \cdot d\vec{s} \tag{10a}$$

$$\frac{1}{s} \oint \mathbb{P}_{in} \widetilde{N} ds = 1 \tag{10b}$$

If the contour coincides with the boundary of the flow cell, the differential becomes $d\vec{s} = \hat{r} b d\theta$. After plugging Eq. (10a) with this $d\vec{s}$ into the relation for single fiber efficiency in Eq. (3) and applying nondimensionalization, one arrives at the definition of the deterministic single fiber η_{det} in Eq. (11a) where $b^* = 1/\sqrt{\alpha}$. The probability $\mathbb{P}_f$ was assumed to be unity between the intersections of the upper and lower limiting trajectories with the contour at points $\left(b^*, \theta_{b_1}\right)$ and $\left(b^*, \theta_{b_2}\right)$ and zero everywhere else, as shown in Eq. (11b). The probability $\mathbb{P}_{in}$ was assumed to be unity between the upper and lower points on the cell boundary where particle radial velocity was zero, $\left(b^*, \theta_{in_1}\right)$ and $\left(b^*, \theta_{in_2}\right)$, with the probability being zero everywhere else, as given in Eq. (11c). A schematic demonstrating the flow cell and these angles is shown in Fig. 4.1.

$$\eta_{det} = -\frac{b^*}{2} \int_0^{2\pi} \mathbb{P}_f \widetilde{N} v_r^* d\theta \Big|_{r^*=b^*} \tag{11a}$$

$$\mathbb{P}_f\big|_{r^*=b^*} = \begin{cases} 1, & \text{if } \theta_{b_1} \le \theta \le \theta_{b_2} \\ 0, & \text{otherwise} \end{cases} \tag{11b}$$

$$\mathbb{P}_{in}|_{r^*=b^*} = \begin{cases} 1, & \text{if } \theta_{in_1} \leq \theta \leq \theta_{in_2} \\ 0, & \text{otherwise} \end{cases} \tag{11c}$$

$$\widetilde{N}\big|_{r^*=b^*} = \begin{cases} 1, & \text{if } \theta_{in_1} \leq \theta \leq \theta_{in_2} \\ \text{undefined}, & \text{otherwise} \end{cases} \tag{11d}$$

It was assumed that the contour was sufficiently upstream of the fiber so that the normalized particle concentration was unity everywhere in the region of particle inflow on the cell boundary $\widetilde{N}$, as shown in Eq. (11d). A criterion for the assumption of uniform particle concentration due to adequate mixing by diffusion between fiber layers is given in the literature as $2Dh_1/U\left(d_f\eta\right)^2 \geq 1$ (Brown, 1993; Kirsch and Stechkina, 1977). This criterion is equivalent to the Fourier number, which in mass transfer is defined as the ratio of the species diffusion rate to the rate of species storage, $Fo = Dt/L_D^2$ (Incropera et al., 2007) If the time considered is the time it takes for a particle to travel one half of the inter-fiber spacing h_1, then roughly $t = h_1/2U$. If characteristic length L_D is taken as the height of the limiting trajectory at the cell boundary y, which can be related to single fiber efficiency for particle capture by mechanical means, then $L_D = y = \eta d_f/2$. It is unclear whether this criterion would be informative for particle capture by electrostatic forces. Due to attractive forces, limiting trajectories can trace paths downstream of the rear stagnation point before being captured. In addition, particle migration velocities due electrostatic forces may make the choice of the interstitial gas velocity U as a characteristic velocity not ideal. Finally, as demonstrated in Eq. (11a), when electrostatic forces are considered there is not a direct correspondence between the height of the limiting trajectory and single fiber efficiency. Nevertheless, this criterion will be considered during analysis, since Chang et al. (2016) showed some evidence that it could be linked to model applicability.

After plugging v_r^* from Eq. (9a) into the relation for η_{det} in Eq. (11) and evaluating the integral, the equation for η_{det} in Eq. (12) is found.

$$\eta_{det} = \left[-\frac{1}{2\sqrt{\alpha}} \sin\theta + \left(\frac{\alpha^2 N_{Di}}{2} + \frac{\sqrt{\alpha} N_{Im}}{2\left(1-\sqrt{\alpha}\right)^2} \right) \theta \right. \\ \left. - \frac{\sqrt{\alpha} N_C}{2} \sin(\theta - \theta_0) \right]_{\theta_{b_1}}^{\theta_{b_2}} \tag{12}$$

When the particle is uncharged Eq. (12) simplifies to the equation for the deterministic single fiber efficiency of a line dipole fiber collecting an uncharged particle $\eta_{\sigma 0}$ as given in Eq. (13a). The orientationally averaged deterministic single fiber efficiency of a line dipole fiber collecting a charged particle $\eta_{\sigma q}$ is given by Eq. (13b). The integral was evaluated via an adaptive quadrature in MATLAB with relative and absolute tolerances of 10^{-3} and 10^{-13}, respectively (Shampine, 2008).

$$\eta_{\sigma 0}(\alpha, N_R, N_{Di}) = \frac{1}{\sqrt{\alpha}} \sin\theta_b + \alpha^2 N_{Di}(\pi - \theta_b) \tag{13a}$$

$$\eta_{\sigma q}(\alpha, N_R, N_{Di}, N_{Im}, N_C) \tag{13b}$$

$$= \frac{1}{\pi} \int_0^{\pi} \left[-\frac{1}{2\sqrt{\alpha}} \sin\theta + \left(\frac{\alpha^2 N_{Di}}{2} + \frac{\sqrt{\alpha} N_{Im}}{2\left(1-\sqrt{\alpha}\right)^2} \right) \theta \right. \\ \left. - \frac{\sqrt{\alpha} N_C}{2} \sin(\theta - \theta_0) \right]_{\theta_{b_1}(\theta_0)}^{\theta_{b_2}(\theta_0)} d\theta_0$$

In depth filtration theory, the penetration through the filter decreases exponentially, but is always finite (Brown, 1993). However, in the model for $\eta_{\sigma 0}$ described above, if $\theta_b \leq \pi/2$, then all particles would be captured in the first layer of the filter. In this case surface

filtration would be occurring, not depth filtration. This is analogous to the requirement in Eq. (14) which ensures a filter doesn't behave as a sieve.

$$1 + N_R < \frac{1}{\sqrt{\alpha}} \tag{14}$$

This puts a theoretical maximum value on $\eta_{\sigma 0}$ at a given α, N_R, and N_{Di} for which depth filtration is still valid. By plugging $\theta_b = \pi/2$ into Eq. (13a), the inequality given in Eq. (15a) is obtained. Similarly, for $\eta_{\sigma q}$ if $\theta_{b_1}(\theta_0) \leq \pi/2$ and $\theta_{b_2}(\theta_0) \leq 3\,\pi/2$ for $0 \leq \theta_0 \leq \pi$, depth filtration will be invalid. The maximum possible value for $\eta_{\sigma q}$ would be at $\theta_0 = 0$. The inequality in Eq. (15b) is found after plugging $\theta_{b_1} = \pi/2$, $\theta_{b_2} = 3\,\pi/2$, and $\theta_0 = 0$ into Eq. (13b).

$$\eta_{\sigma 0}(\alpha, N_R, N_{Di}) < \frac{1}{\sqrt{\alpha}} + \frac{\pi}{2}\alpha^2 N_{Di} \tag{15a}$$

$$\eta_{\sigma q}(\alpha, N_R, N_{Di}, N_{Im}, N_C) < \frac{1}{\sqrt{\alpha}} + \frac{\pi}{2}\left[\alpha^2 N_{Di} + \frac{\sqrt{\alpha} N_{Im}}{\left(1 - \sqrt{\alpha}\right)^2}\right] + \sqrt{\alpha} N_C \tag{15b}$$

4.2.1.3.3 Determination of Limiting Trajectories

To calculate the deterministic single fiber, one must successfully detect the limiting trajectories. Nielsen (1978) identifies two types of limiting trajectories: grazing limiting trajectories and nodal limiting trajectories. Grazing limiting trajectories terminate one particle radius away from the surface of a fiber at a point where Eq. (16a) is satisfied (Banks and Kurowski, 1983). Nodal limiting trajectories end at a point more than one particle radius away from the fiber surface where Eq. (16b) is satisfied (Nielsen, 1978). An illustration of the two types of limiting trajectories is given in Fig. 4.1.

$$v_r^*(1 + N_R, \theta_R) = 0 \tag{16a}$$

$$\vec{v}^*(r_c^*, \theta_c) = 0 \tag{16b}$$

To ensure that limiting trajectories exist within the Kuwabara flow cell, the inequality $v_r^*(b^*, 0) > 0$ for $\theta_0 = \pi$, or written alternatively as Eq. (17), must be satisfied.

$$1 - \alpha^{5/2} N_{Di} - \frac{\alpha}{\left(1 - \sqrt{\alpha}\right)^2} N_{Im} - \alpha N_C > 0 \tag{17}$$

Candidate limiting trajectories were identified by finding the roots of Eqs. (16a) and (16b), either analytically, when possible, or numerically using the Chebfun open-source package for MATLAB which can find multiple roots via Chebyshev expansion (Driscoll et al., 2014). From the locations of these roots, plus a very small numerical jitter to avoid the particles getting stuck at a stationary point in the particle velocity field, backwards particle trajectories were calculated. If these trajectories intersected the outside boundary of the flow cell, the angle at which this intersection occurred was saved. Forward particle trajectories were then calculated from the cell boundary at angles slightly smaller or larger than the minimum and maximum of the saved angles, respectively. This search was repeated at angles further away from the extrema until both the upper and lower trajectories exited the flow cell without colliding with the fiber. Then a binary search method was used between pairs of misses and hits of the upper and lower limiting trajectories until either the relative error for the deterministic single fiber efficiency between iterations was less than 10^{-4} or the difference in angle at the boundary between a hitting and missing trajectory was less than or equal to two times floating-point relative accuracy.

4.2.2 Development of Surrogate Models

Section 4.2.1 described the development of a numerical model to calculated the deterministic single fiber efficiency of electret filter media. To allow others to exploit the results of this numerical model, a surrogate model was developed. The goal was to cover a wide range of filter, operational, and particle properties that one may encounter in the operation of electret filters. The approximate range of properties considered and the range of nondimensional parameters which correspond to this range of properties is given in Eq. (18).

$$\left.\begin{array}{c} \alpha = 0.01 - 0.25 \\ d_f = 1 - 100\ \mu\text{m} \\ \sigma = 0 - 1000\ \mu\text{C/m}^2 \\ \varepsilon_f \sim 2 \\ U_0 = 0.01 - 1\ \text{m/s} \\ d_p = 1 - 1000\ \text{nm} \\ q = 0e - 10e \\ \varepsilon_p \sim 5 \end{array}\right\} \Rightarrow \begin{cases} \alpha = 0.01 - 0.25 \\ N_R = 10^{-5} - 1 \\ N_{Di} = 10^{-14} - 10^{5} \\ N_{Im} = 10^{-11} - 10^{2} \\ N_C = 10^{-7} - 10^{2} \end{cases} \tag{18}$$

Based on the input nondimensional parameters, the surrogate model was to determine whether depth filtration theory is valid using K-nearest neighbors (KNN) classification and, if so, estimate the deterministic single fiber efficiency using KNN regression. Both KNN classification and regression were accomplished using the Python machine learning module scikit-learn (Pedregosa et al., 2011). Numerical datasets were separated into training, validating, and testing sets. The models were initially fit with the training set, which consisted of 70% of the data. In the validation step, hyperparameters, parameters which the user must input prior to training, were optimized using 15% of the data. Finally, the remaining 15% of the data was used to test the overall effectiveness of the models.

Training, validating, and testing data input feature spaces for the uncharged particle models, $\boldsymbol{x}_{\sigma 0}$, and charged particle models, $\boldsymbol{x}_{\sigma q}$, were of the forms given in Eqs. (19a) and (20a), respectively, provided the conditions in Eqs. (14) and (17) were met. The target values for classification for the uncharged and charged particle models, $y_{\sigma 0,class}$ and $y_{\sigma q,class}$, are shown in Eqs. (19b) and (20b). For samples where the classification target value equaled unity, Eqs. (19c) and (20c) were used to calculate the target values for regression, $y_{\sigma 0,regr}$ and $y_{\sigma q,regr}$, respectively.

$$\boldsymbol{x}_{\sigma 0} = \ln([\alpha \quad N_R \quad N_{Di}]) \tag{19a}$$

$$y_{\sigma 0,class} = \begin{cases} 0, & \text{if } \theta_b \leq \dfrac{\pi}{2} \\ 1, & \text{otherwise} \end{cases} \tag{19b}$$

$$y_{\sigma 0,regr} = \ln\left(\frac{\pi}{\theta_b} - 1\right) \tag{19c}$$

$$\boldsymbol{x}_{\sigma q} = \ln([\alpha \quad N_R \quad N_{Di} \quad N_{Im} \quad N_C]) \tag{20a}$$

$$y_{\sigma q,class} = \begin{cases} 0, & \text{if } \theta_{b_1} \leq \dfrac{\pi}{2} \text{ and } \theta_{b_2} \geq \dfrac{3\pi}{2} \text{ for all } \theta_0 \\ 1, & \text{otherwise} \end{cases} \tag{20b}$$

$$y_{\sigma q,regr} = \ln(\eta_{\sigma q}) \tag{20c}$$

To ensure that prior to weighting all features contributed approximately proportionally to the distance used to determine the nearest neighbors, the ranges of all features were rescaled using Eq. (21).

$$x'_m = \frac{x_m - x_{m,min}}{x_{m,max} - x_{m,min}} \tag{21}$$

Then the weighted Euclidean distance between samples i and j of M-dimensional feature space was computed by Eq. (22a), where w_m is the weight applied to feature m and, as shown in Eq. (22b), the sum of all weights is one.

$$d_{ij} = \sqrt{\sum_{m=1}^{M} w_m \left(x'_{i,m} - x'_{j,m}\right)^2} \tag{22a}$$

$$\sum_{m=1}^{M} w_m = 1 \tag{22b}$$

The predicted regression target $\hat{y}_{regr_i}$ of sample i was calculated in Eq. (23) as the weighted average of the K nearest training target values y_{regr_k} weighted by the inverse of the distance defined in Eq. (22a).

$$\hat{y}_{regr_i} = \frac{\sum_{k=1}^{K} \frac{1}{d_{ik}} y_{regr_k}}{\sum_{k=1}^{K} \frac{1}{d_{ik}}} \tag{23}$$

Similarly, the predicted classifier target $\hat{y}_{class_i}$ of sample i was found using Eq. (24). Here the weighted average of the K nearest training target values y_{class_k} weighted by the inverse of the distance is mapped to one of the two classes. Because there are an even number of classes, K is an odd number to avoid a tie.

$$\hat{y}_{class_i} = \begin{cases} 0, & \text{if } \dfrac{\sum_{k=1}^{K} \frac{1}{d_{ik}} y_{class_k}}{\sum_{k=1}^{K} \frac{1}{d_{ik}}} < \dfrac{1}{2} \\ 1, & \text{if } \dfrac{\sum_{k=1}^{K} \frac{1}{d_{ik}} y_{class_k}}{\sum_{k=1}^{K} \frac{1}{d_{ik}}} > \dfrac{1}{2} \end{cases} \tag{24}$$

For the uncharged particle models, the training set consisted of a grid uniformly spaced in feature space $\boldsymbol{x}_{\sigma 0}$ (logarithmically spaced in α, N_R, and N_{Di} parameter space) with 20 samples per decade. The minimum and maximum values of α, N_R, and N_{Di} equaled that listed in Eq. (18). The validation and test data were generated by draws of random

numbers uniformly distributed in feature space $\boldsymbol{x}_{\sigma 0}$ and having the same extent as the training data. The number of training, validation, and testing samples for the uncharged particle models, as well as the extrema of each feature needed for the scaling in Eq. (21), is given in Table 4.1.

For the charged particle models, samples were generated using four different methods. First, a 5-dimensional convex hull was constructed from feature space $\boldsymbol{x}_{\sigma q}$ generated by the range of relevant electret filter operation properties given Eq. (18) using the Qhull algorithm (Barber et al., 1996). In Method 1, a grid of about 190k total samples uniformly spaced in feature space (logarithmically spaced in α, N_R, N_{Di}, N_{Im}, and N_C parameter space) with 20 samples per decade for feature α and one sample per decade for all the other features was searched inside of this convex hull, with the MATLAB File Exchange function Inhull (D'Errico, 2009) being used to determine whether a sample was inside the convex hull of operationally relevant feature space. Within this grid, $\eta_{\sigma q}$ didn't asymptotically approach a constant value with decreasing parameter values for 28k samples. A second convex hull was constructed around the nearest neighbors of this subset of gridded samples. In Method 2, 1.3M random samples uniformly distributed in feature space where generated inside of this second convex hull. For Method 3, 380k samples were generated outside of the second hull, yet still inside of the operationally relevant feature space hull. Finally, in Method 4, 5.7M random samples uniformly distributed in feature space were generated inside the convex hull of operationally relevant feature space. The training set consisted of all the samples generated from Methods 1-3. The samples generated from Method 4 were separated such that the training set had 70% of the total samples with the validation and testing set having 15% each. The number of training,

validation, and testing samples for the charged particle models, as well as the extrema of each feature needed for the scaling in Eq. (21), is given in Table 4.1.

Table 4.1 Summary of the training, validation, and test samples for the classification and regression models for uncharged and charged particles

	N_{train} (-)	$N_{validate}$ (-)	N_{test} (-)	$[x_{m,min} \quad x_{m,max}]$ (-)				
				$\ln(\alpha)$	$\ln(N_R)$	$\ln(N_{Di})$	$\ln(N_{Im})$	$\ln(N_C)$
$\hat{y}_{\sigma 0,class}$	835,926	179,127	179,127	[-4.6052 -1.3863]	[-11.513 0.0000]	[-25.328 11.464]	–	–
$\hat{y}_{\sigma q,class}$	5,313,341	1,138,573	1,138,573	[-4.6052 -1.3863]	[-11.513 0.0000]	[-29.934 10.795]	[-23.920 4.3547]	[-15.397 4.5995]
$\hat{y}_{\sigma 0,regr}$	813,105	174,237	174,237	[-4.6052 -1.3863]	[-11.513 0.0000]	[-25.328 10.509]	–	–
$\hat{y}_{\sigma q,regr}$	5,147,558	1,103,048	1,103,048	[-4.6052 -1.3863]	[-11.513 0.0000]	[-29.934 10.770]	[-23.920 4.0231]	[-15.397 4.5995]

In the validation step, the feature weighting w_m used to calculate the weighted Euclidean distance in Eq. (22) and the number of nearest neighbors K were optimized to maximize the accuracy classification score of the classifier and the coefficient of determination of the regressor. The accuracy classification score and the coefficient of determination of the final classifier and regressor model fits, respectively, were then determined from the test dataset.

The final surrogate models to estimate the deterministic single fiber efficiencies for uncharged particles, $\hat{\eta}_{\sigma 0}$, and charged particles, $\hat{\eta}_{\sigma q}$, are given in Eq. (25). First, if sieving occurs, the process is surface filtration and the single fiber efficiency is effectively infinite. Second, if the radial particle velocity $v_r^*(b^*, 0) \leq 0$ for $\theta_0 = \pi$, all particles are collected on the surface of the filter and the single fiber efficiency is effectively infinite. Third, if the predicted classifier target is zero, the classification model predicts all particles are collected on the surface of the filter and the single fiber efficiency is effectively infinite. Lastly, if the predicted classifier target is unity, the classification model predicts that depth filtration

theory is valid and deterministic single fiber efficiency is calculated from the predicted regression target.

$$\hat{\eta}_{\sigma 0_i} = \begin{cases} \infty, & \text{if } 1 + N_{R_i} \geq \dfrac{1}{\sqrt{\alpha_i}} \\ \infty, & \text{if } 1 - \alpha_i^{5/2} N_{Di_i} \leq 0 \\ \infty, & \text{if } \hat{y}_{\sigma 0,class_i} = 0 \\ \left[\dfrac{1}{\sqrt{\alpha_i}} \sin\left(\dfrac{\pi}{e^{\hat{y}_{\sigma 0,regr_i}} + 1}\right)\right. & \\ \left. + \alpha_i{}^2 N_{Di_i}\left(\pi - \dfrac{\pi}{e^{\hat{y}_{\sigma 0,regr_i}} + 1}\right)\right], & \text{if } \hat{y}_{\sigma 0,class_i} = 1 \end{cases} \tag{25a}$$

$$\hat{\eta}_{\sigma q_i} = \begin{cases} \infty, & \text{if } 1 + N_{R_i} \geq \dfrac{1}{\sqrt{\alpha_i}} \\ \infty, & \text{if } \left[1 - \alpha_i^{5/2} N_{Di_i} - \dfrac{\alpha_i}{\left(1 - \sqrt{\alpha_i}\right)^2} N_{Im_i}\right. \\ & \left. - \alpha_i N_{C_i}\right] \leq 0 \\ \infty, & \text{if } \hat{y}_{\sigma q,class_i} = 0 \\ e^{\hat{y}_{\sigma q,regr_i}}, & \text{if } \hat{y}_{\sigma q,class_i} = 1 \end{cases} \tag{25b}$$

4.2.3 Experimental Validation of Surrogate Models

4.2.3.1 Filter Media

The initial filtration efficiency of three electrostatically-charged melt-spun type electret filter media used in commercial and residential HVAC filters were tested for the validation of the surrogate models developed in Section 4.2.2. The properties of these three electret media, labeled Media C, E, and F, are listed in Table 4.2. Media C, E, and F were assumed to be made of polypropylene. Note that the manufacturer identified Media C has having a medium charge level and Media E and F as having a high charge level. The

pressure drop equivalent fiber diameter $d_{f,R}$ from Rubow (1981), defined in Eq. (7), was determined to calculate η_D in Eq. (6). For Media C, E, and F the variable d_f was defined as the fitted geometric mean fiber diameter. This value was found by conditioning the media with isopropanol vapor for at least 24h to discharge the media (International Organization for Standardization, 2016), coating the discharged media with 5 nm of iridium, observing it with scanning electron microscope, and manually measuring the fiber diameters from the micrographs using ImageJ (ImageJ 1.48v, National Institutes of Health, USA). Outlying fiber diameters were declared using an adjusted boxplot for skewed distributions (Hubert and Vandervieren, 2008). Then a lognormal probability distribution was fitted to the trimmed fiber diameter data (Podgorski et al., 2011). Statistics of the observed fiber diameters are given in Table 4.2.

The surface charge densities of Media C, E, and F were unknown. Because of this, it was necessary to compare the surrogate model to the initial particle removal efficiencies of electret media with a known surface charge density. Li et al. (2012) tested two polypropylene electret filters, listed as Media 1 and 2 in Table 4.2. The filtration performance of these media was determined by measuring the penetration of charge neutralized polydisperse sodium chloride particles using a scanning mobility particle sizer at two face velocities, 5.3 and 10.6 cm/s. The surface charge density σ was estimated using the ionizing X-ray bipolar fiber charge method of Brown (1979) with the cavity correction described in Waker and Brown (1988). Media 1, having a higher charge level, had an estimated $\sigma = 118$ μC/m^2 and Media 2 had a lower charge level with an estimated $\sigma = 25$ μC/m^2. Li et al. (2012) states that the microscopic median fiber diameter was one-half of the effective fiber diameter calculated using the method of Davies (1953) in Eq. (26).

For Media 1 and 2, the variable d_f was defined as the value of the microscopic median fiber diameter estimated in this manner.

$$\Delta p = \frac{\mu_g U_0 h}{d_{f,D}^2}[64\alpha^{1.5}(1 + 56\alpha^3)] \tag{26}$$

Table 4.2 Summary of the filter properties of the electret media used for the experimental validation of single fiber efficiency surrogate models

	Filter Media				
	C	**E**	**F**	**1**[a]	**2**[a]
Thickness, h (mm)	0.698	0.826	1.18	0.69	0.77
Basis weight (g/m^2)	66.5	76.7	116	57.7	56.3
Pressure drop, Δp, at face velocity U_0 = 14 cm/s (mm H_2O)	1.56	1.95	2.53	n/a	n/a
Pressure drop, Δp, at face velocity U_0 = 5.4 cm/s (mm H_2O)	n/a	n/a	n/a	2.1	2.1
Solidity, α (-)	0.105	0.102	0.108	0.089	0.078
Charge level	Medium	High	High	High	Low
Surface charge density, σ (µC/ m^2)	n/a	n/a	n/a	118	25
Coefficient of determination of surrogate model for measured σ (-)	n/a	n/a	n/a	-0.0989	0.957
Effective surface charge density, σ_e (µC/ m^2)	55.7	125	123	65.4	24.4
Coefficient of determination of surrogate model for fitted σ_e (-)	0.821	0.907	0.912	0.975	0.962
Effective fiber diameter, $d_{f,R}$ (µm) (Rubow, 1981)	16.5	15.6	17.4	7.38	6.92
Effective fiber diameter, $d_{f,D}$ (µm) (Davies, 1953)	16.4	15.6	17.2	7.55	7.18
Number of fibers observed (-)	113	125	91	n/a	n/a
Arithmetic mean fiber diameter (µm)	14.3	13.4	14.5	n/a	n/a
Median fiber diameter (µm)	14.2	13.4	14.4	3.78	3.59
Minimal fiber diameter (µm)	11.7	10.5	12.9	n/a	n/a
Maximal fiber diameter (µm)	18.0	16.3	16.5	n/a	n/a
Fitted geometric mean fiber diameter (µm)	14.3	13.4	14.5	n/a	n/a
Fitted geometric standard deviation of fiber diameter (-)	1.06	1.06	1.06	n/a	n/a
Coefficient of determination of fitted lognormal fiber diameter distribution (-)	0.996	0.993	0.996	n/a	n/a

[a]Li et al. (2012)

4.2.3.2 Particle Filtration Testing

Three challenge particles in different size ranges were used for the measurement of aerosol penetration through Media C, E, and F. A schematic of the system used for this test is shown in Fig. 4.2. Silver nanoparticles generated by evaporation and condensation by passing a nitrogen carrier gas over a silver rod placed in an electric tube furnace (Lindberg/Blue M, Thermo Fisher Scientific, USA) classified into mobility diameters 3-50 nm by a Nano-Differential Mobility Analyzer (Nano-DMA) (Model 3085, TSI Inc., USA). For more details on the tube furnace temperature and carrier gas flow rate see Chang et al. (2015). Potassium chloride particles and polystyrene latex (PSL) spheres (3700A and 4009A, Thermo Fisher Scientific, USA) were aerosolized by a Collison type atomizer (Model 3079, TSI Inc., USA) and classified by mobility diameter using a long DMA (Model 3081, TSI Inc., USA) with KCl particles ranging 20-500 nm and PSL being 707 or 994 nm. For more details on the solution concentration of KCl see Chen et al. (2016).

Monodisperse test aerosols exiting the DMAs were charge conditioned in one of three ways before challenging filters. In the first method, singly charged particles challenged the filter directly after leaving the DMA. Otherwise, the particles passed through a Po-210 aerosol neutralizer which brings the aerosol into bipolar steady-state charge distribution. In the second method, these charge neutralized particles challenged the filter. In the third method, the charge neutralized particles passed through an electrostatic precipitator (ESP) which removed all charged particles. The remaining uncharged particles were then used to challenge the filter.

Test filters were housed in the filter holder described in Chang et al. (2015) which provides uniform particle deposition at face velocities up to 1.0 m/s. To calculate particle penetration through the test filter media, particle concentrations were measured upstream and downstream of the filter by an Ultrafine Condensation Particle Counter (UCPC) (Model 3776, TSI Inc., USA). Penetration was measured at three face velocities: 5, 25, and 50 cm/s. Media C, E, and F were tested as is (i.e., charged media). Media E was also tested after being discharged by isopropyl immersion as specified in International Organization for Standardization (2009). The combinations of filter media type and filter media charge conditioning, test particle type and particle charge conditioning, and test face velocity that were considered are summarized in Table 4.3.

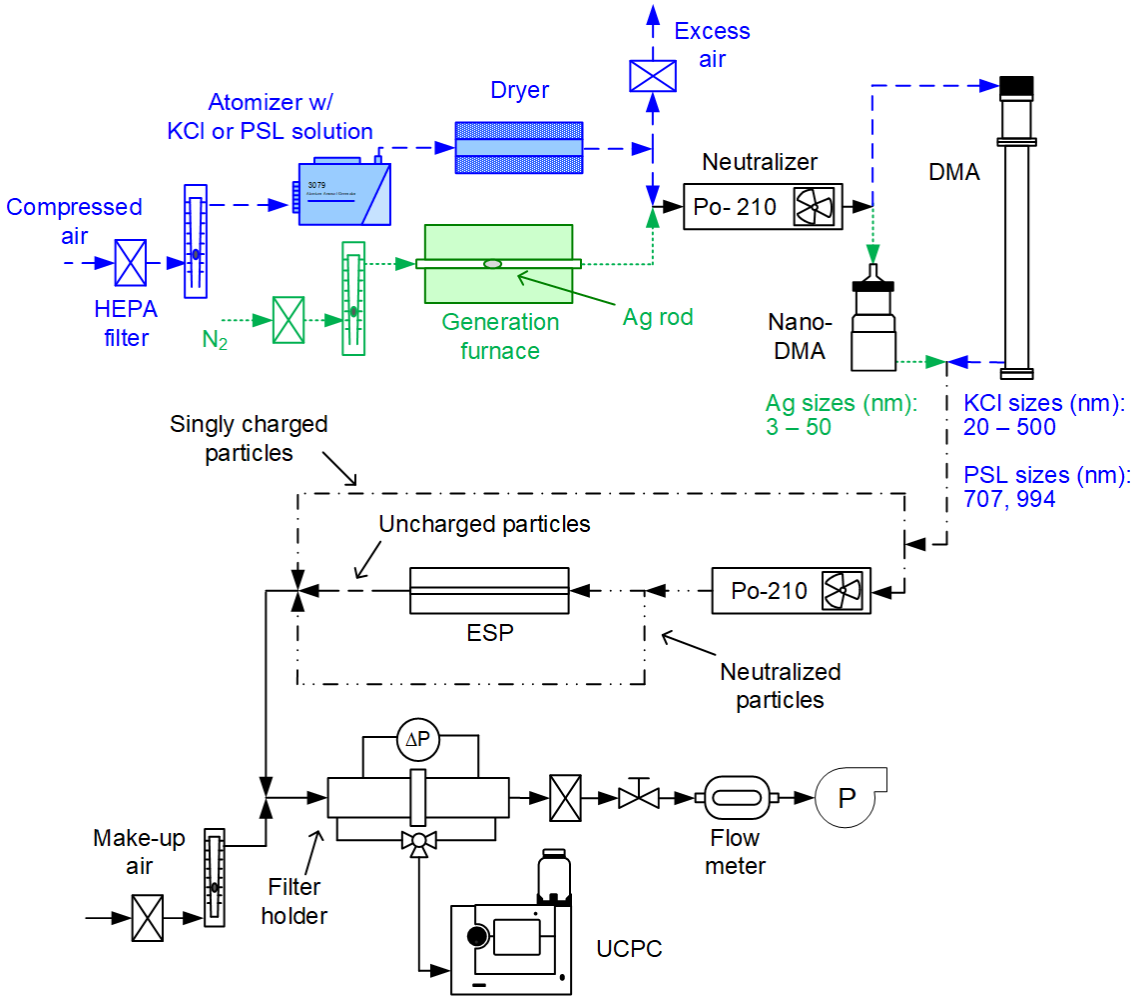

Fig. 4.2 Schematic of the experimental system to test the filtration efficiency of electret filter media

Table 4.3 Summary of the filter media, filter media charge conditioning, particle charge conditioning, particle material, and face velocity (in cm/s) test conditions used in the experimental validation of surrogate models

	Filter media charge conditioning	Particle charge conditioning						
		Uncharged particles			Singly charged particles		Neutralized particles	
		Ag	KCl	PSL	Ag	KCl	Ag	KCl
C	Charged	–	5	–	–	5, 25, 50	5, 25, 50	5, 25, 50
E	Charged	5, 25, 50	5, 25, 50	5, 25, 50	–	5, 25, 50	5, 25, 50	5, 25, 50
	Discharged	5, 25, 50	5, 25, 50	–	5, 25, 50	5, 25, 50	–	–
F	Charged	–	5	–	–	5, 25, 50	5, 25, 50	5, 25, 50

4.2.3.3 Fitting of an Effective Surface Charge Density

An effective charge density σ_e was calculated for each electret filter media by using the method of least squares to minimize the sum of the squares of the residuals, the difference between the measured and predicted aerosol penetration, for all experiential conditions. The sum of the squares of the residual was minimized using the differential evolution algorithm (Storn and Price, 1997) in the SciPy library (Jones et al., 2001-). Differential evolution is stochastic in nature and does not require that the function being optimized be differentiable. This is an attractive method since $\hat{\eta}_{\sigma 0}$ and $\hat{\eta}_{\sigma q}$ found using KNN are discontinuous and noisy.

To compare the surrogate models to experimental data, several assumptions were necessary regarding the input variables in the models. The assumptions pertaining to filter media properties were described in Section 4.2.3.1. The value of the particle diameter variable d_p was taken to be the particle mobility diameter. When particles were charge neutralized the penetration was calculated using Eq. (5b) where charge fraction of each particle $f(n)$ was calculated using the approximation of the bipolar charge distribution from Wiedensohler (1988). Gas properties were calculated for dry air at NTP. The assumed relative permittivities of all the relevant materials considered are summarized in Table 4.4.

Table 4.4 Summary of the relative permittivities of gas, particle, and fiber materials

Ag	Air[a]	KCl[b]	NaCl[b]	Polystyrene[b]	Polypropylene[c]
∞	1.00059	4.86	5.92	2.55	2.28

[a]Hector and Schultz (1936)
[b]Laboratory for Insulation Research Massachusetts Institute of Technology Cambridge (1953)
[c]Anderson and McCall (1958)

4.3 Results

4.3.1 Validation and Testing of KNN Models

The optimized values for K, the number of nearest neighbors, and w_m, the weight applied to feature m when computing the weighted Euclidean distance, found from the validation dataset are given in Table 4.5. A higher weight suggests that this feature carries more importance on the target value, while a lower weight suggests less importance. For instance, of the feature weights for the $\hat{y}_{\sigma 0,class}$ predicted target, the weight for the α feature is the smallest. This will shorten the length along the α feature when computing distances to nearest neighbors. On the other hand, weight for the N_{Di} feature is the largest. This signals that $y_{\sigma 0,class}$ varies the most along the N_{Di} feature. By applying a larger scale to the N_{Di} feature, the prediction target $\hat{y}_{\sigma 0,class}$ is less likely to incorporate this variance. It can be seen that N_{Di} has the most influence on deciding whether depth filtration theory is valid in the classifier. This makes sense since dielectrophoretic forces are long range attractive forces which will extend the upper and lower limiting trajectories further apart. N_{Di} also has the most influence in predicting single fiber efficiency and α the least. The classification accuracy scores of the final classifier models for uncharged and charged particle were 99.9% and 99.7%, respectively. The coefficients of determination for the final regressor models for uncharged and charged particles were 1.00 and 0.999, respectively.

Table 4.5 Summary of the optimized hyperparameters K, the number of nearest neighbors, and w_m, the weight applied to feature m, for the classification and regression targets for uncharged and charged particles and their respective accuracy scores or coefficient of determination

Predicted target	K	w_m					Accuracy score (%)	R^2
		$\ln(\alpha)$	$\ln(N_R)$	$\ln(N_{Di})$	$\ln(N_{Im})_{Im}$	$\ln(N_C)$		
$\hat{y}_{\sigma 0,class}$	57	0.0711	0.404	0.525	–	–	99.9	–
$\hat{y}_{\sigma q,class}$	69	0.0192	0.000820	0.613	0.365	0.00215	99.7	–
$\hat{y}_{\sigma 0,regr}$	9	0.0214	0.278	0.7001	–	–	–	1.00
$\hat{y}_{\sigma q,regr}$	25	0.00897	0.170	0.345	0.257	0.219	–	0.999

In Fig. 4.3(a) a histogram of the relative error, defined by $|\eta - \hat{\eta}|/\eta$, of $\hat{\eta}_{\sigma 0}$ in the estimation of the $\eta_{\sigma 0}$ samples in the test data is shown. In general, the relative error is less than about 3% with the mean and median relative errors being 0.79% and 0.61%, respectively. The maximum relative error is 190%. Higher relative error was observed for extremely low values of $\eta_{\sigma 0}$. This was due to a numerical accuracy issue. For extremely low values of $\eta_{\sigma 0}$, the change in the estimated θ_b between iterations of the binary search method reached the limit of machine accuracy before the calculated $\eta_{\sigma 0}$ converged. As seen in Fig. 4.3(b), $\hat{\eta}_{\sigma q}$ did not have this problem since the maximum relative error was 55%. For $\hat{\eta}_{\sigma q}$ the mean and median relative errors were 5.5% and 4.2%, respectively. The prediction of $\hat{\eta}_{\sigma q}$ is coarser than $\hat{\eta}_{\sigma 0}$ because more samples are required as more features are considered. $\hat{\eta}_{\sigma 0}$ has 3 features while $\hat{\eta}_{\sigma q}$ has 5. In addition, the computation of $\eta_{\sigma q}$ samples required about 2,000 – 3,000 times more CPU time than that of $\eta_{\sigma 0}$ because of the need to numerically integrate over a distribution of fiber orientations for the $\eta_{\sigma q}$ model.

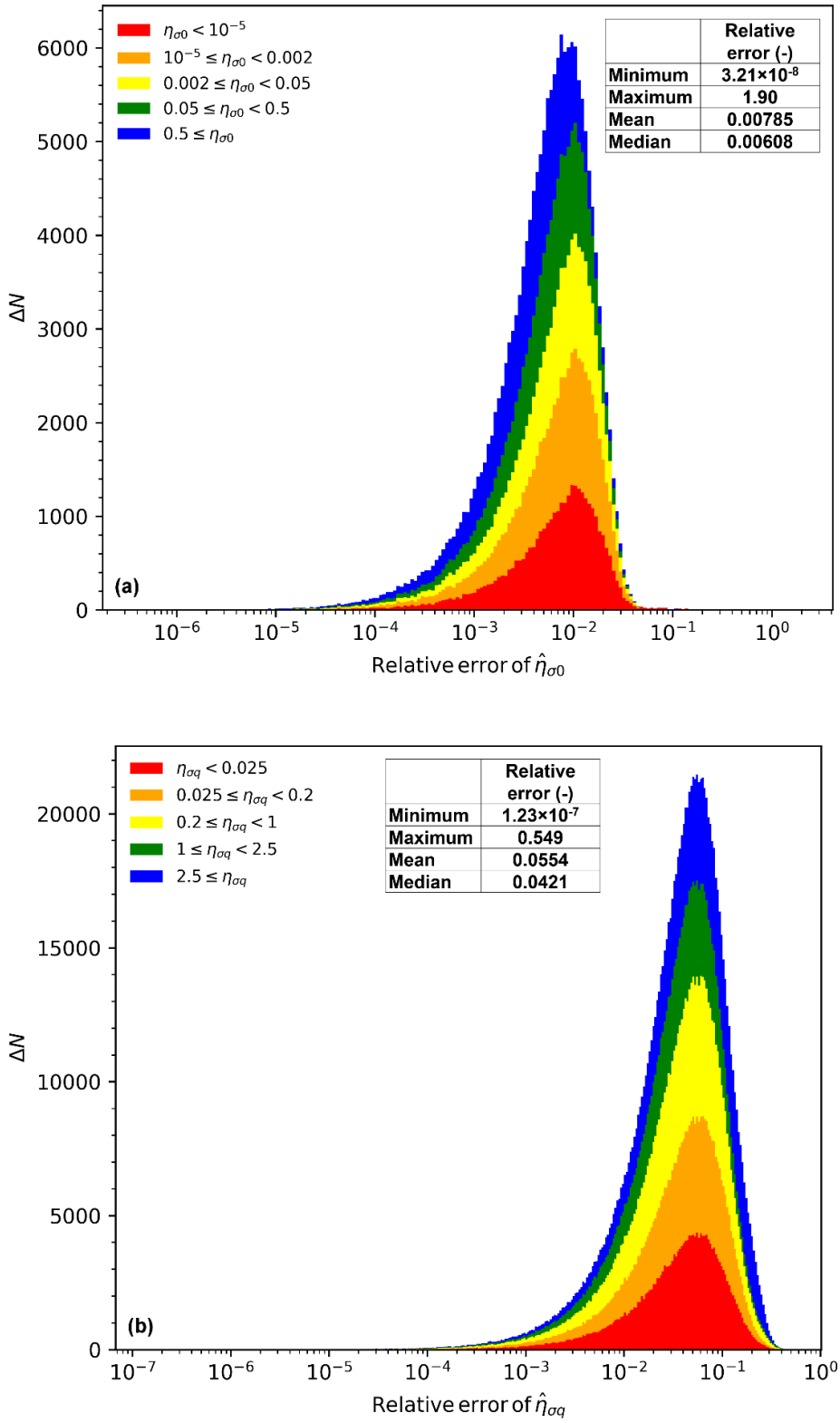

Fig. 4.3 Stacked histograms of the relative error of the predicted single fiber efficiencies for (a) uncharged particles and (b) charged particles where color denotes the known target single fiber efficiency

4.3.2 Characterization of Filter Media by Scanning Mobility Microscope

Fig. 4.4(a) shows the adjusted boxplots for skewed distributions of the fiber diameters of Media C, E, and F. At least 91 fibers were measured for each media. Outliers were excluded and then the trimmed data was fitted to a lognormal distribution as seen in Figs. 4.4(b – d). The statistics of the observed fibers are summarized in Table 4.2. The fiber diameters for each media were very monodisperse, with all media having a fitted geometric standard deviation of fiber diameter of 1.06. The fitted geometric mean fiber diameters for Media C, E, and F were 14.3, 13.4, and 14.6 μm, respectively. Media and mean fiber diameters were within 0.1 μm of the fitted geometric mean fiber diameters.

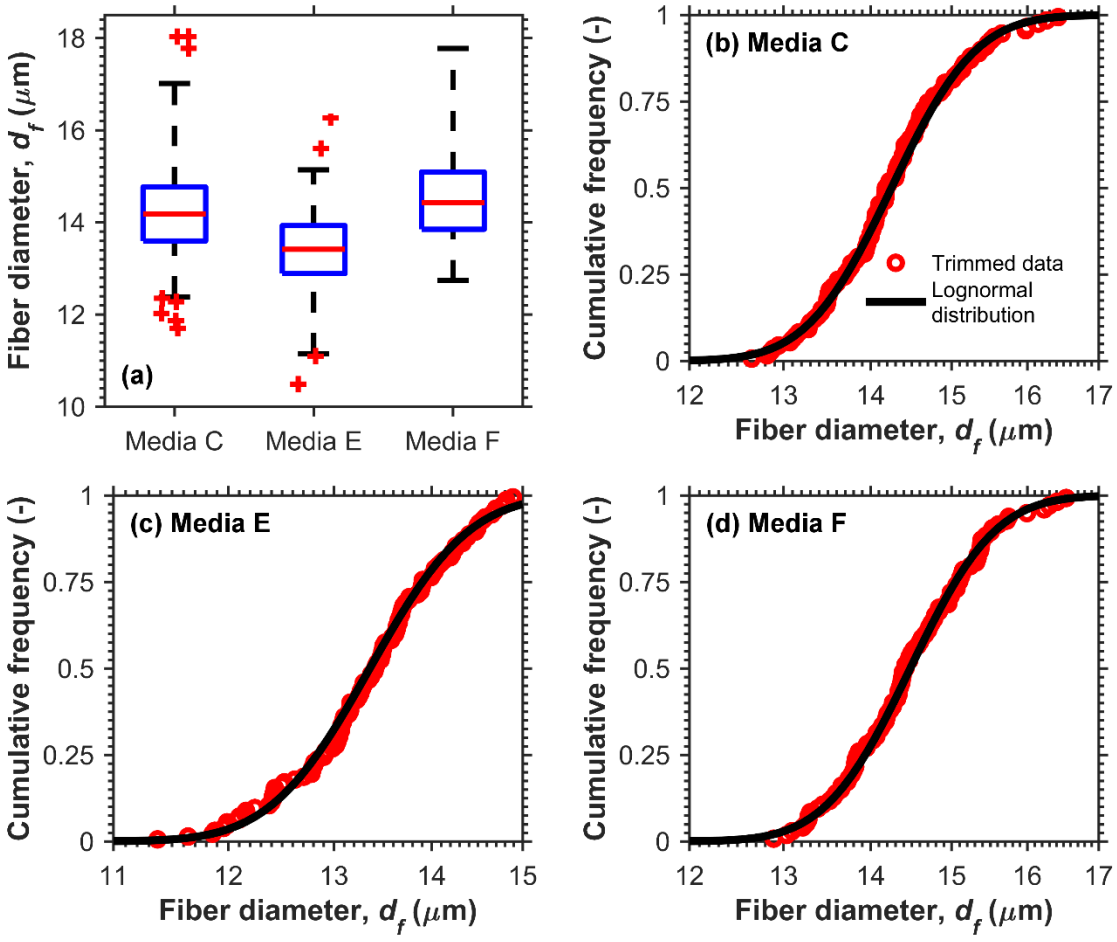

Fig. 4.4 (a) Adjusted boxplots for skewed distributions of the fiber diameters of Media C, E, and F and (b-d) cumulative probability distributions of the lognormal fiber distributions fitted to trimmed data for Media C, E, and F

4.3.3 Comparison of Surrogate Models to Experimental Data

4.3.3.1 Discharged Media

In Fig. 4.5 the ability of the surrogate models $\hat{\eta}_{\sigma 0}$ and $\hat{\eta}_{\sigma q}$ to predict aerosol collection by purely mechanical collection mechanisms was examined. The known values for α and N_R were input while an infinitesimal value was input for any parameter depended on particle charge or surface charge density, i.e., $\hat{\eta}_{\sigma 0}(\alpha, N_R, N_{Di} \rightarrow 0)$ and

$\hat{\eta}_{\sigma q}(\alpha, N_R, N_{Di} \to 0, N_{Im} \to 0, N_C \to 0)$. The surrogate models were then compared to the analytical equation for particle collection by direct interception for Kuwabara cell model η_R (Brown, 1993; Langmuir, 1942) and experimental data collected for discharged Media E challenged by uncharged particles. There was decent agreement between the model for η_D and data for particles smaller than about 30 nm. $\hat{\eta}_{\sigma 0}$ was equivalent to the analytical equation η_R while $\hat{\eta}_{\sigma q}$ overestimated η_R.

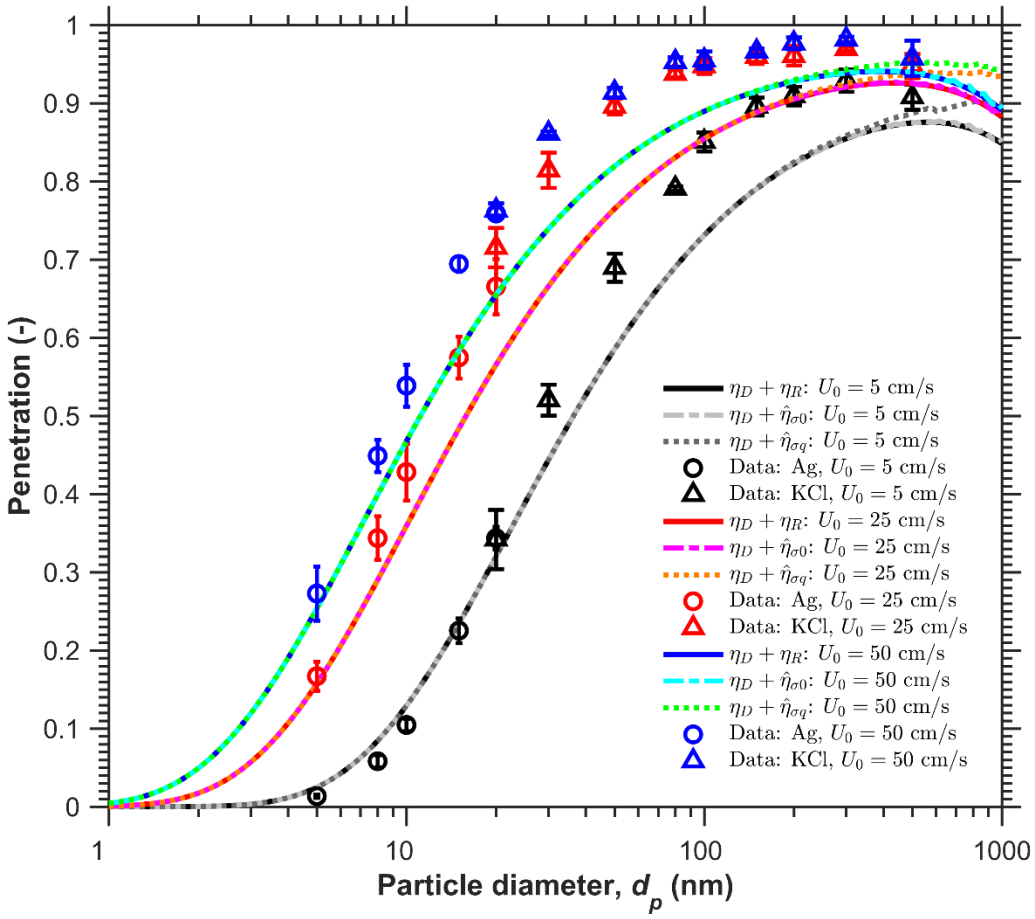

Fig. 4.5 Comparison of theoretical and experimental aerosol penetration for discharged Media E challenged by uncharged particles

In Fig. 4.6, the ability of $\hat{\eta}_{\sigma q}$ to predict aerosol collection when the image force is the only electrostatic force was examined. Again, the known values for α and N_R were input while an infinitesimal value was input for any parameter depended on surface charge density, i.e., $\hat{\eta}_{\sigma 0}(\alpha, N_R, N_{Di} \to 0, N_{Im}, N_C \to 0)$. The surrogate model was compared to experimental data collected for discharged Media E challenged by singly charged particles. The surrogate model could simulate the decrease in aerosol penetration, relative to the penetration of uncharged particles, when the discharged Media E was challenged by singly charged particles.

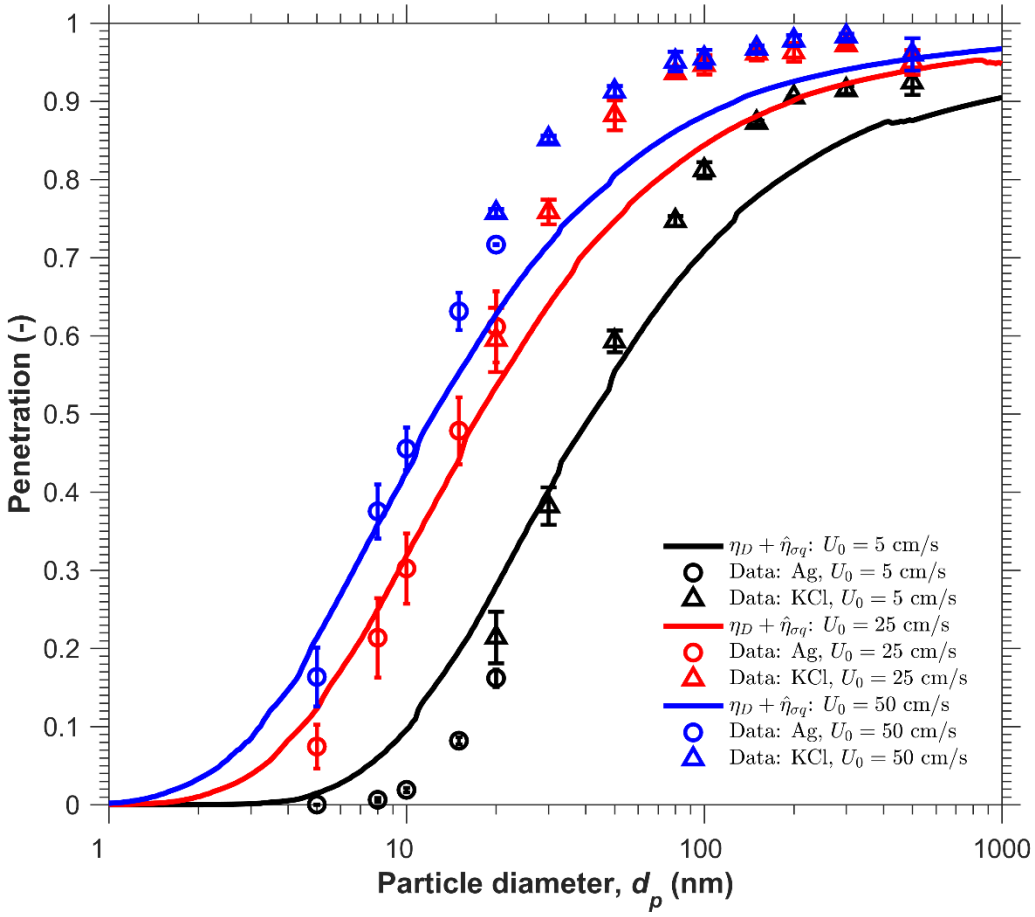

Fig. 4.6 Comparison of theoretical and experimental aerosol penetration for discharged Media E challenged by singly charged particles

4.3.3.1 Charged Media

Now the performance of the surrogate models in simulating the behavior of charged filter media will be considered. The comparison to the results of Li et al. (2012) will be discussed first, because this study estimated the surface charge density using the ionizing X-ray bipolar fiber charge method of Brown (1979) with cavity correction described in Waker and Brown (1988). Fig. 4.7(a) compares the penetration data for Media 1 with the surrogate model when the measured surface charge density of 118 $\mu C/m^2$ was input, plotted in the solid curve, and when the effective surface charge density of 65.4 $\mu C/m^2$ was input, plotted in the dashed curve. The measured surface charge density agreed very poorly with the data (R^2 = -0.099), while the fitted effective surface charge density was in excellent agreement with the data (R^2 = 0.98). This effective surface charge density was closer to the value of 70 $\mu C/m^2$ Chen et al. (2014) found for this media by fitting the theory of Lathrache and Fissan (1987). Fig. 4.7(b) shows the excellent agreement between the aerosol penetration data, surrogate model for the measured surface charge density (25 $\mu C/m^2$, R^2 = 0.96), and the surrogate model for the effective surface charge density (24.4 $\mu C/m^2$, R^2 = 0.96). The reason for the disagreement between the measured and effective charge densities for Media 1 and agreement for Media 2 is unknown. Potential sources of experimental error could be variation between the samples used in the charge measurement and filtration efficiency tests, difficulty in identifying the endpoint of charge neutralization by ions (Brown, 1993), or perhaps some filter material dependency in the cavity theory (Waker and Brown, 1988).

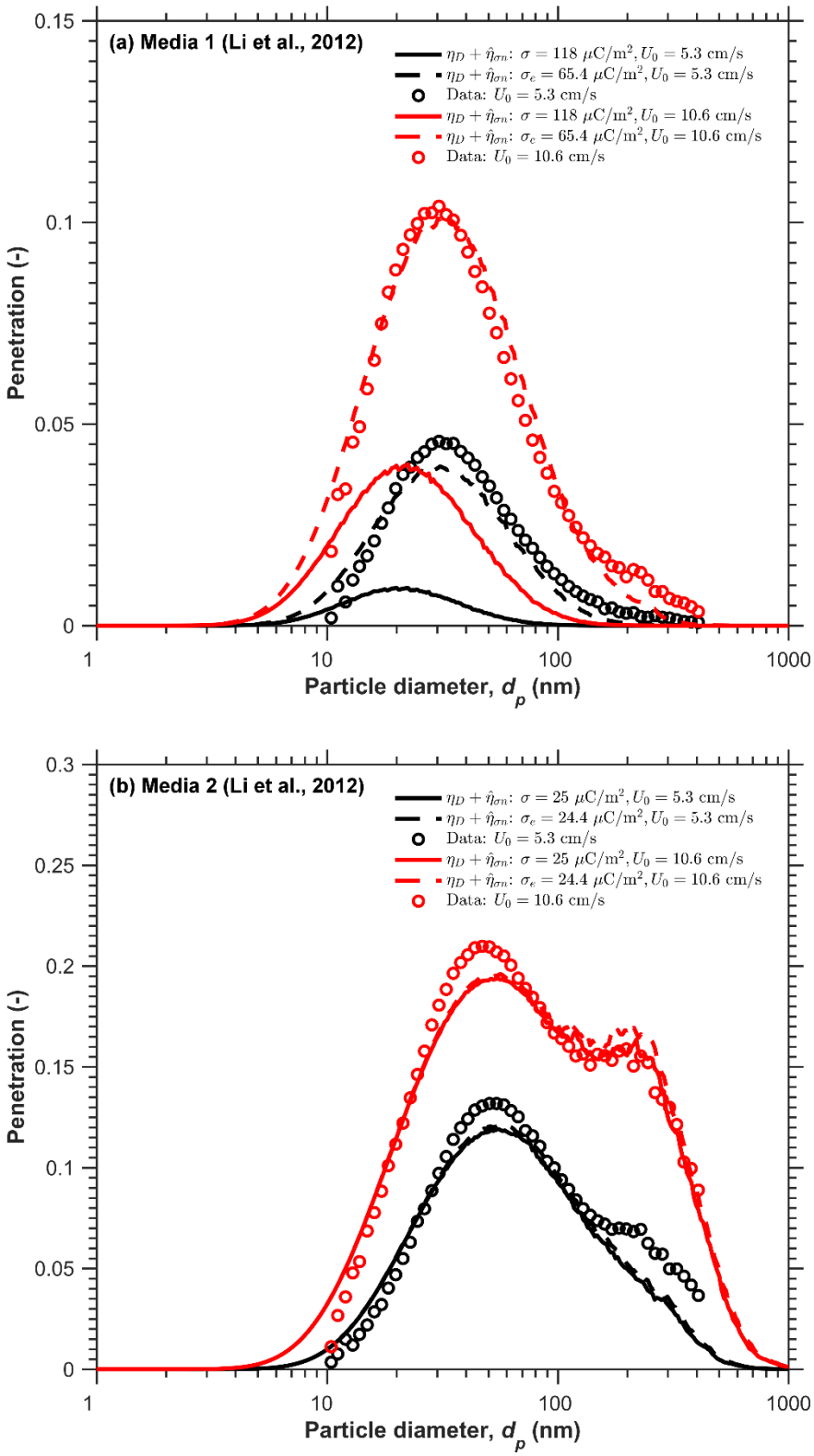

Fig. 4.7 Comparison of theoretical and experimental aerosol penetration for (a) Media 1 and (b) Media 2 challenged by charge neutralized NaCl particles

The surface charge densities of Media C, E, and F were unknown. Effective surface charge densities were found by fitting the surrogate models to penetration data collected for the experimental conditions listed in Table 4.3. The effective surface charge densities for Media C, E, and F were 55.7, 125, and 123 μC/m^2 and their respective coefficients of determination were 0.82, 0.91, and 0.91. Media C, E, and F were reported as having medium, high, and high levels of charge, respectively. These effective surface charge densities fall in line with the measured charge densities in Li et al. (2012) for a media with low level charge (Media 2 was 25 μC/m^2) and high level charge (Media 1 was 118 μC/m^2).

Next, the agreement between surrogate models and experimental data for Media E for $\sigma_e = 125\ \mu\text{C/m}^2$ will be explored for the various experimental conditions. Results were similar for Media C and F and are included in Appendix 2. In Fig. 4.8 the experimental results and surrogate models for Media E challenged by uncharged Ag, KCl, and PSL at three face velocities are plotted. The surrogate model predicted the relative changes in aerosol penetration due to particle relative permittivity. The general shapes of the model curves match the data, with good agreement for KCl particles larger than 80 nm where the decrease of aerosol penetration was due to dielectrophoresis. The model was unable to accurately predict the most penetrating particle size (MPPS). The experimental data shows an MPPS of 30 nm for all face velocities. The corresponding model curves for this size would be the dashed curves for KCl particles which predicted an MPPS of 40 – 60 nm with an increasing MPPS with increasing face velocity. The MPPS occurs where the sum of η_D and $\hat{\eta}_{\sigma 0}$ is at its minimum. The disagreement may arise from the inaccuracies of η_D for particles larger than 30 nm which were already demonstrated in Fig. 4.5.

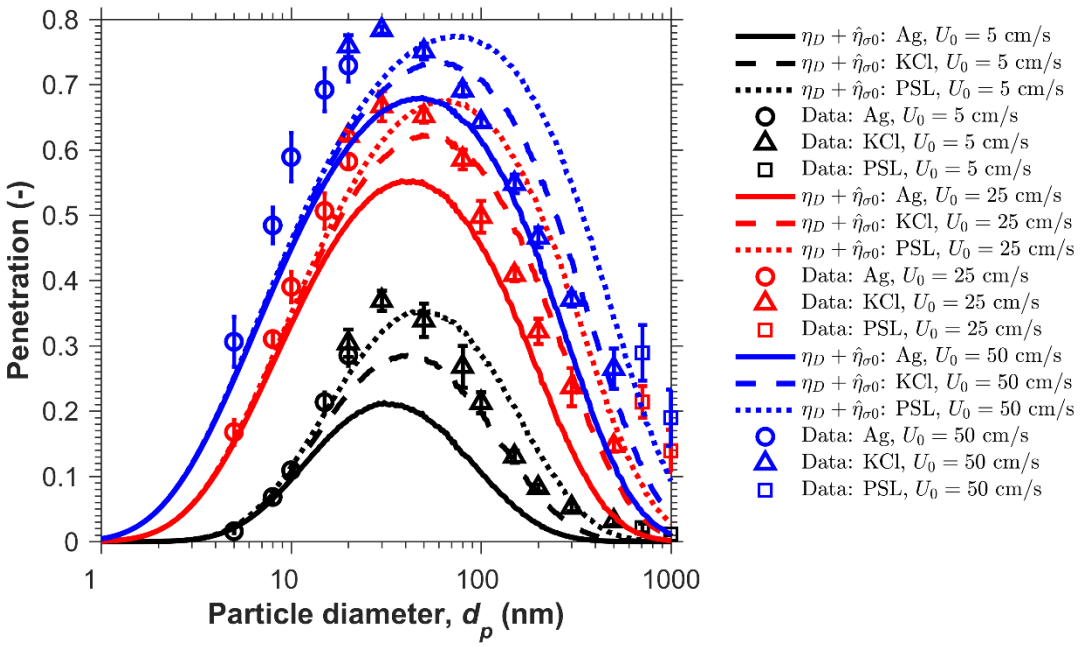

Fig. 4.8 Comparison of theoretical and experimental aerosol penetration for Media E challenged by uncharged particles

Fig. 4.9 compares the experimentally measured penetration of singly charged KCl particle with that predicted by the surrogate model. The model simulates that Media E removes almost all singly charged particles smaller than 50 nm. The agreement between model and data is good for face velocities of 25 and 50 cm/s, but the model underestimates the data at 5 cm/s. The model for $\hat{\eta}_{\sigma q}$ in Fig 4.9 is noisier than the model for $\hat{\eta}_{\sigma 0}$ in Fig 4.8. This is because the number of features in the model increased from 3 to 5 and the training sample size for $\hat{\eta}_{\sigma q}$ wasn't large enough to provide as smooth of curves as $\hat{\eta}_{\sigma 0}$.

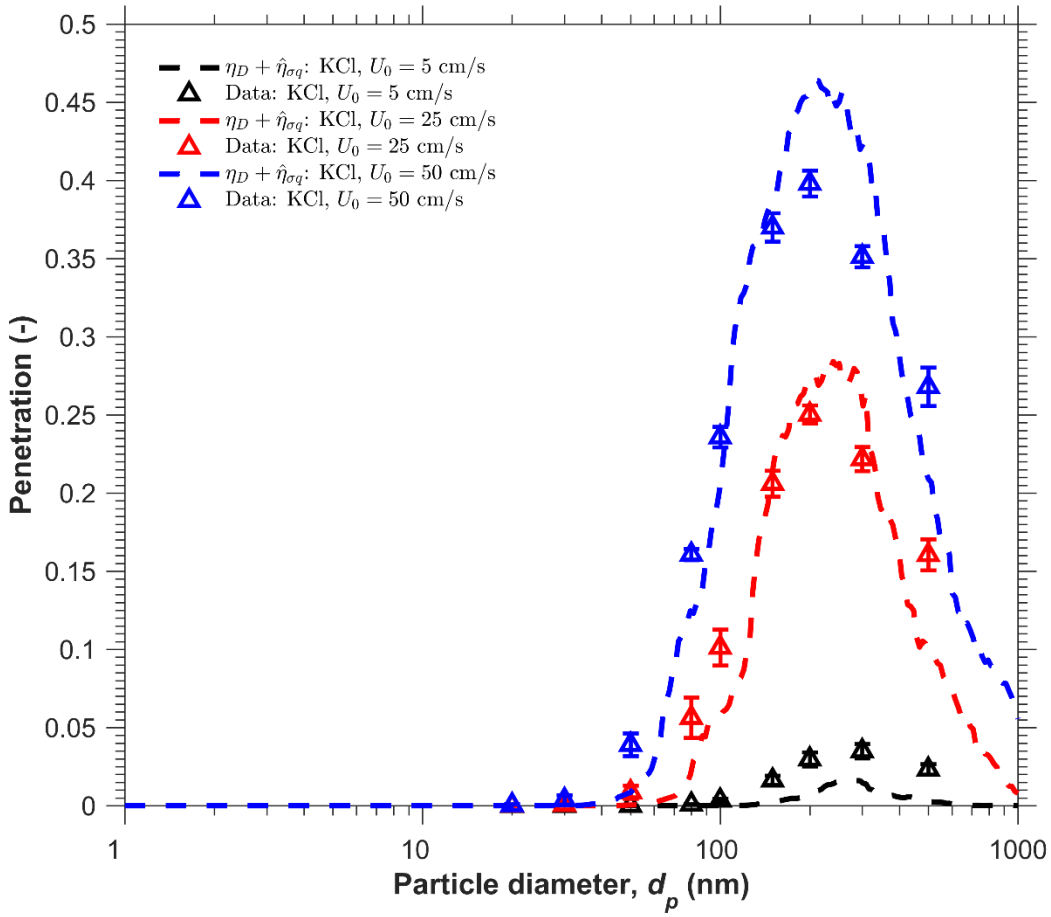

Fig. 4.9 Comparison of theoretical and experimental aerosol penetration for Media E challenged by singly charged KCl particles

Finally, in Fig. 4.10 the penetration of charge neutralized Ag and KCl is presented. The surrogate model predicted the bimodal nature of the experimental data at face velocities of 25 and 50 cm/s. This bimodal shape reflects the fact that the penetration of particles is the sum of the aerosol penetration of particles carrying n charges weighted by the fraction of the total upstream particles carrying n charges, $f(n)$, as seen in Eq. (5b). Most particles smaller than 10 nm carry no charge (Wiedensohler, 1988) and dielectrophoresis has negligible effect on particle collection at these small sizes. The tail at the small sizes of penetration curve is due to collection by diffusion. As particle diameter

increases to about 70 nm, the fraction of particles carrying some charge increases to about 50% and all particles carrying a charge are collected with nearly 100% efficiency by Coulomb force. The efficiency of particle collection due to Coulomb force decreases with increasing particle size until all charge fractions behave identically to the uncharged fraction and are collected primarily by dielectrophoresis. While the model located the two local MPPSs, the magnitude of the aerosol penetration was underestimated for the peak at smaller sizes and overestimated for the peak at larger sizes.

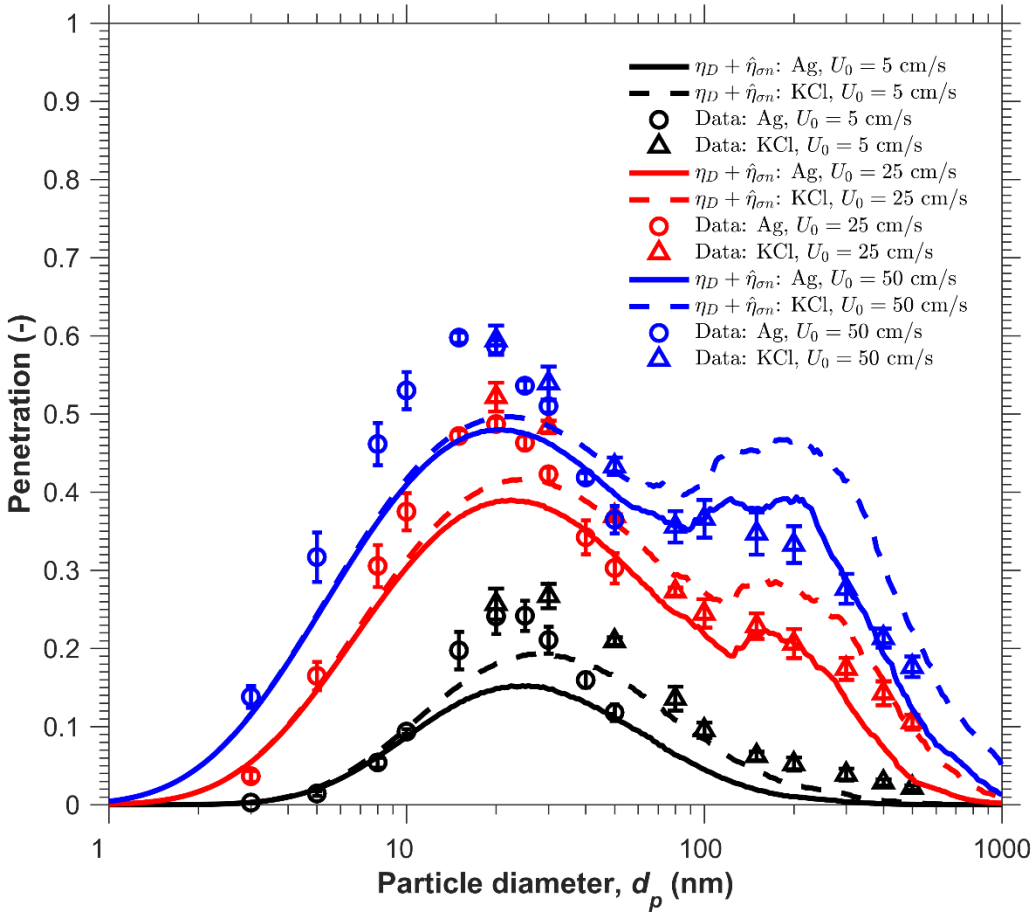

Fig. 4.10 Comparison of theoretical and experimental aerosol penetration for Media E challenged by charge neutralized particles

4.4 Discussion

In this section, four assumptions in the underlying theoretical model and their potential influence on the performance of the surrogate model will be discussed. These assumptions are: (1) additivity between stochastic and deterministic collection mechanisms, (2) the omission of particle inertia, (3) omission of fluid inertia, and (4) uniform particle concentration on the inlet boundary of the flow cell.

4.4.1 Assumption of Additivity Between Stochastic and Deterministic Collection Mechanisms

In the current model, single fiber efficiency is defined as the sum of the stochastic collection mechanisms, η_D, and deterministic collection mechanisms, η_{det}, which includes the effects of particle drag, interception, and electrostatic forces. In Fig. 4.11 the single fiber efficiencies for η_D as given in Eq. (6), direct interception for Kuwabara cell model η_R (Brown, 1993; Langmuir, 1942), an approximation of dielectrophoretic collection efficiency for a point mass, η_{Di}, found by taking the asymptotic limit of $\hat{\eta}_{\sigma 0}$ as N_R approaches zero, i.e., $\hat{\eta}_{\sigma 0}(\alpha, N_R \to 0, N_{Di})$, the sum of these previous three efficiencies, $\hat{\eta}_{\sigma 0}$, $\eta_D + \hat{\eta}_{\sigma 0}$, and experimentally measured single fiber efficiencies for Media E challenged by uncharged KCl particles at face velocity of 5 cm/s are plotted as a function of particle diameter. Analytical curves are plotted as dotted lines, the asymptotic single fiber efficiency from the surrogate model is plotted as a dashed line, the surrogate model is plotted as a dash-dot line, summed single fiber efficiencies are solid lines, and experimental results are symbols.

For the case plotted, interception has no effect on the single fiber efficiency as $\hat{\eta}_{\sigma 0}(\alpha, N_R \to 0, N_{Di}) \approx \hat{\eta}_{\sigma 0}$. This is not to suggest that this is a universal result. For instance, assuming the additivity of $\eta_D + \eta_R + \hat{\eta}_{\sigma 0}(\alpha, N_R \to 0, N_{Di})$ for Media 2, which has a smaller fiber diameter and lower charge level, will result in an overestimation of single fiber efficiency. One can also see in Fig. 4.11 that $\eta_D + \hat{\eta}_{\sigma 0}$ overestimates the experimentally measured single fiber efficiency in the particle size range of 20 – 100 nm. Using Brownian dynamics Podgórski and Bałazy (2008) found that for cylindrical electret fibers with line dipole charge having linear charge densities Q between 0.1 nC/m and 13 nC/m, single fiber efficiencies of uncharged particles found by $\eta_D + \eta_{det}$ will overestimate the true single fiber efficiency for particles smaller than some critical value due to the coupling of diffusion and dielectrophoresis. After relating linear charge density to surface charge density by $Q = \sigma d_f$ (Brown, 1993) and consulting Fig. 4 in Podgórski and Bałazy (2008), it was found that for Media E with the experimental conditions considered in Fig 4.11, $\eta_D + \eta_{det}$ would overestimate the true single fiber efficiency for particles smaller than about 80 – 140 nm. This coupling of diffusion and dielectrophoresis could help explain why the measured aerosol penetration exceeded the predicted penetration near the MPPS in Figs. 4.8 and 4.10. For particles larger than 300 nm, $\hat{\eta}_{\sigma 0}$ begins to overestimate the measured single fiber efficiency. The may be a result of there being a limiting single fiber efficiency which exists because of the interaction of neighboring fiber (Lee et al., 2002).

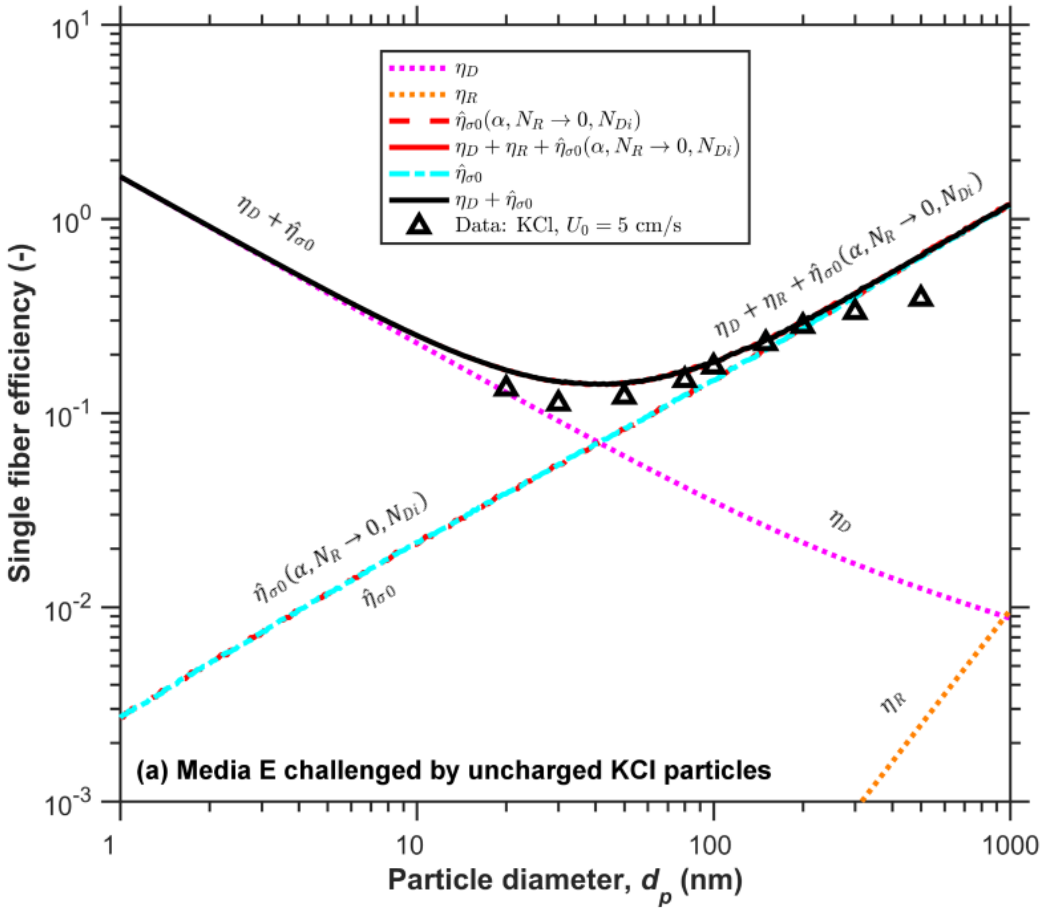

Fig. 4.11 Comparison of theoretical and experimental single fiber efficiencies for Media E challenged by uncharged KCl particles at a face velocity of 5 cm/s

In Fig. 4.12 the single fiber efficiencies for η_D, η_R, approximations of electrostatic force collection efficiencies for a point mass found by taking the asymptotic limit of the surrogate model as all nondimensional parameters except α and the given force's corresponding nondimensional parameter approach zero, i.e., $\hat{\eta}_{\sigma 0}(\alpha, N_R \to 0, N_{Di})$, $\hat{\eta}_{\sigma q}(\alpha, N_R \to 0, N_{Di} \to 0, N_{Im}, N_C \to 0)$, and $\hat{\eta}_{\sigma q}(\alpha, N_R \to 0, N_{Di} \to 0, N_{Im} \to 0, N_C)$, the sum of these previous five efficiencies, $\hat{\eta}_{\sigma q}$, $\eta_D + \hat{\eta}_{\sigma q}$, and the experimentally measured single fiber efficiencies for Media E challenged by singly charged KCl particles at a face velocity of 5 cm/s are plotted as a function of particle diameter. Analytical curves are

plotted as dotted lines, the asymptotic single fiber efficiencies from surrogate models are plotted as dashed lines, the surrogate model is plotted as a dash-dot line, summed single fiber efficiencies are solid lines, and experimental results are symbols.

In Fig. 4.12 it is evident that Coulomb and dielectrophoretic collection mechanisms were dominant for these conditions. The sum of all single fiber efficiencies of independent collection mechanisms gives worse agreement with experimental data than $\eta_D + \hat{\eta}_{\sigma q}$ near the MPPS. This agrees with the finding from Emi et al. (1987), Kanaoka et al. (1987), and Lee et al. (2002) that there is a negative interaction between dielectrophoretic and Coulomb forces which disallows the use of a simple superposition of efficiencies calculated for each force independently. The disagreement between experimental data and $\eta_D + \hat{\eta}_{\sigma q}$ increases as particle size decreases. The experimental data begins to plateau for particles smaller than 50 nm. The modeled curve ends near the same size because $\hat{\eta}_{\sigma q}$ equals infinity due to the fulfillment of condition two or three in in Eq. (25b). While both the data and model approached a limiting value near the same particle size, there was a large disagreement in the magnitude of the single fiber efficiency. This disagreement may be caused by the interaction of neighboring fibers, such as the overlap of electric fields from individual fibers (Lee et al., 2002).

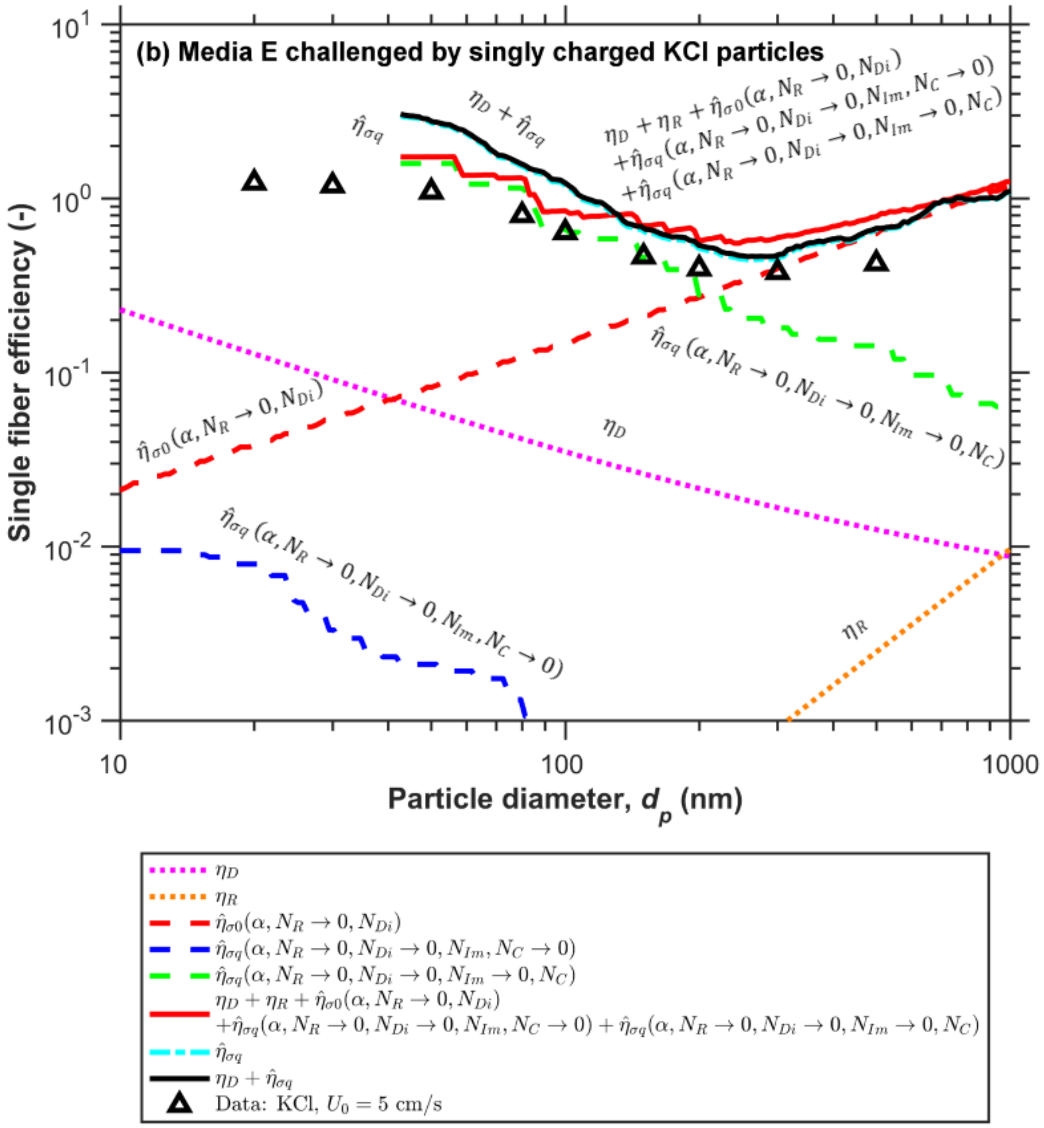

Fig. 4.12 Comparison of theoretical and experimental single fiber efficiencies for Media E challenged by singly charged KCl particles at a face velocity of 5 cm/s

By solving the convection-diffusion equation including Coulomb force, Lee et al. (2002) calculated the regions were the particle collection was either diffusion dominant, where $N_C < 2.7Pe^{0.043 \ln Pe - 1.16}$, or Coulomb force dominant, where $N_C >$

$340Pe^{0.076 \ln Pe - 1.56}$, for the most advantageous orientation of a cylindrical electret fiber with line dipole charge distribution (i.e., $\theta_0 = 0$ for a positively charged particle). In between these two regions, a negative interaction exists between η_D and the Coulomb force single fiber efficiency which precludes the use of the additivity assumption. Using this estimate, the dominant collection regions were found for Media E challenged by singly charged particles at face velocities of 5, 25, and 50 cm/s. Particle collection is Coulomb force dominated for particles smaller than 740, 220, and 140 nm, respectively. This is larger than the observed MPPSs in Fig. 4.9 for all face velocities, except 50 cm/s, suggesting that the additivity assumption of $\eta_D + \hat{\eta}_{\sigma q}$ was reasonable for the experimental conditions investigated.

4.4.2 Omission of Particle Inertia

To evaluate the validity to exclude particle inertia in the deterministic single fiber efficiency, the study of Cao et al. (2004) can be considered. Cao et al. (2004) used Brownian dynamics to consider the effect of particle inertia on the collection of uncharged particles in a staggered array of parallel, rectangular split-type electret fibers. It was found that for particle Stokes numbers greater than 0.5, inertial impaction and interception were the major collection mechanisms. Particle Stokes number never reached 0.5 for all the experimental conditions that Media C, E, F, 1, and 2 were investigated under. This suggests that the decision to neglect particle inertia was acceptable.

4.4.3 Omission of Fluid Inertia

When $Re_f \ll 1$ the effects of viscous forces are dominant and fluid inertia can be ignored. For $Re_f \gg 1$ viscous effects are negligible. For the experimental conditions considered, Re_f was in the range of 0.013 – 0.52 which places much of the data in the viscous-inertial transition flow regime where theories assuming viscous flows are questionable (Hubbard et al., 2012; Sanchez et al., 2013). If σ_e were fitted from the data for all particle charge conditions at each Re_f (which vary as a function of test face velocity), instead of the pooled data for all experimental conditions, a clear trend is observed. In Fig. 4.13(a) it seen that σ_e will increase with increasing Re_f, while Fig. 4.13(b) shows that the goodness of the fit for σ_e will decrease with increasing Re_f.

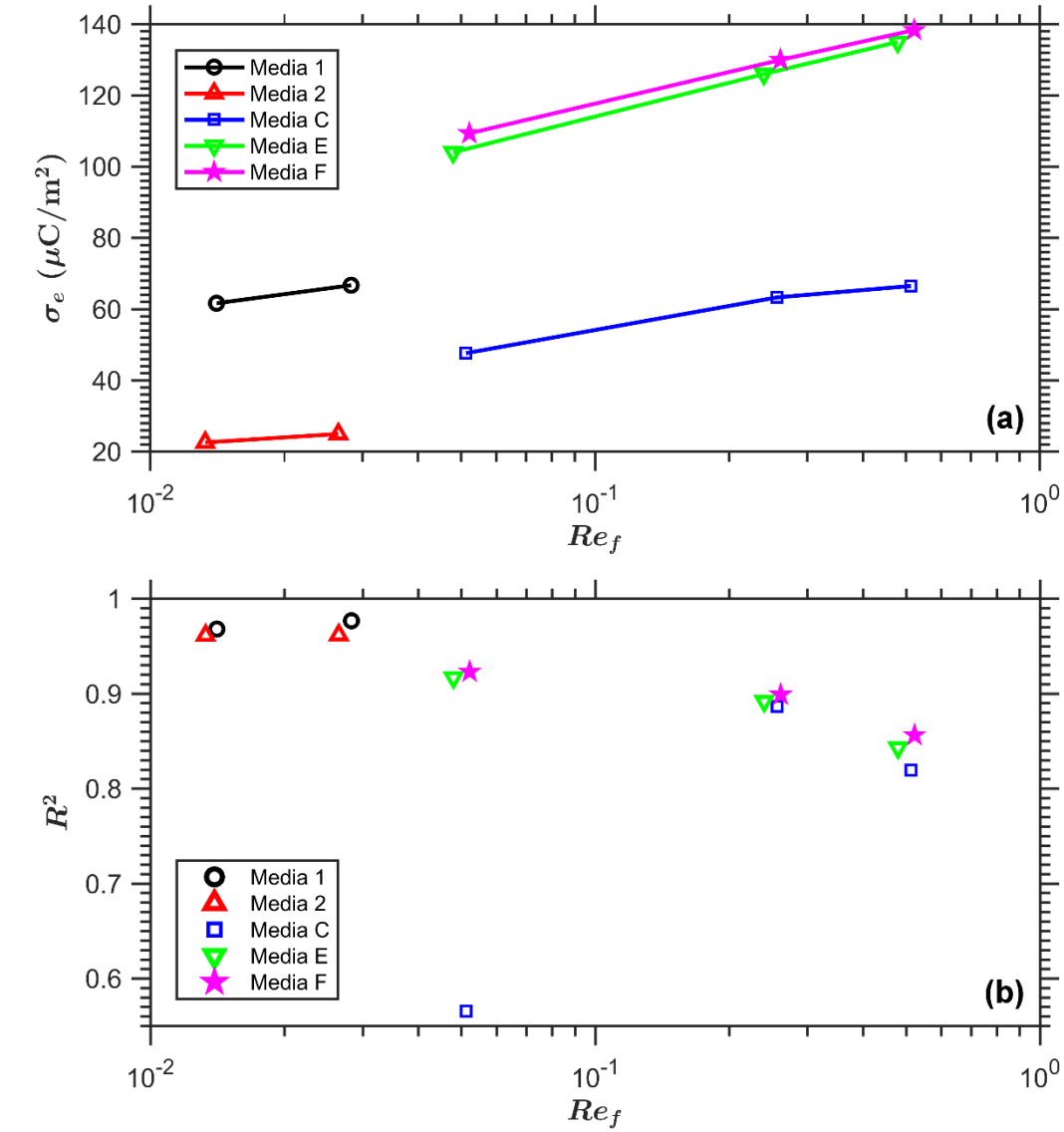

Fig. 4.13 (a) Effective surface charge density and (b) the coefficient of determination for the effective surface charge density as a function fiber Reynolds number

Consider the experimental conditions evaluated for the fitting of σ_e for Media E listed in Table 4.3. Either uncharged particles, or charged particles large enough where dielectrophoresis is the dominant collection mechanism, make up the majority of the data. Fig. 4.14 shows the limiting trajectories of an uncharged 500 nm KCl particle for a fiber from Media E and demonstrates how the fitted σ_e for Media E increased with increasing

Re_f (which was caused by an increase in U_0). The sum of the squares of the residual between the measured penetration and that calculated by $\hat{\eta}_{\sigma 0}$ was minimized. The surrogate model $\hat{\eta}_{\sigma 0}$ is an estimation of $\eta_{\sigma 0}$ found in Eq. (13a). In general, the contribution of dielectrophoresis to the particle velocity on the cell boundary was negligible. So essentially, for a measured penetration there should be a corresponding θ_b, the angle where the limiting trajectory intersected the cell boundary. Fig. 4.13(a) shows the limiting trajectories for $\sigma_e = 104$ μC/m^2 which was fitted at $U_0 = 5$ cm/s. Fig. 4.13(b) shows the limiting trajectories for $\sigma_e = 104$ μC/m^2 at $U_0 = 50$ cm/s. At this higher face velocity and $\sigma_e = 104$ μC/m^2, the value of θ_b does not give an optimal estimate of the measured penetration. σ_e must be increased so that the terminal point of the nodal limiting trajectory moves further away from the fiber, decreasing the corresponding θ_b, and increasing $\eta_{\sigma 0}$.

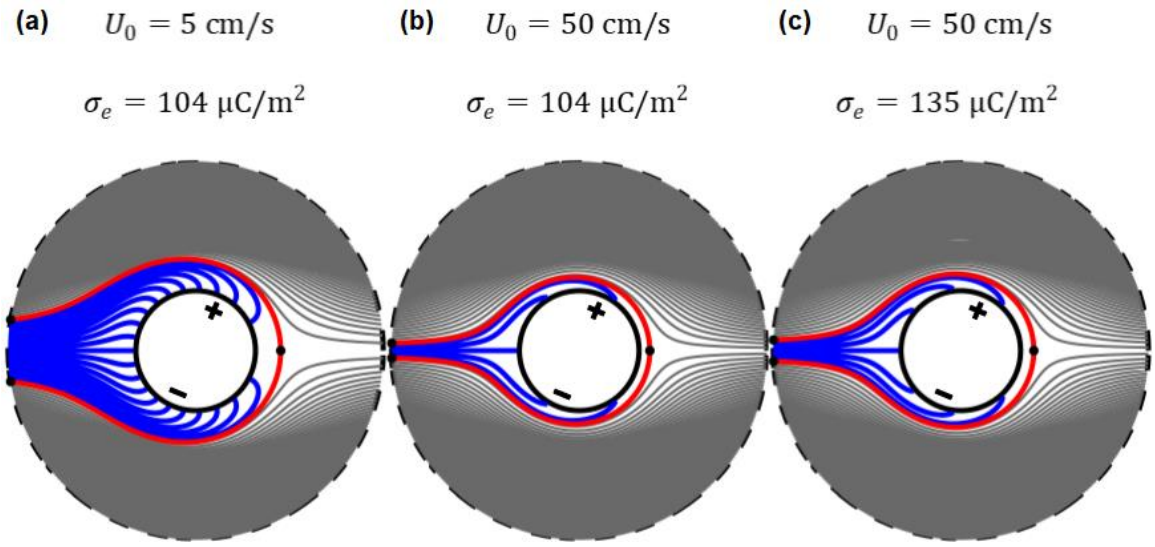

Fig. 4.14 Nodal limiting trajectories for a 500 nm uncharged KCl particle collected by a fiber from Media E with (a) $U_0 = 5$ cm/s and $\sigma_e = 104$ μC/m^2, (b) $U_0 = 50$ cm/s and $\sigma_e = 104$ μC/m^2, and (c) $U_0 = 50$ cm/s and $\sigma_e = 135$ μC/m^2

The results above may suggest that it is necessary to include the fluid inertia in the flow field model. The theoretical results of Tomotika and Aoi (1950) showed that standing eddies can form on the rear of a cylinder at Re_f as small as 0.05. This phenomenon will not be seen if Stokes' approximation is used, as is the case for the Kuwabara cell model. Podgórski (1993) speculated that such eddies may be of special interest in electret filters, where particle capture frequently occurs at the rear of the fiber, as shown in Fig. 4.14. The presence of standing eddies at the rear of the fiber would move the terminal point of the nodal limiting trajectory further away from the fiber. In fact, the presence and size of the eddy would be a function of Re_f.

The decrease in R^2 with increasing Re_f seen in Fig. 4.13(b) may also be explained by this. While most of the experimental data used to fit σ_e for Media E had dielectrophoresis as the dominant collection mechanism, which would be sensitive to the fluid velocity at the rear of the fiber, some of the data had Coulomb force as the dominant collection mechanism. For the Coulomb force, particle collection occurs near the oppositely charged dipole of the fiber. Dipole orientation was assumed to be randomly distributed, meaning the accuracy of the fluid flow at the rear of the fiber would be of less importance for particle collection by Coulomb force than by dielectrophoresis. This would make it difficult to fit a value of σ_e to satisfy both dielectrophoresis dominant and Coulomb force dominant conditions if the flow near the rear stagnation point was not described accurately. It is possible that by employing a flow field which includes the effects of fluid inertia, such as that given by Tomotika and Aoi (1950) or Podgórski (1993), the correlations observed for σ_e and R^2 with Re_f seen in Fig. 4.12 would no longer be present.

4.4.4 Assumption of Uniform Particle Concentration on the Inlet of the Flow Cell Boundary

As stated earlier in Section 4.2.1.3, Kirsch and Stechkina (1977) provided a criterion, equivalent to the Fourier number Fo, for whether the mixing by diffusion between fiber layers was sufficient for the assumption of uniform particle concentration at the cell boundary. Eq. (27) is obtained after solving Eq. (5a) for η and inserting it into the criterion $2Dh_1/U\left(d_f\eta\right)^2 \geq 1$, where for Kuwabara flow the spacing between fibers can be taken as $h_1 = d_f/\sqrt{\alpha}$.

$$Fo = \frac{32\alpha^{3/2}h^2D}{\pi^2(1-\alpha)d_f^3U_0(\ln P)^2} \geq 1 \tag{27}$$

In Fig. 4.15 the theoretical penetration for a fitted σ_e obtained from surrogate models is plotted against the measured penetration. Data for Media C, E, and F challenged by uncharged and singly charged particles at face velocities of 5, 25, and 50 cm/s is summarized. Symbols are filled if the criterion in Eq. 27 is fulfilled and empty if not. Most of the data fall within ±0.1 absolute error. Data which fulfill Eq. (27) appear to underpredict the measured penetration. However, it is difficult to draw too much of a conclusion from this analysis since the derivation of the criterion, as highlighted in Section 4.2.1.3, may no longer be applicable when forces between the fiber and particle are present.

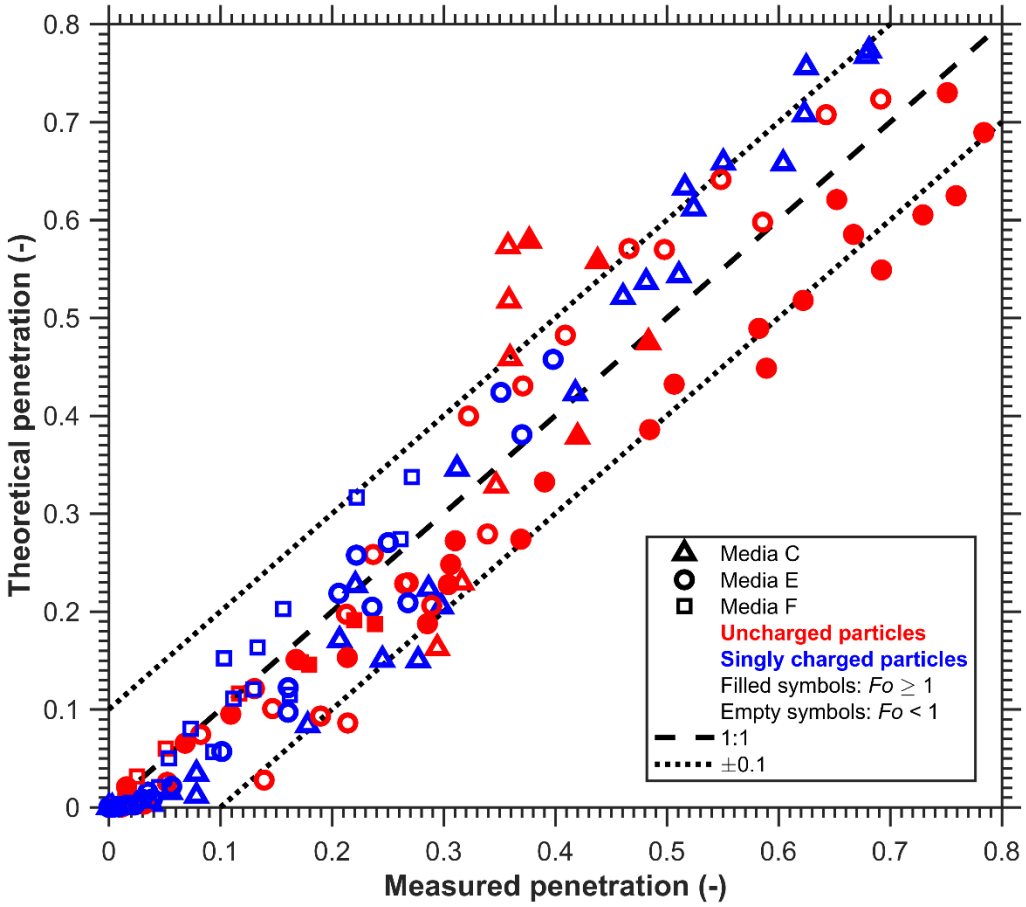

Fig. 4.15 Theoretical penetration plotted against measured penetration for Media C, E, and F challenged by uncharged and singly charged particles (charge state indicated by color) at face velocities of 5, 25, and 50 cm/s. Symbols are filled if $Fo \geq 1$ and empty if not.

4.5 Conclusion

A theoretical model to calculate the single fiber efficiency of a cylindrical electret fiber having a line dipole charge distribution was developed. Surrogate models using K-nearest neighbors classification and regression were trained, validated, and tested using the numerical results of this model. The surrogate model for single fiber efficiency for uncharged particles which considered filter solidity, particle interception, and dielectrophoretic forces had a mean relative error of less than 1%. The mean relative error in predicted single fiber efficiency was less than 6% for the surrogate model for charged particles which considered a random line dipole orientation, filter solidity, particle interception, and dielectrophoretic, image, and Coulomb forces.

Aerosol penetration estimated by the surrogate models for a best fit effective surface charge density were compared to experimentally evaluated electret filters. Coefficients of determination for the fitted effective surface charge densities ranged from 0.82 to 0.98 and the effective surface charge densities were comparable to values reported in the literature. The small disagreements which were present between experimental and theoretical aerosol penetration were likely attributable to the omission of the fluid inertia in the flow model, the coupling of Brownian forces and dielectrophoretic forces, and for very high single fiber efficiencies, the influence of neighboring fibers

5 Accomplishments and Recommendations

5.1 Accomplishments

Chapter 2:

The use of direct-reading particle instruments was shown to be an effective means by which to assess efficacy of the engineering and administrative controls and to identify the potential for inhalation exposure in the production of engineered nanoparticles when incidental nanoparticle concentrations were negligible, as was the case in the inductively coupled plasma synthesis case study. Here, a release of submicrometer particles was detected when a sampling filter was disconnected from the reactor system. Additional local exhaust ventilation was installed for this process as a result of the study.

Chapter 3:

For the case study involving the manufacture of nanocomposite containing multi-walled carbon nanotubes (MWCNTs), nanoparticle number concentrations exceeding 200,000 particles/cm^3 were present on the manufacturing floor during nanocomposite production. Through additional analyses, including the determination of the organic carbon (OC) mass concentration by thermo-optical speciation and the measurement of the particle size distribution of the nonvolatile aerosols through the use of an oxidation catalyst, it was believed that these were incidental nanoparticles consisting largely of organic material that were produced by the heating of the polymer in the extruder. Because of the high concentrations of incidental nanoparticles, area and personal breathing zone (PBZ)

sampling followed by either thermo-optical speciation for elemental carbon (EC) or observation by scanning electron microscopy (SEM) was found to be a more reliable method for detecting the presence of airborne MWCNTs.

All eight of the respirable PBZ samples had estimated 8-h time weighted average EC concentrations below the limit of detection, which was typically less than the recommended exposure limit for CNTs. Analysis of area total suspended particulate samples by SEM found MWCNTs on 10 of the 11 samples collected in the facility. While some free, individual MWCNTs were found, most of the MWCNT structures observed were in the form of ropey, micrometer-sized agglomerates.

Chapter 4:

A theoretical model to predict the single fiber efficiency of a cylindrical electret fiber having a line dipole charge distribution was developed. The numerical results were implemented into surrogate models which considered a random fiber orientation, filter solidity, particle interception, and dielectrophoretic, image, and Coulomb forces. The mean error of predicted single fiber efficiencies for the surrogate models for charged and uncharged particles were 6% and 0.8%, respectively. Aerosol penetration estimated by the surrogate models for a best fit effective surface charge density were compared to experimentally evaluated electret filters. Coefficients of determination between experimental data and surrogate models for the fitted effective surface charge densities ranged from 0.82 to 0.98 and the effective surface charge densities were comparable to values reported in the literature.

5.2 Recommendations

5.2.1 Strategies to Avoid Potential Complications Due to Elevated Organic Carbon Concentration in the Thermo-Optical Speciation of Elemental Carbon for Exposure Studies Involving Nanocomposites

Corrections should be made for artifacts caused by adsorbed organic vapor by sampling with tandem quartz filters and subtracting the OC measured on the bottom filter from that measured on the top filter (Birch, 2004). If possible, thermal analysis of the bulk materials which constitute the nanocomposite, or the nanocomposite as whole, should be performed to determine onset of oxidation and confirm complete oxidation (NIOSH, 2013b). If high nanoparticle concentrations are present near extrusion processes, it is likely that there will also be high OC concentrations. The monitoring of organic vapor concentrations with sorbent tubes may be pertinent for fully characterizing worker exposure, as potential health effects may be additive or synergistic with co-exposures.

5.2.2 Development of Surrogate Models Using Stochastic Variational Inference Gaussian Processes

Gaussian process regression was identified as a promising method for the development of a surrogate model for numerical data. Gaussian process regression can interpolate observations and compute empirical confidence intervals. However, since traditional Gaussian process regression can typically only handle datasets with fewer than 10k points, scalable Gaussian processes must be used. A paper from Hensman et al. (2013) for Gaussian processes for Big Data was found. The concepts outlined in it are included in the Stochastic Variational Inference model in GPy (SVI-GP), the Gaussian processes

framework in Python made available by researchers in the Department of Computer Science at The University of Sheffield.

5.2.3 Collection Efficiency of Submicrometer Uncharged Aerosol Particles in Electret Filters at Small Reynolds Numbers

As discussed in Section 4.4.3, there is some evidence that the omission of fluid inertia in the flow model introduced Re_f dependencies in the fitted effective charge density. The Kuwabara flow model presently used could be replaced with a solution to Oseen's flow, such as Tomotika and Aoi (1950) or Podgórski (1993), to see if these dependencies still hold. If not, it would it be interesting to measure the filtration efficiency of Media E challenged by uncharged Ag and KCl particles at increasingly lower values of Re_f. Then one could see if σ_e found for Kuwabara flow approaches a constant value as Re_f approaches zero. Uncharged particles should be chosen here because (1) the effect of fluid inertia near the rear of the fiber should be more pronounced on the single fiber efficiency of uncharged particles and (2) if one would want to later use the data for the validation of a surrogate model, the development of a model with 4 features for uncharged particle (α, N_R, N_{Di}, and Re_f) would be much more feasible than a 6 feature model for charged particles (α, N_R, N_{Di} , N_{Im}, N_C, and Re_f).

5.2.4 Effect of Multipolar Dielectrophoretic Force and Nonuniform Fiber Charge Distributions on the Filtration Efficiency of Electret Filters

In the model presented in Chapter 4, the electret fiber was assumed to be cylindrical with a line dipole charge distribution and the orientation of the dipole was assumed to be random. This charge distribution has been used frequently by modelers and originally was

a simplification for the electric field generated fiber with rectangular cross-section generated by the fibrillation of an electret film (Brown, 1981). Electret filter media can be manufactured by a variety of techniques and these means of production will determine the filter structure, charge distribution, stability, and magnitude of the internal electric field (Myers and Arnold, 2003).

Through the use of Electrostatic Force Microscopy, Bonilla et al. (2012) observed the spatial distribution of charge on fibers from electret filter media composed of melt blown polypropylene non-woven mats charged via corona treatment. Their results showed that the fibers had a heterogeneous surface charge distribution with larger variations along the length of the fiber.

Few theoretical studies have investigated the effects of charge distributions more complicated than the most commonly used line dipole configuration. Thorpe and Brown (1991) (also in Brown (1993)) found that when the number of poles on a cylindrical fiber are increased, the single fiber efficiency decreases when the surface charge density remains constant. Chernyakov and Kirsh (2015) derived formulas for the electric fields generated by charges arbitrarily distributed over the surface of a cylindrical fiber. They found that there is a range of sizes for charged particles where a more nonuniform charge distribution will lead to an increase in efficiency.

Both of the studies above used the equation from Pohl (1958) to calculate dielectrophoretic forces. However, this form of the equation is based on the approximation that only the dipole is produced. When a particle is in a highly non-uniform field, this equation will fail to predict particle behavior because of the neglect of induced higher-order moments (Washizu and Jones, 1994). Washizu and Jones (1994) provided an

equation to calculate the higher-order dielectrophoretic force terms. Applying this definition of the dielectrophoretic force to the equations derived by Chernyakov and Kirsh (2015) for the electric fields generated by charges arbitrarily distributed over the surface of a cylindrical fiber could lead to a better insight on the relation between electret charge configuration and single fiber efficiency.

5.2.5 Evaluation of Electret Charge Configuration by Deposition of Charged Fluorescing Particles

A qualitative investigation of the charge distribution on electret fibers may be done by challenging an electret filter with positively and/or negatively charged fluorescent particles, fixing and sectioning the filter, then inspecting it under optical or fluorescence microscope. Kim et al. (2006) evaluated the charging state of resin wool filters by depositing charged polystyrene latex particles of both polarities. Even with a filtration area of 0.33 cm^2, loading times of over 48 hours were needed to deposit a sufficient number of particles.

These low particle concentrations were a result of the aerosol generation method used (atomization of a PSL solution, followed by dryer, then neutralizer, then corona charger, and finally selection by DMA). A vibrating-orifice aerosol generator (VOAG) can produce highly monodisperse solid and liquid particles approximately 0.50 to 50 μm in diameter at concentrations higher than generally achievable with atomization of PSL followed by classification by DMA (Berglund and Liu, 1973). Solid, spherical, fluorescing particles can be generated by the VOAG from a solution of ammonium hydroxide and fluorescein powder (Stöber and Flachsbart, 1973; Vanderpool and Rubow, 1988).

However, at these larger sizes the particles must be highly charged for Coulombic forces, which will follow field lines, to dominate dielectrophoretic forces. Reischl et al. (1977) developed a method to generate uniform electric charging on particles produced by the VOAG with a minor modification. With the addition of an induction cap, where a small voltage is applied, one can induce charges with magnitudes up to the Rayleigh limit of the droplets prior to evaporation. After the loading of fluorescing particles, the filter could be fixed by adhesive vapor (Vaughan and Brown, 1996) prior to embedding in resin, sectioning by microtome, and imaging by optical or fluorescence microscopy.

Bibliography

Anderson, EW, McCall DW. (1958) The dielectric constant and loss of polypropylene. *Journal of Polymer Science*; 31(122): 241-242.

Asbach C, Kaminski H, Fissan H, Monz C, Dahmann D, Mülhopt S, Paur HR, Kiesling HJ, Herrmann F, Voetz M, Kuhlbusch TAJ. (2009) Comparison of four mobility particle sizers with different time resolution for stationary exposure measurements. *Journal of Nanopartle Research*; 11(7):1593-1609.

Banks DO, Kurowski GJ. (1983) A perturbation method for the approximation of the inertial collection efficiency for fibrous filters with electrical enchancement. *Journal of Aerosol Science*; 14(4): 463-473.

Barber CB, Dobkin DP, Huhdanpaa H. (1996) The quickhull algorithm for convex hulls. *ACM Transactions on Mathematical Software*; 22(4): 469-483.

Baughman RH, Zakhidov AA, de Heer WA. (2002) Carbon nanotubes--the route toward applications. *Science*; 297: 787-92.

Baumgartner H, Loffler F. (1987) Particle collection in electret fibres filters. A basic theoretical and experimental study. *Filtration & Separation*; 24(5): 346-351.

Bello D, Hart A, Ahn K, Hallock M, Yamamoto N, Garcia E, Ellenbecker M, Wardle B. (2008a) Particle exposure levels during cvd growth and subsequent handling of vertically-aligned carbon nanotube films. *Carbon*; 46: 974-77.

Bello D, Wardle BL, Yamamoto N, Guzman deVilloria R, Garcia EJ, Hart AJ, Ahn K, Ellenbecker MJ, Hallock M. (2008b) Exposure to nanoscale particles and fibers during machining of hybrid advanced composites containing carbon nanotubes. *Journal of Nanoparticle Research*; 11: 231-49.

Berglund RN, Liu BYH. (1973) Generation of monodisperse aerosol standards. *Environmental Science & Technology*; *7*(2): 147-153.

Birch ME, Ku BK, Evans DE, Ruda-Eberenz TA. (2011) Exposure and emissions monitoring during carbon nanofiber production--part i: Elemental carbon and iron-soot aerosols. *The Annals of Occupational Hygiene*; 55: 1016-36.

Birch ME. (2011) Exposure and emissions monitoring during carbon nanofiber production--part ii: Polycyclic aromatic hydrocarbons. *The Annals of Occupational Hygiene*; 55: 1037-47.

Birch ME. (2004) Monitoring of diesel particulate exhaust in the workplace. In: Schlecht PC, O'Connor PF, editors. *NIOSH manual of analytical methods (NMAN)*. Third Supplement to NMAM, 4th Edition ed. Cincinnati, OH: Dept. of Health and Human

Services, Public Health Service, Center for Disease Control and Prevention, National Institute for Occupational Safety and Health.

Bonilla R, ÁVila A, Montenegro C, Hinestroza J. (2012) Direct observation of the spatial distribution of charges on a polypropylene fiber via Electrostatic Force Microscopy. *Journal of Microscopy*; 248(3): 266-270.

Brown RC. (1979) Electrical effects in dust filters. In: *Second World Filtration Congress, London, 1979*, Uplands Press, Croydon, England.

Brown RC. (1981) Capture of dust particles in filters by linedipole charged fibres. *Journal of Aerosol Science*; 12(4): 349-356.

Brown RC. (1993) *Air filtration: an integrated approach to the theory and applications of fibrous filters*, Pergamon Press, Oxford, England.

BSI. (2007) *Nanotechnologies - part 2: Guide to safe handling and disposal of manufactured nanomaterials*. PD 6699-2-2007. London: British Standards Institute.

Cao YH, Cheung CS, Yan ZD. (2004) Numerical Study of an Electret Filter Composed of an Array of Staggered Parallel Rectangular Split-Type Fibers. *Aerosol Science and Technology*; 38(6): 603-618.

Cena LG, Peters TM. (2011) Characterization and control of airborne particles emitted during production of epoxy/carbon nanotube nanocomposites. *Journal of Occupational and Environmental Hygiene*; 8: 86-92.

CFR. (2007) *29 cfr 1910.1000, chapter xvii—occupational safety and health administration. Code of federal regulations, table z-1, limits for air contaminants*. Washington, D.C.: U.S. Federal Register; 2007.

Chang DQ, Chen SC, Pui DYH. (2016) Capture of Sub-500 nm Particles Using Residential Electret HVAC Filter Media-Experiments and Modeling. *Aerosol and Air Quality Research*; 16: 3349-3357.

Chang DQ, Chen SC, Fox AR, Viner AS, Pui DYH. (2015) Penetration of Sub-50 nm Nanoparticles Through Electret HVAC Filters Used in Residence. *Aerosol Science and Technology*; 49(10): 966-976.

Chen BT, Schwegler-Berry D, McKinney W, Stone S, Cumpston JL, Friend S, Porter DW, Castranova V, Frazer DG. (2012) Multi-walled carbon nanotubes: sampling criteria and aerosol characterization. *Inhalation Toxicology*; 24: 798-820.

Chen SC, Chang DQ, Pei C, Tsai CJ, Pui DYH. (2016) Removal Efficiency of Bimodal PM2.5 and PM10 by Electret Respirators and Mechanical Engine Intake Filters. *Aerosol and Air Quality Research*;16(7): 1722-1729.

Chen SC, Wang J, Bahk YK, Fissan H, Pui DYH. (2014) Carbon Nanotube Penetration Through Fiberglass and Electret Respirator Filter and Nuclepore Filter Media: Experiments and Models. *Aerosol Science and Technology*; 48(10): 997-1008.

Chernyakov AL, Kirsh AA. (2015) Efficiency of filtration through fibrous materials with nonuniform charge distribution on fibers. *Colloid Journal*; 77(6): 802-811.

Conny JM, Klinedinst DB, Wight SA, Paulsen JL. (2003) Optimizing thermal-optical methods for measuring atmospheric elemental (black) carbon: a response surface study. *Aerosol Science and Technology*; 37: 703-723.

Dahm MM, Evans DE, Schubauer-Berigan MK, Birch ME, Fernback JE. (2012) Occupational exposure assessment in carbon nanotube and nanofiber primary and secondary manufacturers. *The Annals of Occupational Hygiene*; 56: 542-56.

Dahm MM, Schubauer-Berigan MK, Evans DE, Birch ME, Fernback JE, Deddens JA. (2015) Carbon Nanotube and Nanofiber Exposure Assessments: An Analysis of 14 Site Visits. *The Annals of Occupational Hygiene*; 59(6): 705-723.

Dahm MM, Yencken MS, Schubauer-Berigan MK. (2011) Exposure control strategies in the carbonaceous nanomaterial industry. *Journal of Occupational and Environmental Medicine*; 53: S68-73.

Davies CN. (1953) The separation of airborne dust and particles. *Proceedings of the Institution of Mechanical Engineers, Part B: Management and engineering manufacture*; 1(1-12): 185-213.

De Volder MF, Tawfick SH, Baughman RH, Hart AJ. (2013) Carbon nanotubes: Present and future commercial applications. *Science*; 339: 535-9.

D'Errico J. (2009) In hull (Version 1.2). MATLAB Central File Exchange. Retrieved from https://www.mathworks.com/matlabcentral/fileexchange/10226-inhull

Driscoll TA, Hale N, Trefethen LN. (2014) *Chebfun guide*, Pafnuty Publications, Oxford.

Dvorak M, Dietrich F (2001) A new powder feeder for the transport of ultrafine powders. In: Berndt CCK, Khiam A.; Lugscheider, Erich F. (ed) *Thermal spray 2001: New surfaces for a new millennium,* Singapore, 2001, ASM International, pp 539-541

Emi H, Kanaoka C, Otani Y, Ishiguro T. (1987) COLLECTION MECHANISMS OF ELECTRET FILTER. *Particulate Science and Technology*; 5(2): 161-171.

Evans DE, Turkevich LA, Roettgers CT, Deye GJ, Baron PA (2013) Dustiness of fine and nanoscale powders. *The Annals of Occupational Hygiene*; 57(2): 261-277

Fleury D, Bomfim JAS, Vignes A, Girard C, Metz S, Muñoz F, R'Mili B, Ustache A, Guiot A, Bouillard JX. (2013) Identification of the main exposure scenarios in the

production of cnt-polymer nanocomposites by melt-moulding process. *Journal of Cleaner Production*; 53: 22-36.

Fonseca AS, Viitanen A-K, Koivisto AJ, Kangas A, Huhtiniemi M, Hussein T, Vanhala E, Viana M, Querol X, Hämeri K. (2014) Characterization of Exposure to Carbon Nanotubes in an Industrial Setting. *The Annals of Occupational Hygiene*; 59(5): 586-599.

Fujitani Y, Kobayashi T, Arashidani K, Kunugita N, Suemura K (2008) Measurement of the physical properties of aerosols in a fullerene factory for inhalation exposure assessment. *Journal of Occupational and Environmental Hygiene*; 5(6): 380-389.

Goel NS, Spencer PR. (1975) Toner particle-photoreceptor adhesion. In: Lee LH. (ed) *Adhesion Science and Technology*, vol. 9, 763-829.

Gormley PG, Kennedy M (1948) Diffusion from a stream flowing through a cylindrical tube. *Proceedings of the Royal Irish Academy. Section A: Mathematical and Physical Sciences*; 52: 163-169.

Guo JY, Gitzhofer F, Boulos MI (1997) Effects of process parameters on ultrafine SiC synthesis using induction plasmas. *Plasma Chemistry and Plasma Processing*; 17(2): 219-249.

Han JH, Lee EJ, Lee JH, So KP, Lee YH, Bae GN, Lee SB, Ji JH, Cho MH, Yu IJ. (2008) Monitoring multiwalled carbon nanotube exposure in carbon nanotube research facility. *Inhalation Toxicology*; 20: 741-749.

Hector LG, Schultz HL. (1936) The Dielectric Constant of Air at Radiofrequencies. *Physics*; 7(4): 133-136.

Hedmer M, Isaxon C, Nilsson PT, Ludvigsson L, Messing ME, Genberg J, Skaug V, Bohgard M, Tinnerberg H, Pagels JH. (2014) Exposure and emission measurements during production, purification, and functionalization of arc-discharge-produced multi-walled carbon nanotubes. *The Annals of Occupational Hygiene*; 58: 355-79.

Heitbrink WA, Evans DE, Ku BK, Maynard AD, Slavin TJ, Peters TM. (2009) Relationships among particle number, surface area, and respirable mass concentrations in automotive engine manufacturing. *Journal of Occupational and Environmental Hygiene*; 6: 19-31.

Heitbrink WA, Lo LM, Dunn KH. (2015) Exposure Controls for Nanomaterials at Three Manufacturing Sites. *Journal of Occupation and Environmental Hygiene*; 12: 16-28.

Hellmann A, Schmidt K, Ripperger S, Berges M (2012) Release of ultrafine dusts during the machining of nanocomposites. *Gefahrstoffe Reinhaltung der Luft*; 72: 473-476.

Helsel D. (2010) Much ado about next to nothing: Incorporating nondetects in science. *The Annals of Occupational Hygiene*; 54: 257-62.

Hensman J, Fusi N, Lawrence N. (2013) Gaussian Processes for Big Data. In: *Proceedings of the Twenty-Ninth Conference on Uncertainty in Artificial Intelligence*. AUAI Press.

Huang G, Park JH, Cena LG, Shelton BL, Peters TM (2012) Evaluation of airborne particle emissions from commercial products containing carbon nanotubes. *Journal of Nanoparticle Research*; 14: 1231.

Hubbard JA, Brockmann JE, Dellinger J, Lucero DA, Sanchez AL, Servantes BL. (2012) Fibrous Filter Efficiency and Pressure Drop in the Viscous-Inertial Transition Flow Regime. *Aerosol Science and Technology*;, 46(2): 138-147.

Hubert M, Vandervieren E. (2008) An adjusted boxplot for skewed distributions. *Computational Statistics & Data Analysis*; 52(12): 5186-5201.

Hwang D, Bradley J (2010) The recession's ripple effect on nanotech. *Lux Reseach, Inc., New York, NY*

ICRP. (1994) Human respiratory tract model for radiological protection. *Annals of the ICRP*; 24:(1-3).

Iijima S. (1991) Helical microtubules of graphitic carbon. *Nature*; 354: 56-58.

Incropera FP, Lavine AS, Bergman TL, DeWitt DP. (2007). *Fundamentals of Heat and Mass Transfer*, 6th ed., John Wiley & Sons, Hoboken, New Jersey.

International Organization for Standardization. (2009). *Particulate air filters for general ventilation -- Determination of filtration performance (ISO/TS Standard No. 21220:2009).*

International Organization for Standardization. (2016). *Air filters for general ventilation -- Part 1: Technical specifications, requirements and classification system based upon particulate matter efficiency (ePM) (ISO Standard No. 1690-1:2016).*

Iwasaki T, Slade JJ, Stanley WE. (1937). SOME NOTES ON SAND FILTRATION [with Discussion]. *Journal - American Water Works Association)*; 29(10): 1591-1602.

Jensen KA, Koponen IK, Clausen PA, Schneider T (2008) Dustiness behaviour of loose and compacted bentonite and organoclay powders: What is the difference in exposure risk? *Journal of Nanopart Research*; 11(1):133-146.

Jeong CH, Evans GJ (2009) Inter-comparison of a fast mobility particle sizer and a scanning mobility particle sizer incorporating an ultrafine water-based condensation particle counter. *Aerosol Science and Technology*; 43(4): 364-373.

Ji JH, Kim JB, Lee G, Bae GN. (2015) Nanomaterial release characteristics in a single-walled carbon nanotube manufacturing workplace. *Journal of Nanoparticle Research*; 17: 77.

Johnson DR, Methner MM, Kennedy AJ, Steevens JA. (2010) Potential for occupational exposure to engineered carbon-based nanomaterials in environmental laboratory studies. *Environmental Health Perspectives*; 118: 49-54.

Jones E, Oliphant E, Peterson P, others. (2001-) SciPy: Open source scientific tools for Python (Version 0.19.1). Retrieved from http://www.scipy.org/

Jones TB. (1995) *Electromechanics of particles*. Cambridge University Press, New York, New York

Kanaoka C, Emi H, Otani Y, Iiyama T. (1987) Effect of Charging State of Particles on Electret Filtration. *Aerosol Science and Technology*; 7(1): 1-13.

Kelly WP, McMurry PH (1992) Measurement of particle density by inertial classification of differential mobility analyzer-generated monodisperse aerosols. *Aerosol Science and Technology*; 17(3): 199-212

Khan B, Hays MD, Geron C, Jetter J. (2011) Differences in the oc/ec ratios that characterize ambient and source aerosols due to thermal-optical analysis. *Aerosol Science and Technology*; 46: 127-37.

Kim JH, Mulholland GW, Kukuck SR, Pui DYH. (2005) Slip Correction Measurements of Certified PSL Nanoparticles Using a Nanometer Differential Mobility Analyzer (Nano-DMA) for Knudsen Number From 0.5 to 83. *Journal of Research of the National Institute of Standards and Technology*; 110(1): 31-54.

Kim JC, Otani Y, Chung JD. (2006). Evaluation of Charging State of Resin Wool Filter by Deposition of Charged Particles. *Earozoru Kenkyu*; 21(2), 153-159.

Kirsch AA, Stechkina IB. (1977). Inertial deposition of aerosol particles in model filters at low reynolds numbers. *Journal of Aerosol Science*;, 8(5): 301-307.

Kuhlbusch TA, Asbach C, Fissan H, Gohler D, Stintz M. (2011) Nanoparticle exposure at nanotechnology workplaces: A review. *Particle and Fibre Toxicology*; 8:22.

Kuhlbusch TA, Fissan H. (2006) Particle characteristics in the reactor and pelletizing areas of carbon black production. *Journal of Occupational and Environmental Hygiene*; 3: 558-67.

Kuhlbusch TA, Neumann S, Fissan H. (2004) Number size distribution, mass concentration, and particle composition of PM1, PM2.5, and PM10 in bag filling areas of carbon black production. *Journal of Occupational and Environmental Hygiene*; 1: 660-71.

Kuo YY, Zhang H, Gerecke A, Wang J. (2014) Chemical composition of nanoparticles released from thermal cutting of polystyrene foams and the associated isomerization of hexabromocyclododecane (HBCD) diastereomers. *Aerosol and Air Quality Research*; 14:1114-1120.

Kuwabara S. (1959) The Forces experienced by Randomly Distributed Parallel Circular Cylinders or Spheres in a Viscous Flow at Small Reynolds Numbers. *Journal of the Physical Society of Japan*; 14(4): 527-532.

Laboratory for Insulation Research, Massachusetts Institute of Technology. (1953) *Tables of Dielectric Materials, Volume IV*. Technical Report No. 57. Cambridge, Massachusetts.

Langmuir, I. (1942) *Report on Smoke and Filters*. OSRD 865. Washington, D.C.

Lathrache R, Fissan H. (1987) Enhancement of particle deposition in filters due to electrostatic effects. *Filtration & Separation*; 24(6): 418-422.

Lathrache R, Fissan H. (1989) Grundlegende Untersuchungen zum Abscheideverhalten der Elektret-Filter. I: Bestimmung der Abscheidegrade. *Staub. Reinhaltung der Luft*; 49(9): 309-314.

Lathrache R, Fissan HJ, Neumann S. (1986) Deposition of submicron particles on electrically charged fibers. *Journal of Aerosol Science*; 17(3): 446-449.

Leconte Y, Leparoux M, Portier X, Herlin-Boime N (2008) Controlled synthesis of β-SiC nanopowders with variable stoichiometry using inductively coupled plasma. *Plasma Chemistry and Plasma Processing*; 28(2): 233-248.

Lee JH, Ahn KH, Kim SM, Kim E, Lee GH, Han JH, Yu IJ. (2015) Three-Day Continuous Exposure Monitoring of CNT Manufacturing Workplaces. *BioMed Research International*; Article ID 237140.

Lee JH, Kwon M, Ji JH, Kang CS, Ahn KH, Han JH, Yu IJ (2011) Exposure assessment of workplaces manufacturing nanosized TiO2 and silver. *Inhalation Toxicology*; 23(4): 226-236

Lee JH, Lee SB, Bae GN, Jeon KS, Yoon JU, Ji JH, Sung JH, Lee BG, Yang JS, Kim HY, Kang CS, Yu IJ. (2010) Exposure assessment of carbon nanotube manufacturing workplaces. *Inhalation Toxicology*; 22: 369-81.

Lee JS, Choi YC, Shin JH, Lee JH, Lee Y, Park SY, Baek JE, Park JD, Ahn K, Yu IJ. (2014) Health surveillance study of workers who manufacture multi-walled carbon nanotubes. Nanotoxicology; 9(6): 802-811.

Lee KW, Liu BYH. (1982) Theoretical Study of Aerosol Filtration by Fibrous Filters. *Aerosol Science and Technology*; 1(2): 147-161.

Lee M, Otani Y, Namiki N, Emi H. (2002) Prediction of Collection Efficiency of High-performance Electret Filters. *Journal of Chemical Engineering of Japan*; 35(1): 57-62.

Lee MH, Otani Y, Namiki N, Emi H. (2002) Interaction between Brownian Diffusion and Coulombic Force in Electret Filtration. *Earozoru Kenkyu*; 17(4): 277-283.

Leparoux M, Leconte Y, Wirth A, Buehler T (2010) In situ treatment of thermal RF plasma processed nanopowders to control their agglomeration and dispersability. *Plasma Chemisry and Plasma Processing*; 30(6): 779-793.

Leparoux M, Schreuders C, Shin JW, Siegmann S (2005) Induction plasma synthesis of carbide nano-powders. *Advanced Engineering Materials*; 7(5): 349-353.

Leparoux M, Siegmann S (2003) Development of a filtration unit with a by-pass sampling system for nanoparticle collection. In: *Filtech Europa 2003*, Düsseldorf, Germany, October 21 - 23, 2003 2003. pp II-243/II-249

Li L, Zuo Z, Japuntich DA, Pui DYH. (2012) Evaluation of Filter Media for Particle Number, Surface Area and Mass Penetrations. *Annals of Occupational Hygiene*; 56(5): 581-594.

Liu X, Hurt RH, Kane AB. (2010) Biodurability of single-walled carbon nanotubes depends on surface functionalization. *Carbon*; 48: 1961-69.

Lux Research. (2016) Nanotechnology update: U.S. Leads in government spending amidst increased spending across asia. *Lux Research, Inc., New York, New York*.

Maynard A, Pui DH (2007) Nanotechnology and occupational health: New technologies – new challenges. *Journal of Nanoparticle Research*; 9(1): 1-3.

Maynard AD, Baron PA, Foley M, Shvedova AA, Kisin ER, Castranova V. (2004) Exposure to carbon nanotube material: Aerosol release during the handling of unrefined single-walled carbon nanotube material. *Journal of Toxicology and Environmental Health Part A*; 67: 87-107.

Mercer RR, Hubbs AF, Scabilloni JF, Wang L, Battelli LA, Friend S, Castranova V, Porter DW. (2011) Pulmonary fibrotic response to aspiration of multi-walled carbon nanotubes. *Particle and Fibre Toxicology*; 8: 21.

Mercer RR, Hubbs AF, Scabilloni JF, Wang L, Battelli LA, Schwegler-Berry D, Castranova V, Porter DW. (2010) Distribution and persistence of pleural penetrations by multi-walled carbon nanotubes. *Particle and Fibre Toxicology*; 7: 28.

Methner M, Beaucham C, Crawford C, Hodson L, Geraci C. (2012a) Field application of the nanoparticle emission assessment technique (NEAT): Task-based air

monitoring during the processing of engineered nanomaterials (ENM) at four facilities. *Journal of Occupational and Environmental Hygiene*; 9: 543-55.

Methner M, Crawford C, Geraci C. (2012b) Evaluation of the potential airborne release of carbon nanofibers during the preparation, grinding, and cutting of epoxy-based nanocomposite material. *Journal of Occupational and Environmental Hygiene*; 9: 308-18.

Methner M, Hodson L, Dames A, Geraci C (2010) Nanoparticle Emission Assessment Technique (NEAT) for the identification and measurement of potential inhalation exposure to engineered nanomaterials--Part B: Results from 12 field studies. *Journal of Occupational and Environmental Hygiene*; 7(3): 163-176.

Methner M, Hodson L, Geraci C. (2010) Nanoparticle emission assessment technique (NEAT) for the identification and measurement of potential inhalation exposure to engineered nanomaterials--part a. *Journal of Occupational and Environmental Hygiene*; 7: 127-132.

Methner MM, Birch ME, Evans DE, Ku BK, Crouch K, Hoover MD. (2007) Identification and characterization of potential sources of worker exposure to carbon nanofibers during polymer composite laboratory operations. *Journal of Occupational and Environmental Hygiene;* 4: D125-30.

Miller AL, Drake PL, Murphy NC, Cauda EG, LeBouf RF, Markevicius G. (2013) Deposition uniformity of coal dust on filters and its effect on the accuracy of FTIR analyses for silica. *Aerosol Science and Technology*; 47: 724-733.

Mouret G, Thomas D, Chazelet S, Appert-Collin JC, Bemer D. (2009) Penetration of nanoparticles through fibrous filters perforated with defined pinholes. *Journal of Aerosol Science*; 40(9): 762-775.

Muller J, Huaux Fo, Fonseca A, Nagy JB, Moreau N, Delos M, Raymundo-Piñero E, Béguin Fo, Kirsch-Volders M, Fenoglio I, Fubini B, Lison D. (2008) Structural defects play a major role in the acute lung toxicity of multiwall carbon nanotubes: Toxicological aspects. *Chemical Research in Toxicology*; 21: 1698-705.

Murphy FA, Poland CA, Duffin R, Donaldson K. (2013) Length-dependent pleural inflammation and parietal pleural responses after deposition of carbon nanotubes in the pulmonary airspaces of mice. *Nanotoxicology*; 7: 1157-1167.

Myers DL, Arnold BD. (2003) Electret media for HVAC filtration applications. *International Nonwovens Journal*; 1: 43-54.

National Institute for Occupational Safety and Health Division of Applied Research and Technology (DART) (2016) *Hierarchy of controls*. Available: https://www.cdc.gov/niosh/topics/hierarchy/default.html [accessed November 28, 2017 2017].

Nielsen KA. (1978) Collection of inertialess particles on circular cylinders with electrical forces and gravitation. *Journal of Colloid and Interface Science*; 64(1): 131-142.

NIOSH. (2003a) Diesel particulate mater (as elemental carbon): Method 5040. In: NIOSH, editor. *DHHS (NIOSH) Publication No. 94-113*. Cincinnati, OH: U.S. Department of Health and Human Services PHS, Centers for Disease Control and Prevention, National Institute for Occupational Safety and Health.

NIOSH. (2003b) Particles not otherwise regulated, respirable: Method 0600. In: NIOSH, editor. *DHHS (NIOSH) Publication No. 94-113*. Cincinnati, OH: U.S. Department of Health and Human Services PHS, Centers for Disease Control and Prevention, National Institute for Occupational Safety and Health.

NIOSH. (2009) Approaches to safe nanotechnology: Managing the health and safety concerns associated with engineered nanomaterials. In NIOSH editor. *DHHS (NIOSH) Publication No. 2009-125*. Cincinnati, OH: US Department of Health and Human Services, Centers for Disease Control and Prevention, National Institute for Occupational Safety and Health.

NIOSH. (2012) Filling the knowledge gaps for safe nanotechnology in the workplace: A progess report from the NIOSH Nanotechnology Research Center, 2004-2011. In NIOSH editor. *DHHS (NIOSH) Publication No. 2013-101*. Cincinnati, OH: US Department of Health and Human Services, Centers for Disease Control and Prevention, National Institute for Occupational Safety and Health.

NIOSH. (2013a) Current strategies for engineering controls in nanomaterial production and downstream handling processes. In NIOSH editor. *DHHS (NIOSH) Publication Number 2014-102*. Cincinnati, OH: US Department of Health and Human Services, Centers for Disease Control and Prevention, National Institute for Occupational Safety and Health.

NIOSH. (2013b) Current Intelligence Bulletin 65: Occupational Exposure to Carbon Nanotubes and Nanofibers. In NIOSH editor. *DHHS (NIOSH) Publication No. 2013-145*. Cincinnati, OH: US Department of Health and Human Services, Centers for Disease Control and Prevention, National Institute for Occupational Safety and Health.

Oberdörster G, Ferin J, Lehnert BE. (1994) Correlation between particle size, in vivo particle persistence, and lung injury. *Environmental Health Perspectives*; 102: 173-179.

Oberdörster G, Oberdörster E, Oberdörster J (2005) Nanotoxicology: An emerging discipline evolving from studies of ultrafine particles. *Environmental Health Perspectives*; 113(7): 823-839.

Oberdorster G, Sharp Z, Atudorei V, Elder A, Gelein R, Kreyling W, Cox C.. 2004. Translocation of inhaled ultrafine particles to the brain. *Inhalation Toxicology*; 16: 437-445.

Ogura I, Sakurai H, Mizuno K, Gamo M. (2010) Release potential of single-wall carbon nanotubes produced by super-growth method during manufacturing and handling. *Journal of Nanoparticle Research*; 13: 1265-80.

Ogura I., Kotake M., Shigeta M., Uejima M., Saito K., Hashimoto N., Kishimoto A. (2013) Potential release of carbon nanotubes from their composites during grinding. *Journal of Physics: Conference Series*; 429: 012049.

Ono-Ogasawara M, Myojo T. (2013) Characteristics of multi-walled carbon nanotubes and background aerosols by carbon analysis; particle size and oxidation temperature. *Advanced Powder Technology*; 24: 263-69.

OSHA. (2013) Table Z-1 limits for air contaminants. US Department of Labor, Occupational Safety & Health Administration. https://www.osha.gov/pls/oshaweb/owadisp.show_document?p_table=standards&p_id=9992 (Accessed 21 October 2013)

OSHA. (1997) Standard interpretation 01/23/1997 - Calculation methods used under the air contaminants standard for extended work shifts [online]. Available from: URL: https://www.osha.gov/pls/oshaweb/owadisp.show_document?p_table=INTERPRETATIONS&p_id=22333 (Accessed 6 Feb 2015).

Otani Y, Emi H, Mori J. (1993) Initial Collection Efficiency of Electret Filter and Its Durability for Solid and Liquid Particles [Translated][†]. *KONA Powder and Particle Journal*; 11: 207-214.

Park JY, Ramachandran G, Raynor PC, Olson Jr GM. (2010) Determination of particle concentration rankings by spatial mapping of particle surface area, number, and mass concentrations in a restaurant and a die casting plant. *Journal of Occupational and Environmental Hygiene*; 7: 466-476.

Pedregosa F, Varoquaux G, Gramfort A, Michel V, Thirion B, Grisel O, Blondel M, Prettenhofer P, Weiss R, Dubourg, V. (2011) Scikit-learn: Machine learning in Python. *Journal of Machine Learning Research*; 12(Oct): 2825-2830.

Pich J. (1965) The filtration theory of highly dispersed aerosols. *Staub Reinhaltung der Luft*; 5: 16-23.

Pich J. (1966) Pressure Drop of Fibrous Filters at Small Knudsen Numbers. *Annals of Occupational Hygiene*; 9(1): 23-27.

Pich J. (1971) Pressure characteristics of fibrous aerosol filters. *Journal of Colloid and Interface Science*; 37(4): 912-917.

Pich J, Emi H, Kanaoka C. (1987) Coulombic deposition mechanism in electret filters. *Journal of Aerosol Science*; 18(1): 29-35.

Podgórski A. (1993) 22 P 05 Analytical description of gas flow around a fiber for modelling of aerosol filtration. *Journal of Aerosol Science*; 24: S277-S278.

Podgórski A. (2002) On the transport, deposition and filtration of aerosol particles in fibrous filters: selected problems. *Prace Wydziału Inżynierii Chemicznej i Procesowej Politechniki Warszawskiej*; 28(1): 3-207.

Podgórski A. (2009) Estimation of the upper limit of aerosol nanoparticles penetration through inhomogeneous fibrous filters. *Journal of Nanoparticle Research*; 11(1): 197-207.

Podgórski A, Bałazy A. (2008) Novel Formulae for Deposition Efficiency of Electrically Neutral, Submicron Aerosol Particles in Bipolarly Charged Fibrous Filters Derived Using Brownian Dynamics Approach. *Aerosol Science and Technology*; 42(2): 123-133.

Podgorski A, Maißer A, Szymanski WW, Jackiewicz A, Gradon L. (2011) Penetration of Monodisperse, Singly Charged Nanoparticles through Polydisperse Fibrous Filters. *Aerosol Science and Technology*; 45(2): 215-233.

Pohl HA. (1958). Some Effects of Nonuniform Fields on Dielectrics. *Journal of Applied Physics*; 29(8): 1182.

Poland CA, Duffin R, Kinloch I, Maynard A, Wallace WA, Seaton A, Stone V, Brown S, Macnee W, Donaldson K. (2008) Carbon nanotubes introduced into the abdominal cavity of mice show asbestos-like pathogenicity in a pilot study. *Nature Nanotechnology*; 3: 423-8.

Porter DW, Hubbs AF, Chen BT, McKinney W, Mercer RR, Wolfarth MG, Battelli L, Wu N, Sriram K, Leonard S, Andrew M, Willard P, Tsuruoka S, Endo M, Tsukada T, Munekane F, Frazer DG, Castranova V. (2013) Acute pulmonary dose-responses to inhaled multi-walled carbon nanotubes. *Nanotoxicology*; 7: 1179-94.

R'mili B, Dutouquet C, Sirven JB, Aguerre-Chariol O, Frejafon E. (2010) Analysis of particle release using LIBS (laser-induced breakdown spectroscopy) and TEM (transmission electron microscopy) samplers when handling CNT (carbon nanotube) powders. *Journal of Nanoparticle Research*; 13: 563-77.

Rao N, Micheel B, Hansen D, Fandrey C, Bench M, Girshick S, Heberlein J, McMurry P (1995) Synthesis of nanophase silicon, carbon, and silicon carbide powders using a plasma expansion process. *Journal of Material Research*; 10(8): 2073-2084.

Reischl G, John W, Devor W. (1977) Uniform electrical charging of monodisperse aerosols. *Journal of Aerosol Science*; 8(1): 55-65.

Robinson A. (1956) On the motion of small particles in a potential field of flow. *Communications on Pure and Applied Mathematics*; 9(1): 69-84.

Roco MC. (2011) The long view of nanotechnology development: The national nanotechnology initiative at 10 years. In: *Nanotechnology Research Directions for Societal Needs in 2020*, vol 1. Science Policy Reports. Springer Netherlands, pp 1-28

Roco MC. (2017) Overview. In: *Nanotechnology commercialization*:John Wiley & Sons, Inc., 1-23.

Rubow KL. (1981) *Submicron aerosol filtration characteristics of membrane filters.* (PhD Thesis), University of Minnesota Minneapolis.

Sanchez AL, Hubbard JA, Dellinger JG, Servantes BL. (2013). Experimental Study of Electrostatic Aerosol Filtration at Moderate Filter Face Velocity. *Aerosol Science and Technology*; 47(6): 606-615.

Sargent L, Porter D, Staska L, Hubbs A, Lowry D, Battelli L, Siegrist K, Kashon M, Mercer R, Bauer A, Chen B, Salisbury J, Frazer D, McKinney W, Andrew M, Tsuruoka S, Endo M, Fluharty K, Castranova V, Reynolds S. (2014) Promotion of lung adenocarcinoma following inhalation exposure to multi-walled carbon nanotubes. *Particle and fibre toxicology*; 11: 3.

Schlag S, Suresh B, Yang V, Yoneyama M (2011) Nanoscale chemicals and materials applications and market overview. In: *2011 International Conference on Nanoscience, Engineering and Technology (ICONSET)*, Chennai, Tamilnadu, India, 28-30 Nov. 2011. IEEEXplore, pp 308-313

Schlagenhauf L., Chu B.T.T, Buha J., Nüesch F., Wang J. (2012) Release of carbon nanotubes from an epoxy-based nanocomposite during an abrasion process. *Environmental Science and Technology*; 46: 7366-7372.

Schneider T, Jensen KA (2008) Combined single-drop and rotating drum dustiness test of fine to nanosize powders using a small drum. *Annals of Occupational Hygiene*; 52 (1): 23-34.

Sessler GM. (1999). *Electrets, vol. 1*: Laplacian Press.

Shampine LF. (2008) Vectorized adaptive quadrature in MATLAB. *Journal of Computational and Applied Mathematics*; 211(2): 131-140.

Shampine LF, Reichelt MW. (1997) The matlab ode suite. *SIAM journal on scientific computing*; 18(1): 1-22.

Shvedova AA, Kisin E, Murray AR, Johnson VJ, Gorelik O, Arepalli S, Hubbs AF, Mercer RR, Keohavong P, Sussman N, Jin J, Yin J, Stone S, Chen BT, Deye G, Maynard

A, Castranova V, Baron PA, Kagan VE. (2008) Inhalation vs. Aspiration of single-walled carbon nanotubes in c57bl/6 mice: Inflammation, fibrosis, oxidative stress, and mutagenesis. *American Journal of Physiology - Lung Cellular and Molecular Physiology*; 295: L552-L65.

Skillas G, Maisels A, Pratsinis SE, Kodas TT (2011) Manufacturing of materials by aerosol processes. In: Baron PA, Kulkarni P, Willeke K (eds) *Aerosol Measurement - Principles, Techniques, and Applications*. 3rd edn. Wiley, Hoboken, NJ, USA, pp 751-770

Stechkina IB, Fuchs NA. (1966) Studies on Fibrous Aerosol Filters—I. Calculation of Diffusional Deposition of Aerosols in Fibrous Filters. *Annals of Occupational Hygiene*; 9(2): 59-64.

Stöber W, Flachsbart H. (1973) An evaluation of nebulized ammonium fluorescein as a laboratory aerosol. *Atmospheric Environment (1967)*; 7(7): 737-748.

Storn R, Price K. (1997) Differential Evolution – A Simple and Efficient Heuristic for global Optimization over Continuous Spaces. *Journal of Global Optimization*; 11(4): 341-359.

Swanson J, Kittelson D, Giechaskiel B, Bergmann A, Twigg M. (2013) A miniature catalytic stripper for particles less than 23 nanometers. *SAE International Journal of Fuels and Lubricants*; 6: 542-51.

Takaya M, Ono-Ogasawara M, Shinohara Y, Kubota H, Tsuruoka S, Koda S. (2012) Evaluation of exposure risk in the weaving process of MWCNT-coated yarn with real-time particle concentration measurements and characterization of dust particles. *Industrial Health*; 50: 147-55.

Thakur R, Das D, Das A. (2013) Electret Air Filters. *Separation & Purification Reviews, 42*(2), 87-129.

Thorpe A, Brown RC. (1991) A study of the electric charge in filters using monodisperse test aerosols. In: *5th Aerosol Society Conference Proceedings.*

Tomotika S, Aoi T. (1950) THE STEADY FLOW OF VISCOUS FLUID PAST A SPHERE AND CIRCULAR CYLINDER AT SMALL REYNOLDS NUMBERS. *The Quarterly Journal of Mechanics and Applied Mathematics*; 3(2): 141-161.

Tomotika S, Aoi T. (1953) THE STEADY FLOW OF A VISCOUS FLUID PAST AN ELLIPTIC CYLINDER AND A FLAT PLATE AT SMALL REYNOLDS NUMBERS. *The Quarterly Journal of Mechanics and Applied Mathematics*; 6(3): 290-312.

Tsai CJ, Liu CN, Hung SM, Chen SC, Uang SN, Cheng YS, Zhou Y. (2012) Novel active personal nanoparticle sampler for the exposure assessment of nanoparticles in workplaces. *Environmental science & technology*; 46: 4546-52.

Tsai CJ, Wu CH, Leu ML, Chen SC, Huang CY, Tsai PJ, Ko FH (2009) Dustiness test of nanopowders using a standard rotating drum with a modified sampling train. *Journal of Nanopart Research*; 11(1): 121-131.

Tsai CSJ, White D, Rodriguez H, Munoz CE, Huang CY, Tsai CJ, Barry C, Ellenbecker MJ (2012) Exposure assessment and engineering control strategies for airborne nanoparticles: an application to emissions from nanocomposite compounding processes. *Journal of Nanoparticle Research*; 14(7): 989.

Tsai SJ, Hofmann M, Hallock M, Ada E, Kong J, Ellenbecker M. (2009) Characterization and evaluation of nanoparticle release during the synthesis of single-walled and multiwalled carbon nanotubes by chemical vapor deposition. *Environmental science & technology*; 43: 6017-23.

Tsai SJC, Ashter A, Ada E, Mead JL, Barry CF, Ellenbecker MJ. (2008) Airborne nanoparticle release associated with the compounding of nanocomposites using nanoalumina as fillers. *Aerosol and Air Quality Research*; 8: 160-77.

Vanderpool RW, Rubow KL. (1988) Generation of Large, Solid, Monodisperse Calibration Aerosols. *Aerosol Science and Technology*; 9(1): 65-69.

Vaughan NP, Brown RC. (1996) Observations of the microscopic structure of fibrous filters. *Filtration & Separation*; 33(8): 741-748.

Vollath D. (2008) Plasma synthesis of nanopowders. *Journal of Nanoparticle Research*; 10 (S1): 39-57.

Waker AJ, Brown RC. (1988) Application of cavity theory to the discharge of electrostatic dust filters by x-rays. *International Journal of Radiation Applications and Instrumentation. Part A. Applied Radiation and Isotopes*; 39(7): 677-684.

Walser T, Hellweg S, Juraske R, Luechinger NA, Wang J, Fierz M. (2012) Exposure to engineered nanoparticles: Model and measurements for accident situations in laboratories. *The Science of the Total Environment*; 420: 119-126.

Wang J, Asbach C, Fissan H, Hulser T, Kaminski H, Kuhlbusch TAJ, Pui DYH. (2012) Emission measurement and safety assessment for the production process of silicon nanoparticles in a pilot-scale facility. *Journal of Nanoparticle Research*; 14(4): 1-9.

Wang J, Asbach C, Fissan H, Hülser T, Kuhlbusch TAJ, Thompson D, Pui DYH. (2011) How can nanobiotechnology oversight advance science and industry: Examples

from environmental, health, and safety studies of nanoparticles (nano-EHS). *Journal of Nanoparticle Research*; 13(4): 1373-1387.

Wang J, Thompson D, Pui DYH. (2013) Integrative filtration research and sustainable nanotechnology. *Particuology*; 11(1): 5-13.

Wang L, Castranova V, Mishra A, Chen B, Mercer R, Schwegler-Berry D, Rojanasakul Y. (2010) Dispersion of single-walled carbon nanotubes by a natural lung surfactant for pulmonary in vitro and in vivo toxicity studies. *Particle and fibre toxicology*; 7: 31.

Wang J, Chen DR, Pui DYH. (2007) Modeling of filtration efficiency of nanoparticles in standard filter media. *Journal of Nanoparticle Research*; 9(1): 109-115.

Washizu M, Jones TB. (1994) Multipolar dielectrophoretic force calculation. *Journal of Electrostatics*; 33(2): 187-198.

Weber E. (1965) *Electromagnetic theory ; static fields and their mapping*. New York: New York : Dover Publications.

Wick P, Manser P, Limbach LK, Dettlaff-Weglikowska U, Krumeich F, Roth S, Stark WJ, Bruinink A. (2007) The degree and kind of agglomeration affect carbon nanotube cytotoxicity. *Toxicology letters*; 168: 121-31.

Wiedensohler A. (1988) An approximation of the bipolar charge distribution for particles in the submicron size range. *Journal of Aerosol Science*; 19(3): 387-389.

Yamada S, Seto T, Otani Y. (2011) Influence of Filter Inhomogeneity on Air Filtration of Nanoparticles. *Aerosol and Air Quality Research*; 11: 155-160.

Yang H, Yu JZ. (2002) Uncertainties in charring correction in the analysis of elemental and organic carbon in atmospheric particles by thermal/optical methods. *Environmental science and technology*; 36: 5199-5204.

Zhang H, Kuo YY, Gerecke A, Wang J. (2012) Co-release of hexabromocyclododecane (HBCD) and nano- and microparticles from the thermal cutting of polystyrene foams. *Environmental Science and Technology*; 46: 10990–10996.

Zhao Q. (2013) *Characterization and thermal decomposition behavior of carbon nanotubes and nanocomposites*. M.S. Thesis, University of Cincinnati.

Zimmermann E, Derrough S, Locatelli D, Durand C, Fromaget JL, Lefranc E, Ravanel X, Garrione J (2012) Results of potential exposure assessments during the maintenance and cleanout of deposition equipment. *Journal of Nanoparticle Research*; 14 (10): 1-17.

Appendix 1 Aerosol Emission Monitoring and Assessment of Potential Exposure to Multi-walled Carbon Nanotubes in the Manufacture of Polymer Nanocomposites (Supplementary Material)

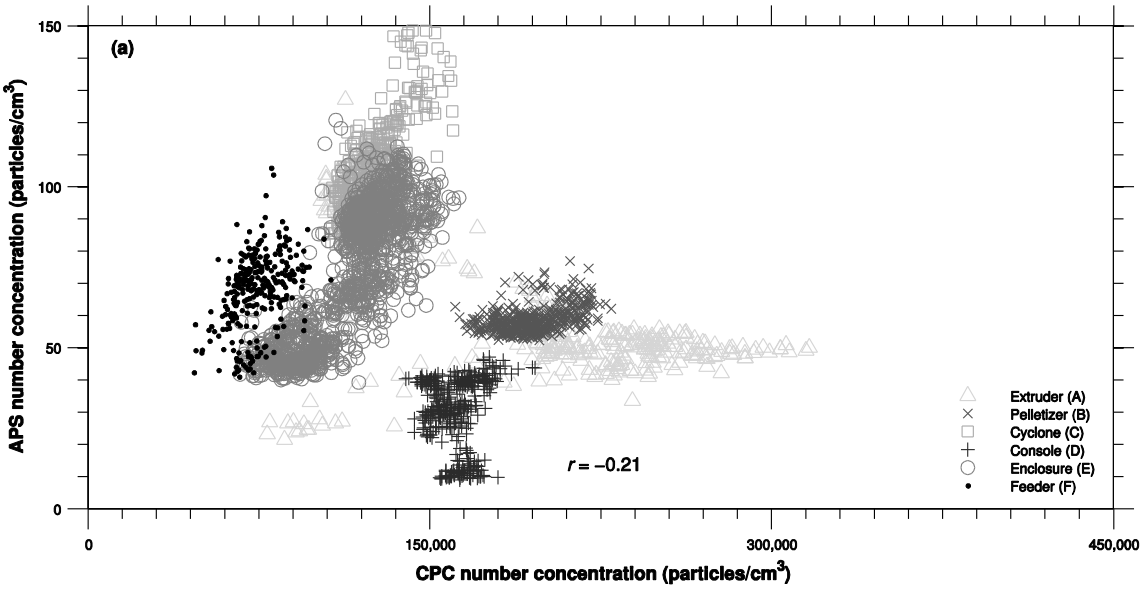
(a)
APS number concentration (particles/cm3)
150
100
50
0
0
150,000
300,000
450,000
CPC number concentration (particles/cm3)
r = –0.21
Extruder (A)
Pelletizer (B)
Cyclone (C)
Console (D)
Enclosure (E)
Feeder (F)

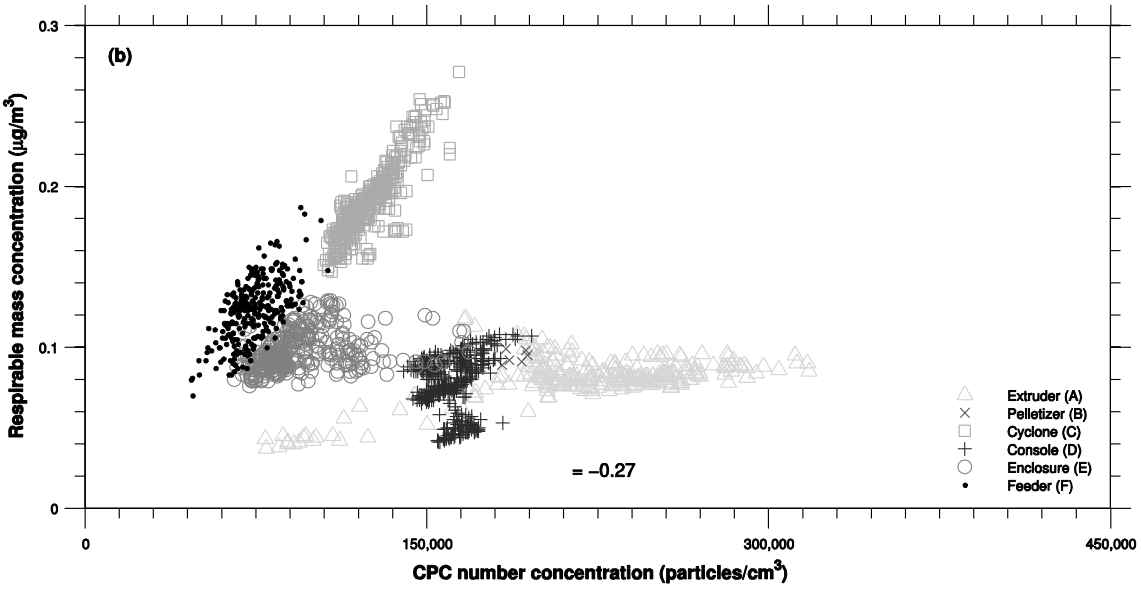
(b)
Respirable mass concentration (µg/m3)
0.3
0.2
0.1
0
0
150,000
300,000
450,000
CPC number concentration (particles/cm3)
= –0.27
Extruder (A)
Pelletizer (B)
Cyclone (C)
Console (D)
Enclosure (E)
Feeder (F)

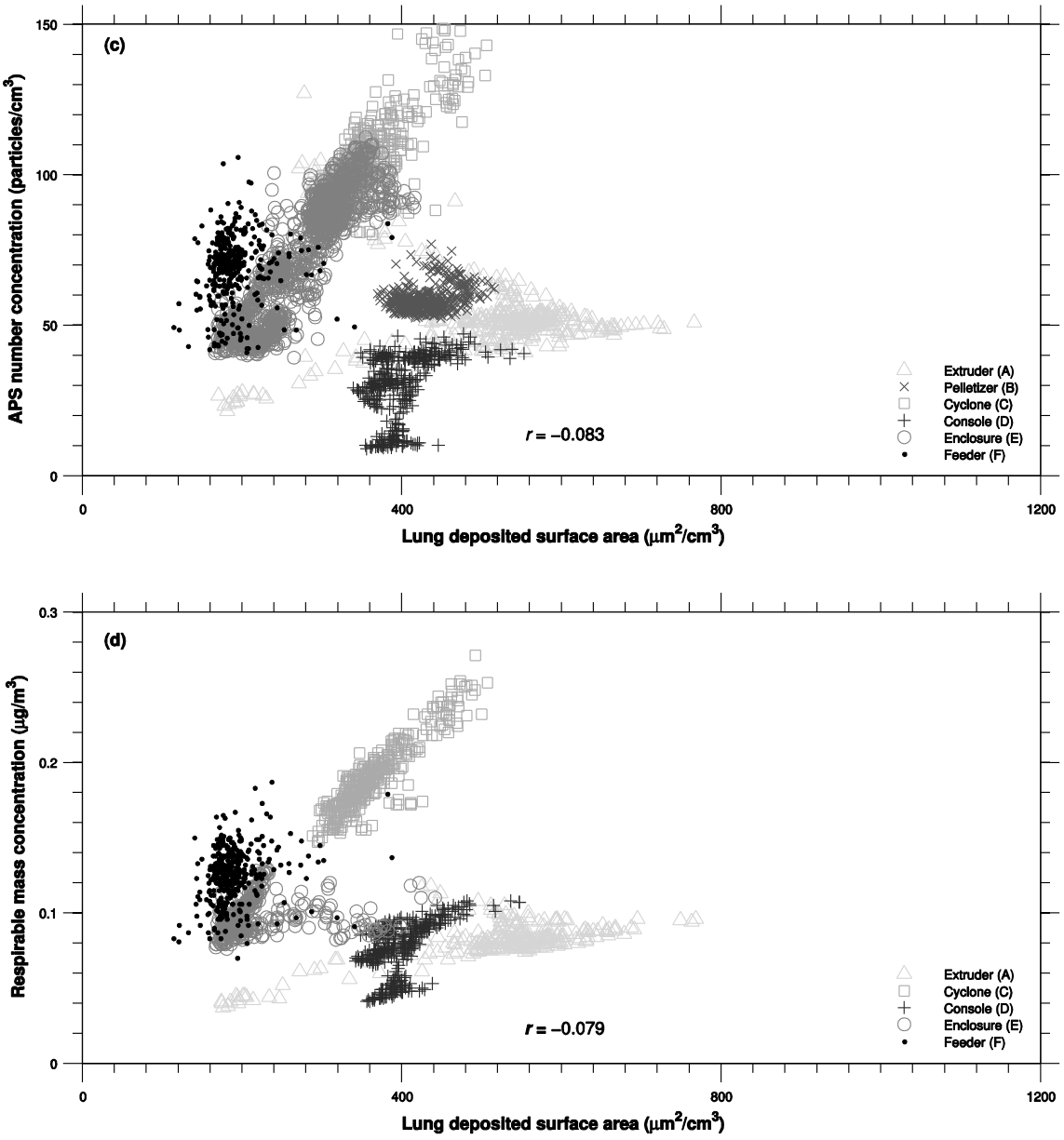

Fig. A1.1 Correlation of (a) particle number concentrations measured by CPC and APS, (b) particle number concentrations measured by CPC and respirable mass concentrations, (c) lung deposited surface area concentrations and particle number concentrations measured by APS, and (d) lung deposited surface area concentrations and respirable mass concentrations during steady, continuous nanocomposite production at selected locations in the facility.

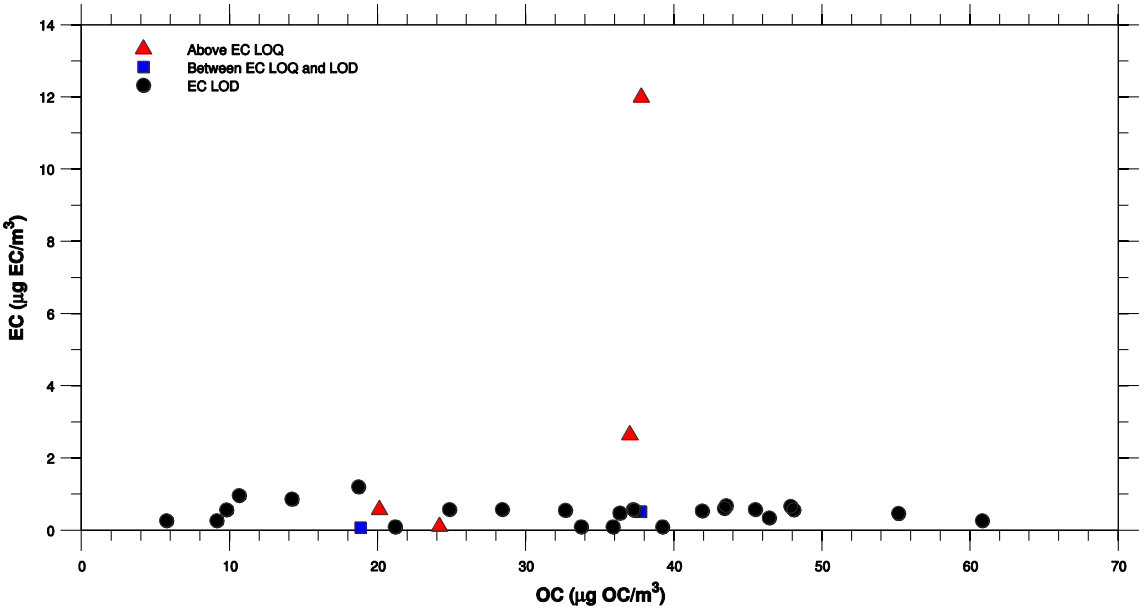

Fig. A1.2 Reported EC concentrations, where the LOD is given for samples whose EC concentrations were below the LOD, and OC concentrations for the 31 area and PBZ samples

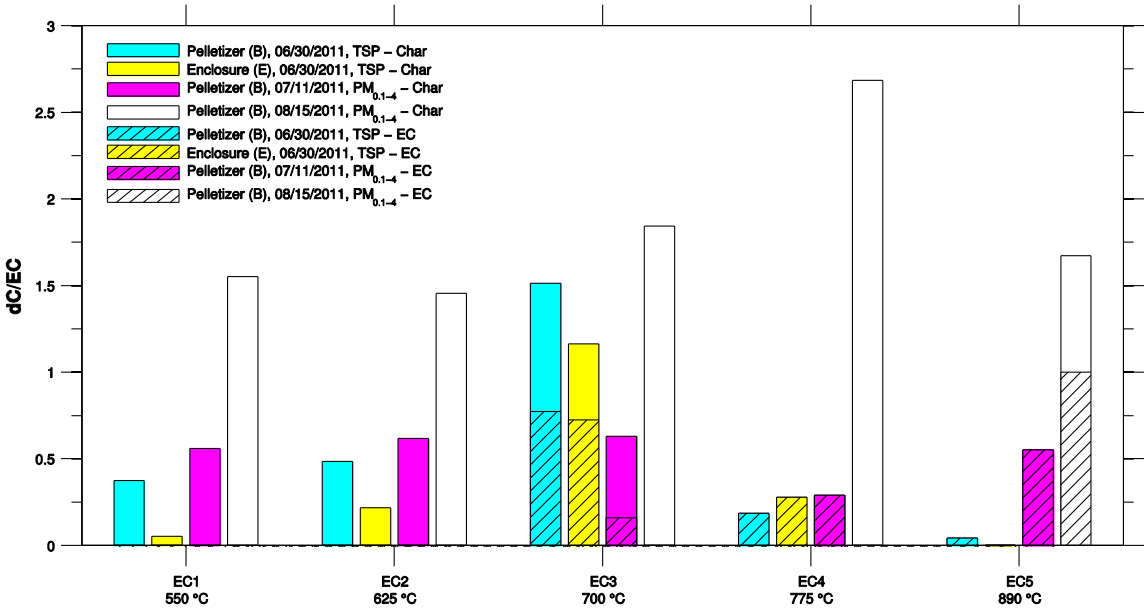

Fig. A1.3 Carbon masses detected at each oxidation temperature in NIOSH Method 5040 analysis, dC, normalized by the total elemental carbon mass, EC, for the four samples containing quantifiable EC concentrations, where the term char refers to pyrolytically generated carbon.

Table A1.1 Summary of sampling times for area and PBZ sampling during production of nanocomposites containing MWCNTs

Monitoring event			OC-EC sampling time (min)			MWCNT by ICP-MS sampling time (min)	Total dust by gravimetric analysis sampling time (min)		MWCNTs found by SEM sampling time (min)
Location	Date	Activity	TSP at 4 L/min	PM_4 at 2.5 L/min	$PM_{0.1}$ and $PM_{0.1-4}$ at 2 L/min	TSP at 5 L/min	PM_4 at 2.5 L/min	$PM_{0.1}$ and $PM_{0.1-4}$ at 2 L/min	TSP at ~ 2.5 L/min
Extruder (A)	4/6/11	Two extruders[2]	–	–	–	–	–	–	178
	6/30/11	One extruder[5]	328	–	–	–	–	–	–
Pelletizer (B)	4/5/11	Clean pelletizer and cyclone[1]	–	–	–	–	–	–	78
	4/6/11	Two extruders[2]	–	–	–	–	–	–	168
	6/30/11	One extruder[5]	327	–	–	–	–	NA[b]	–
	7/06/11	One extruder[6]	–	294	–	–	–	NA[b]	–
	7/11/11	One extruder	–	444	450	–	–	–	453
	7/12/11	Two extruders	–	402	400	–	319	NA[b]	–
	8/15/11	One extruder	–	1440	1425	–	–	–	–
	8/16/11	One extruder	–	1449	1430	–	–	–	–
Cyclone (C)	4/28/11	One extruder[a,4]	155	–	–	155	–	–	154
Console (D)	4/08/11	Background	154	–	–	148	–	–	–
	4/26/11	One extruder[a,3]	156	–	–	–	–	–	152
Enclosure (E)	4/08/11	Background	–	–	–	155	–	–	164
	4/28/11	MWCNT transfer; change vacuum bags, one extruder[a,4]	155	–	–	163	–	–	162
	6/30/11	One extruder[5]	321	–	–	–	–	–	–
	8/15/11	One extruder	–	1450	–	–	–	–	–
	8/16/11	One extruder	–	–		–	–	–	–

Feeder (F)	4/6/11	MWCNT transfer, two extruders[2]	–	–	–	–	–	–	17
	4/26/11	One extruder[a,3]	151	–	–	151	–	–	151
Gowning (G)	5/24/11	Two extruders	150	–	–	–	–	–	–
PBZ	4/4/11	MWCNT transfer, one extruder	–	240	–	–	–	–	–
PBZ	4/5/11	Clean pelletizer and cyclone[1]	–	115	–	–	–	–	–
PBZ	4/6/11	MWCNT transfer, two extruders[2]	–	209	–	–	–	–	–
PBZ	4/26/11	One extruder[3]	–	207	–	–	–	–	–
PBZ	4/28/11	MWCNT transfer, change vacuum cleaner bags, one extruder[4]	–	294	–	–	–	–	–
PBZ	5/25/11	One extruder	–	243	–	–	–	–	–
PBZ	6/30/11	One extruder[5]	–	251	–	–	–	–	–
PBZ	7/06/11	One extruder[6]	–	228	–	–	–	–	–

–: Not sampled

[a] Samples were collocated with the direct-reading instruments in Figs. 3.3,3.4, A1.1

[b] Sampling times are not available due to missing records

[1 -- 6] Area and PBZ samples collected concurrently

Table A1.2 Summary of results from area and PBZ sampling during production of nanocomposites containing MWCNTs.

Monitoring event			EC (µg EC/m^3)				OC (µg OC/m^3)				MWCNT by ICP-MS (µg/m^3)	Total dust by gravimetric analysis (µg/m^3)			MWCNTs found by SEM
Location	Date	Activity	TSP	PM_4	$PM_{0.1\text{-}4}$	$PM_{0.1}$	TSP	PM_4	$PM_{0.1\text{-}4}$	$PM_{0.1}$	TSP	PM_4	$PM_{0.1\text{-}4}$	$PM_{0.1}$	TSP
Extruder (A)	4/6/11	Two extruders[2]	–	–	–	–	–	–	–	–	–	–	–	–	Yes
	6/30/11	One extruder[5]	0.27[a]	–	–	–	61	–	–	–	–	–	–	–	–
Pelletizer (B)	4/5/11	Clean pelletizer and cyclone[1]	–	–	–	–	–	–	–	–	–	–	–	–	Yes
	4/6/11	Two extruders[2]	–	–	–	–	–	–	–	–	–	–	–	–	Yes
	6/30/11	One extruder[5]	2.6	–	–	–	37	–	–	–	–	–	34	18	–
	7/6/11	One extruder[6]	–	0.48[a]	–	–	–	36	–	–	–	–	39	16	–
	7/11/11	One extruder	–	0.52[b]	0.58	0.86[a]	–	38	20	14	–	–	–	–	Yes
	7/12/11	Two extruders	–	0.35[a]	0.10[a]	0.96[a]	–	46	34	11	–	60	29	41	–
	8/15/11	One extruder	–	0.10[a]	0.11	0.27[a]	–	39	24	9.1	–	–	–	–	–
	8/16/11	One extruder	–	0.09[a]	–	–	–	36	–	–	–	–	–	–	–
Cyclone (C)	4/28/11	One extruder[c, 4]	0.57[a]	–	–	–	45	–	–	–	2.7[a]	–	–	–	Yes
Console (D)	4/8/11	Background	0.57[a]	–	–	–	9.8	–	–	–	2.8[a]	–	–	–	No
	4/26/11	One extruder[c, 3]	0.56[a]	–	–	–	37	–	–	–	–	–	–	–	Yes
Enclosure (E)	4/8/11	Background	–	–	–	–	–	–	–	–	2.7[a]	–	–	–	Yes
	4/28/11	MWCNT transfer; change vacuum bags, one extruder[c, 4]	0.54[a]	–	–	–	42	–	–	–	2.6[a]	–	–	–	Yes (See Fig. 3.6)
	6/30/11	One extruder[5]	12	–	–	–	38	–	–	–	–	–	–	–	–

	8/15/11	One extruder	–	0.10[a]	–	–	–	21	–	–	–	–	–	–	–
	8/16/11	One extruder	–	–	0.08[b]	0.27[a]	–	–	19	5.7	–	–	–	–	–
Feeder (F)	4/6/11	MWCNT transfer, two extruders[2]	–	–	–	–	–	–	–	–	–	–	–	–	Yes
	4/26/11	One extruder[c, 3]	0.57[a]	–	–	–	48	–	–	–	2.8[a]	–	–	–	Yes
Gowning (G)	5/24/11	Two extruders	0.58[a]	–	–	–	25	–	–	–	–	–	–	–	–
PBZ	4/4/11	MWCNT transfer, one extruder	–	0.58[a]	–	–	–	37	–	–	–	–	–	–	–
PBZ	4/5/11	Clean pelletizer and cyclone[1]	–	1.2[a]	–	–	–	19	–	–	–	–	–	–	–
PBZ	4/6/11	MWCNT transfer, two extruders[2]	–	0.66[a]	–	–	–	48	–	–	–	–	–	–	–
PBZ	4/26/11	One extruder[3]	–	0.68[a]	–	–	–	44	–	–	–	–	–	–	–
PBZ	4/28/11	MWCNT transfer, change vacuum cleaner bags, one extruder[4]	–	0.47[a]	–	–	–	55	–	–	–	–	–	–	–
PBZ	5/25/11	One extruder	–	0.58[a]	–	–	–	28	–	–	–	–	–	–	–
PBZ	6/30/11	One extruder[5]	–	0.55[a]	–	–	–	33	–	–	–	–	–	–	–
PBZ	7/6/11	One extruder[6]	–	0.61[a]	–	–	–	43	–	–	–	–	–	–	–

–: Not sampled
[a] LOD
[b] Between the LOD and LOQ
[c] Samples were collocated with the direct-reading instruments in Figs. 3.3, 3.4, A1.1
[1 -- 6] Area and PBZ samples collected concurrently

Appendix 2 Collection Efficiency of Submicrometer Aerosol Particles in Electret Filters (Supplementary Material)

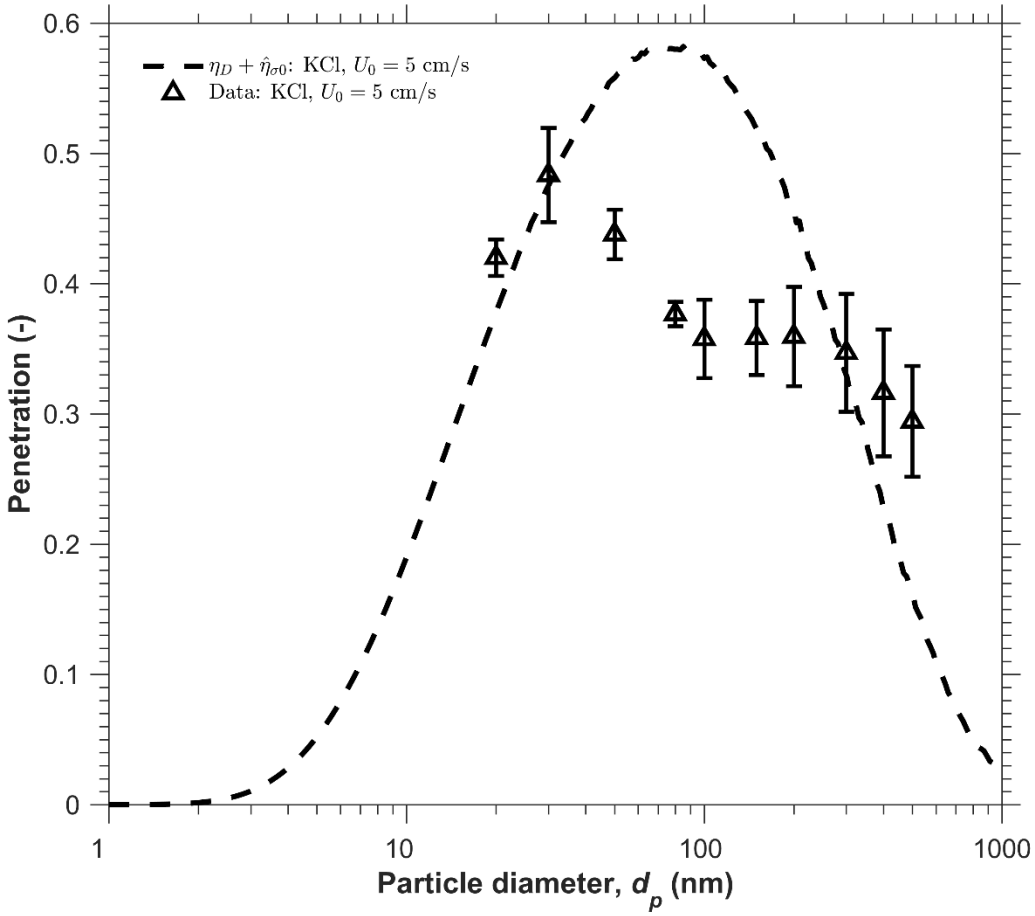

Fig. A2.1 Comparison of theoretical and experimental aerosol penetration for Media C challenged by uncharged KCl particles at a face velocity of 5 cm/s

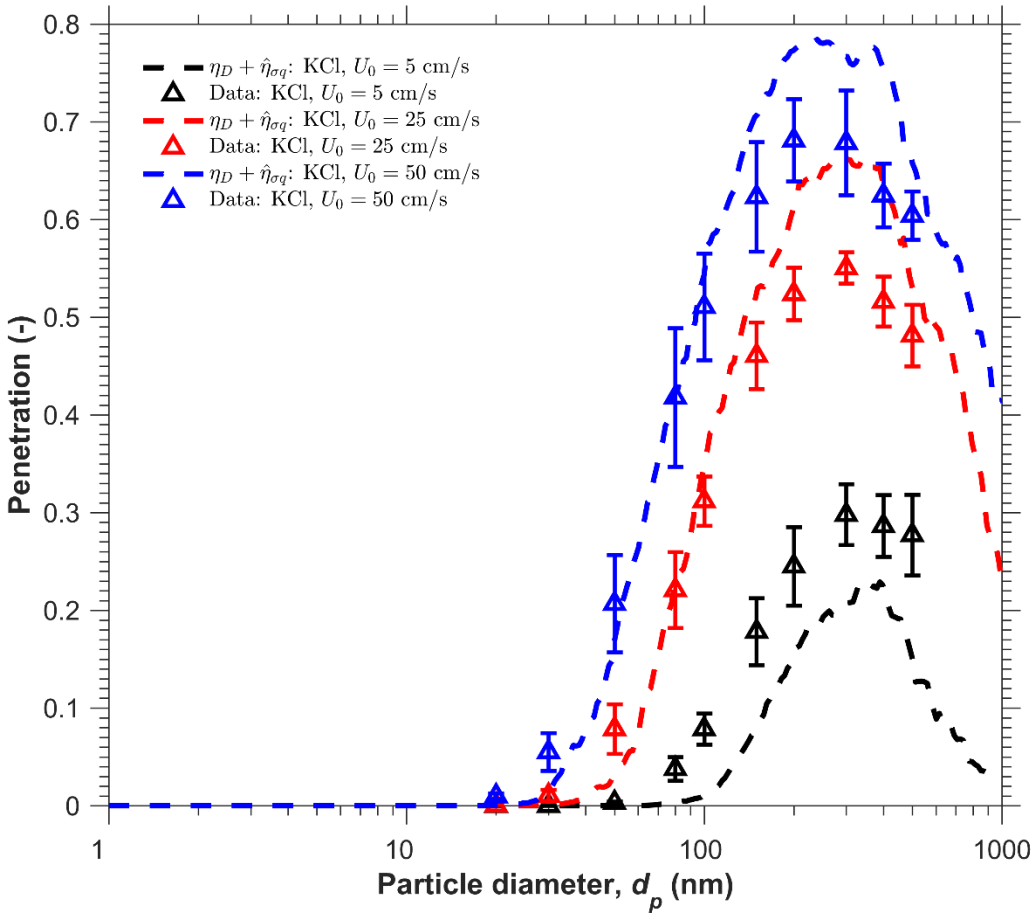

Fig. A2.2 Comparison of theoretical and experimental aerosol penetration for Media C challenged by singly charged KCl particles

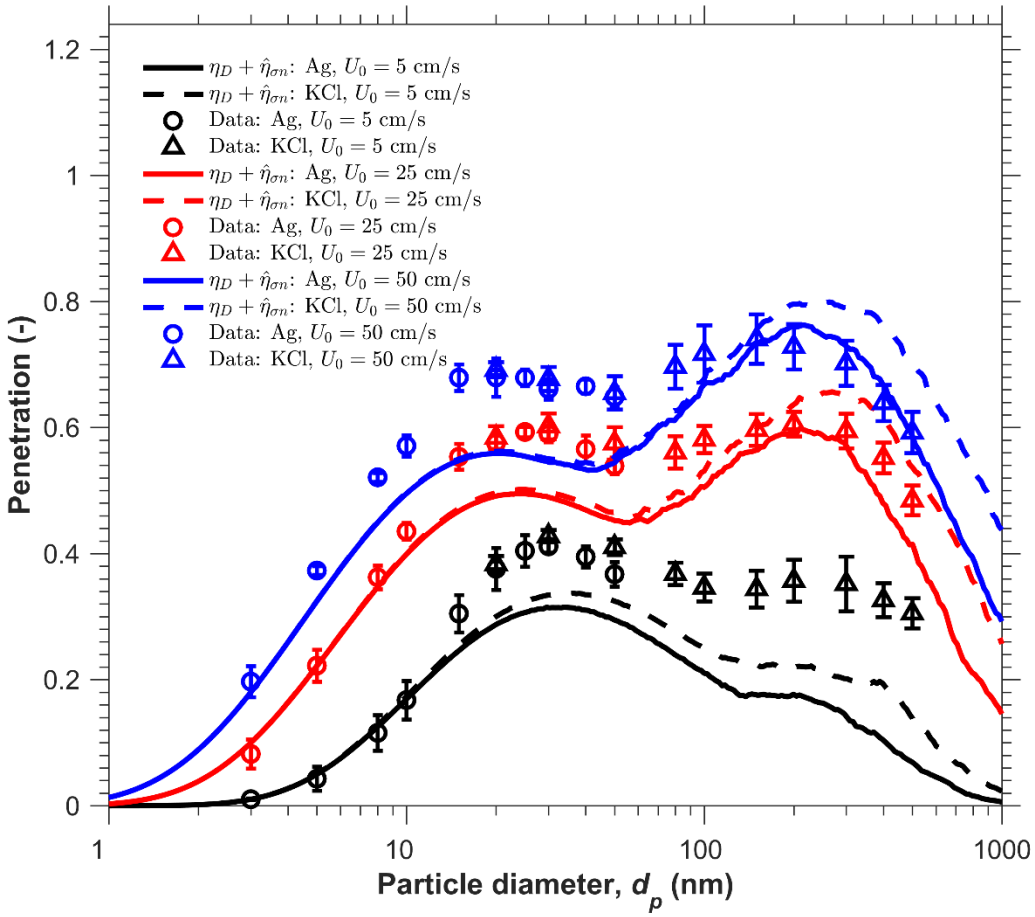

Fig. A2.3 Comparison of theoretical and experimental aerosol penetration for Media C challenged by charge neutralized particles

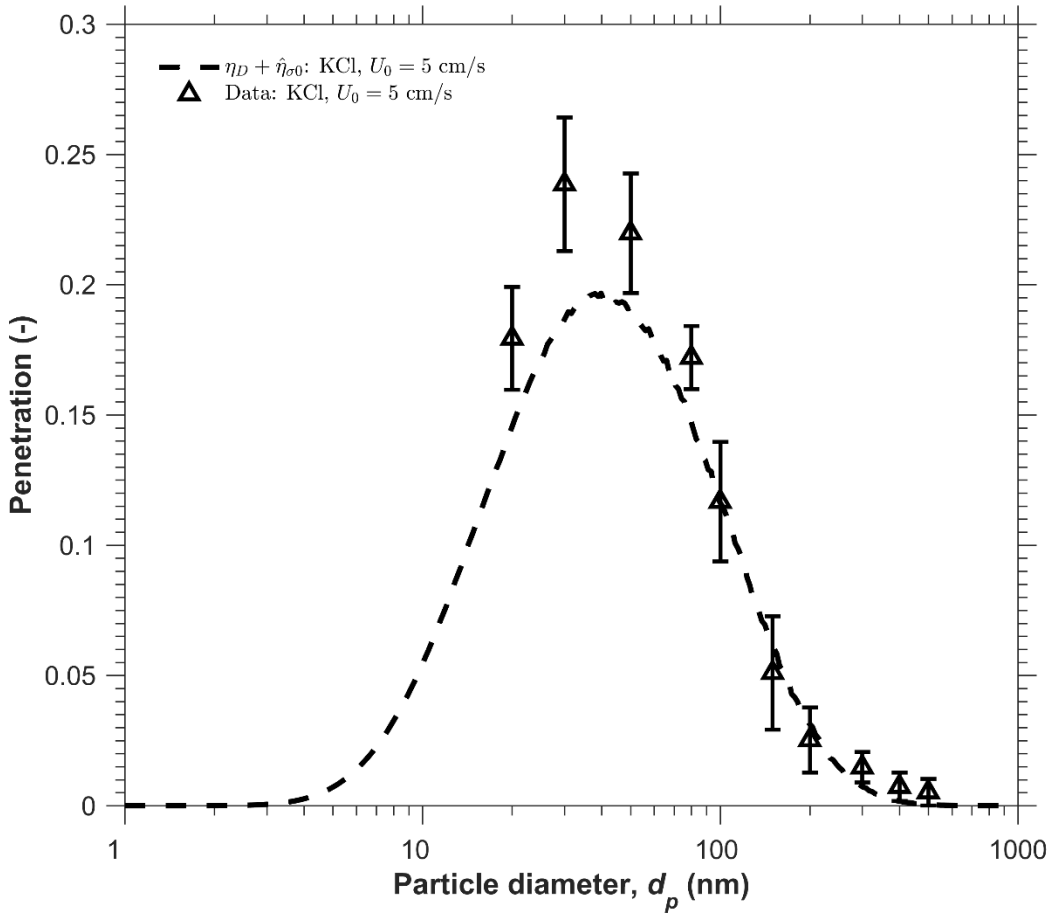

Fig. A2.4 Comparison of theoretical and experimental aerosol penetration for Media F challenged by uncharged KCl particles at a face velocity of 5 cm/s

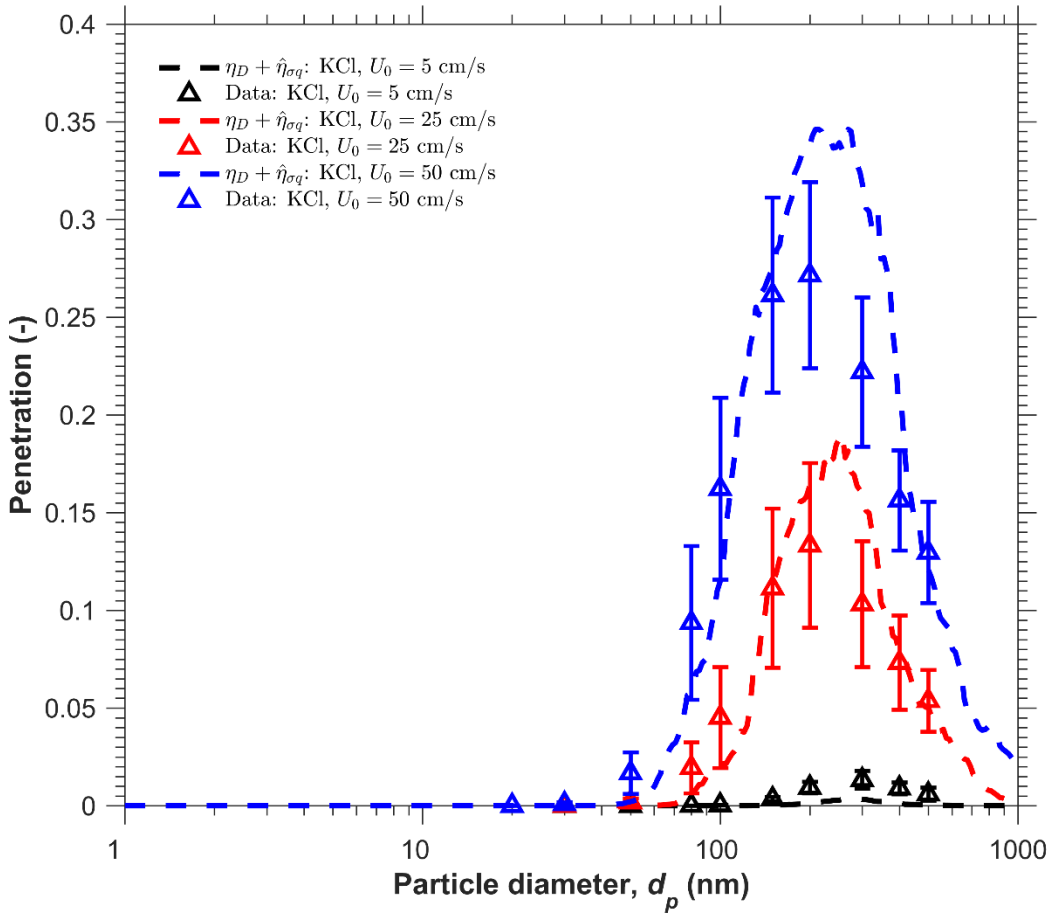

Fig. A2.5 Comparison of theoretical and experimental aerosol penetration for Media F challenged by singly charged KCl particles

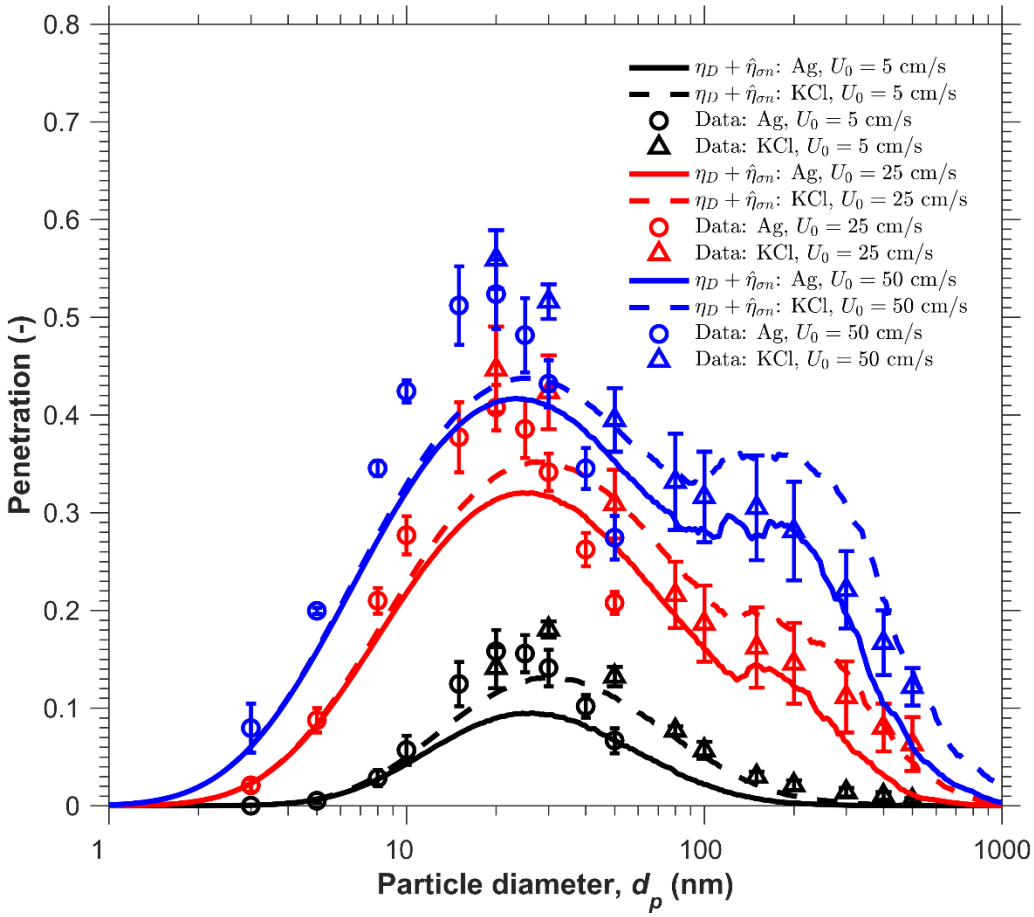

Fig. A2.6 Comparison of theoretical and experimental aerosol penetration for Media F challenged by charge neutralized particles